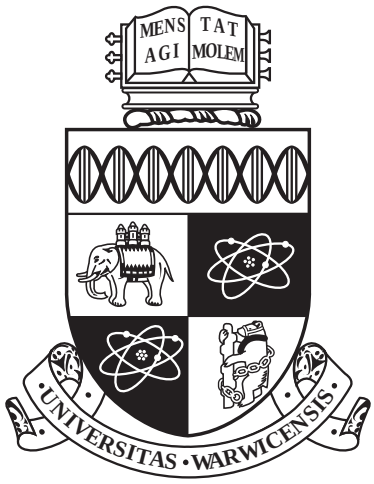

Energy Transfer from Energetic Ions to Dense Plasmas

by

Donald Edie

Thesis

Submitted to the University of Warwick

for the degree of

Doctor of Philosophy

Centre for Fusion, Space and Astrophysics, Department of Physics

October 2012

THE UNIVERSITY OF
WARWICK

Contents

Acknowledgments

Ultimately, this work has been the result of the combined efforts of many people over the previous years and in this section I would like to acknowledge the valuable contributions that have been made by my collaborators.

Firstly, I would like to thank my supervisor Dr. D.O. Gericke for his guidance and tutelage that has been instrumental to the success of this research. I would also like to acknowledge the contributions of Dr. J. Vorberger who has taken an active role in my education and also in the implementation of the simulations presented in this work by providing me with data from DFT-MD simulations and equation of state calculations for non-ideal systems.

I would like to thank Professor S. Rose the time that he has taken to discuss stopping power theory with me and also for his invaluable contributions regarding the numerical calculations of electron stopping power in degenerate systems which greatly increased the feasibility of the simulation of complex systems.

I would also like to thank the group of Professor M. Bonitz at Christian-Albrechts-Universität zu Kiel for hosting my stay for a week, in particular I would like to acknowledge here the work of David Hochstuhl and the time he dedicated to teaching me about their research and expanding my understanding of computational Hartree-Fock techniques.

Finally, I would like to acknowledge the financial support of the Engineering and Physical Sciences Research Council, without which I would not have had the means to be able to pursue this research.

Declarations

I declare that the work which I present here in this thesis is my own work unless otherwise stated. This work was carried out at the University of Warwick under the supervision of Dr. D.O. Gericke. This work has been performed for submission for the degree of Doctor of Philosophy and has not been previously submitted to the University of Warwick or any other academic institution for admission to a higher degree.

The work presented within has, in part, been previously published within the scientific community by myself and my colleagues. The details of these publications are as follows:

- Rutherford Appleton Laboratories, Central Laser Facility annual report (theory and computation section), *Alpha-particle stopping power for dense hydrogen plasmas*, 2009.
- GSI Helmholtzzentrum für Schwerionenforschung, GSI Scientific Report 2011 (plasma physics section), *Fluctuations of Particle Stopping in Dense Plasmas*, 2011.

Abstract

Theoretical investigations into the energy deposition of fast ion in dense plasma regimes are presented. These simulations allow insight into the behaviour of charged particle stopping and other energy transfer processes as seen in a dense plasma regime.

The modelling of ions within partially ionised plasmas are investigated with respect to their effect on particle scattering interactions. Calculated scattering cross-sections are used as a measure of significance in comparing the cases of ions treated as screened point particles versus the case of bound electrons of finite spatial extent being modelled using Hartree-Fock theory.

Prominent effects of naturally occurring, microscopic density fluctuations on particle stopping are then investigated using DFT-MD simulations to describe the local electron densities. An analysis is repeated for several different DFT-MD profiles, representing different target materials and regimes. The results are then presented statistically with a qualitative interpretation.

Finally, a simulation is presented which models the inter-particle energy transfer processes that drive the initial stages of an alpha particle burn wave in an inertial fusion scenario. The effects on burn time of such criteria as degeneracy in the target electron system, electron-ion temperature equilibration timescales and the rate of fusion reactions within the hot spot are all investigated and the relative dominance of these variables in different regimes is discussed.

Chapter 1

Introduction

Observations of free particles interacting with composite matter can be used to infer internal properties of the composite matter body in question. Probing composite matter with free particles in this way is a useful diagnostic. However, our ability to probe internal properties in this way relies upon our existing knowledge of particle interactions with bulk materials of known composition. It is of interest for us to improve the accuracy with which we can theoretically model such particle interactions because this will help us with future experimental work. The particle interactions in themselves can happen through a variety of channels and are often described by many different physical approaches. Particle energy deposition and stopping power is an example that has been the subject of much theoretical investigation [Bethe [1930]; Bohr [1916]; Bloch [1933]; Fermi and Teller [1947]; Lindhard [1954]]. The theoretical modelling of inter-particle interactions quickly becomes a complex process. In many scenarios, we find that small changes in the treatment of the system can result in large changes in the results of our theoretical calculations. The bulk of this thesis concerns itself with the results of modelling these interactions from the perspective of a statistically averaged interaction of many particles. Although, to begin with, these first chapters will introduce some energy transfer models which are commonly used in particle simulations. We will also explain the derivation of these models and the assumptions used which dictate the regimes in which each model is applicable.

In this introduction, the properties of dense plasmas will be discussed for the purpose of highlighting the behavioural differences that qualify a plasma as being 'dense' and what separates this from any other form of ionised matter. Creation of dense plasmas will also briefly be covered to show the fields in which the properties of dense plasmas are of interest, such as behaviour of astrophysical plasmas and high

energy, dense plasmas that are created for inertial confinement fusion [Atzeni and Meyer-ter-Vehn [2004]; Lindl [1998]; Chabot et al. [1994]]. Since inertial fusion is currently a matter of significant interest, much of the research shown in this thesis was performed with consideration of its applicability to inertial confinement fusion. As a result, the introduction will conclude with an introduction to the concepts of inertial fusion itself which will cover experimental design and a brief overview of the progress made by the National Ignition Facility towards its original goal of creating a controlled burning plasma in a laboratory environment [Moses and Wuest [2005]].

1.1 Particle beams as a probe of matter

Historically, probing matter targets with charged particle beams has often provided a critical insight into the target's internal structure. The discovery of the nucleus by Ernest Rutherford in 1909 was the result of such a particle beam experiment. Large angle scattering observed in a beam of alpha-particles incident on a gold foil implied the existence of highly localised, massive scattering bodies within the gold [Rutherford [1911]]. This research lead to the development of Rutherford's orbital model of the atom and the alpha scattering experiment provided the strongest evidence for the acceptance of the nuclear model over the existing 'plum pudding' model of the atom formulated by J. J. Thompson [Thomson [1904]].

In modern experiments, much more exotic, higher energy states of matter can be created and studied, although some of the properties of these high energy matter states are not yet fully understood. Currently, high energy-density matter (HEDM) research is only of particular interest to quite a limited number of fields but in future, the uses of HEDM are hoped to expand. HEDM physics is of interest for the modelling of astrophysical plasmas because it is believed that some massive bodies such as the planet Jupiter create dense plasma conditions within their planetary core [Guillot [1999]; Militzer et al. [2008]; Nettelmann et al. [2008]] and it is also thought that these conditions exist in the atmospheres of white dwarves and neutron stars[Dufour et al. [2007], Daligault and Gupta [2009]]. HEDM is of interest to inertial fusion research because the high energy fusion plasmas that are created are within the HEDM regime. As such, a better understanding of how HEDM behaves will provide useful additional information that will help in our attempts to build a device which can create an efficient laboratory fusion plasma.

One significant characteristic which separates a dense plasma from a sparse plasma is the interaction timescales of the constituent particles, i.e. collisional timescales versus the timescales of collective interactions via long range Coulomb

forces, which allows simultaneous 'collective' interaction with many neighbouring particles. The relative lengths of these timescales, with respect to each other, control the way in which the plasma will behave. Critically, for a dense plasma, the inter-particle distance becomes so small that the collisional timescales become far shorter than the timescales of collective effects and oscillatory wave motion. As a result, the local kinetic behaviour of particles in a dense plasma is largely dominated by recent collisional interactions and the influence of large-scale fluid-like collective wave behaviour is reduced [Huba [2007]]. The high opacities that are typical of HEDM makes internal particle behaviour difficult to observe in an HEDM body. As a result, we are reliant on penetrative probes, such as particle beams [Golubev et al. [1998]; Tahir et al. [2003]] or high energy photons such as hard x-rays [Ichimaru [2004]]. These are our primary tools for probing beneath the surface of the dense plasmas we create and such probing is necessary for us to be able to better understand the physics which governs the behaviour of these dense plasmas.

1.2 Physics of non ideal plasmas

We begin by considering a theoretical plasma as a system of particles in which the energies and momenta of a particle species, a, can be statistically described by a distribution function, $f_a(p)$. In this description, an ideal plasma is considered to be one in equilibrium in which there is no evolution of the distribution function [Kremp et al. [2004]],

$$f_a(p) = f_a^0(p). \tag{1.1}$$

The alternative to this is a non ideal plasma where the plasma is not in an equilibrium and so the distribution of particle energies will change. In this case the evolution of the distribution function is described by a kinetic equation which is generally of the form

$$\left(\frac{\partial}{\partial t} + \mathbf{v}\cdot\frac{\partial}{\partial \mathbf{r}} + \mathbf{F}\cdot\frac{\partial}{\partial \mathbf{p}}\right) f_a = I_a \tag{1.2}$$

where I_a describes the collisional interactions in the system. On the microscopic level, significant effects arise which are not described by generalised fluid descriptions of a plasma. For instance, in many dense plasmas, limits set by the Heisenberg uncertainty principle begin to be encroached. The effect of this is that the state of a particle will no longer be fully determined by its trajectory in phase space but instead should be described by the particle wavefunction. An important effect

of this is the significance of spin statistics. The particle distribution functions are split [Kremp et al. [2004]] such that properties are no longer Boltzmann distributed but rather the Fermions (non-integer spin particles) take a Fermi-Dirac distribution [Fermi [1926]]

$$f_a(p) = \frac{1}{\exp\left(\beta(p^2/2m_a - \mu_a)\right) + 1} \tag{1.3}$$

and the Bosons (integer-spin particles) take a Bose-Einstein distribution [Bose [1924]]

$$f_a(p) = \frac{1}{\exp\left(\beta(p^2/2m_a - \mu_a)\right) - 1} \tag{1.4}$$

where $\beta = 1/k_B T$, p is the momentum at which the distribution is being evaluated, m_a mass of a particle of the species in question and μ_a is the chemical potential for particle species a in the system being analysed. At zero temperature in a Fermi system, the chemical potential takes the limiting value of the Fermi energy and is given as [Kremp et al. [2004]]

$$\mu_a^0 = E_F = \frac{h^2}{2m_a}\left(\frac{6\pi^2 n_a}{2s_a + 1}\right)^{2/3} \tag{1.5}$$

where n_a is the number density of particles of species a and s_a is their spin value. This quantity describes some limiting behaviours of strongly degenerate Fermi systems only, whose generalised particle distribution takes the form shown in equation (1.3).

It is important to note here that, in the non-equilibrium case, the distribution functions will still fully define the kinetic energy of the particles in the system. Importantly, this is also true when the distribution describes a beam of particles and so this approach can easily be applied to descriptions of particle stopping systems as well. The proceeding subsections will introduce some further effects that must be included when modelling dense plasmas and show the implications that these effects will have on the plasma modelling process.

1.2.1 Correlation effects

Dense plasmas can generally be described as a strongly-correlated many-particle system. In this sense, correlation relates to the influence of local Coulomb interactions with nearby particles. As the density of the plasma increases, so too will the inter-particle coupling, which will change the dynamic properties of the plasma. The classical coupling parameter is a measure of the average Coulomb potential between each neighbouring pair of particles with respect to their thermal energy and is given

here for electrons by [Kremp et al. [2004]]

$$\Gamma_{ee} = \frac{e^2 \left(4\pi n/3\right)^{1/3}}{k_B T}. \tag{1.6}$$

This coupling parameter scales with density and scales inversely with temperature. Systems described as weakly coupled will have a coupling parameter value of less than one and systems that are described as strongly coupled will have a coupling parameter value that is larger than one. For very high values of this coupling parameter ($\Gamma_{ii} > 172$ calculated for ions) the plasma ions will form a lattice and the dense plasma will retain some of the structural properties of solid matter. In plasma regimes where the coupling parameter is typically larger than one, simulations of particle interactions are generally improved by consideration of direct inter-particle Coulomb forces as opposed to considering an averaged Coulomb field.

In a dense plasma, the self energy of a particle can also provide quite a significant amount of energy. Self energy describes the additional kinetic energy that a charged particle has within the body of a dense plasma as a result of the influence of Coulomb interactions with neighbouring particles [Kremp et al. [2004]]. This self energy can be thought of as a modification to the ideal kinetic energy, $E = p^2/2m$, such that the kinetic energy is then given as $E_a(p) = p^2/2m_a + \mathrm{Re}\Sigma_a$, where Σ_a is the self energy contribution. The self energy is given in full from the potential induced by the particle trajectory through the plasma. In the static limit, at lowest order, the expression for the self energy reduces to

$$\Sigma_a(0) = -\kappa e_a^2 \tag{1.7}$$

where κ is the inverse Debye screening length [Kremp et al. [2004], p. 24], i.e. in atomic units, at lowest order, the self energy is equal to the value of the Coulomb potential at the Debye length. In some of the later work of this thesis it will be shown that self energy contributions can cause excitation and even ionisation of electron states in high density matter.

1.2.2 Quantum effects

As previously mentioned, in a dense plasma the particle state is defined by the particle wavefunction. This wavefunction has an associated wavelength that is determined by the kinetic energy of the particle in question,

$$\Lambda_a = \frac{h}{\sqrt{2\pi m_a k_B T}}. \tag{1.8}$$

Here, Λ_a is the particle wavelength and m_a is the particle mass, with the quantum mechanical expectation value for the kinetic energy of a free particle being, $E = \pi k_B T$. This wavelength is the de Broglie wavelength associated with an electron system that has an average thermal velocity of

$$v_{th} = \sqrt{2\pi k_B T / m_e}. \tag{1.9}$$

In some cases, the plasma can become so dense that the inter-particle distances are on the order of this wavelength. The level of degeneracy is generally quantified as

$$n_a \Lambda_a^3 = n_a \left(\frac{h}{\sqrt{2\pi m_a k_B T}} \right)^3. \tag{1.10}$$

This gives an approximate measure of the number of particles which lie within a thermal wavelength of any given single particle of that species. The border between a degenerate and a non-degenerate plasma is considered as lying at $n_a \Lambda_a^3 = 1$ with strongly degenerate plasmas having values much larger than one and non-degenerate plasmas having values much smaller than one. In the cases of significant degeneracy, it is important to include the effects of degeneracy for indistinguishable particles in order to account for the way in which this degeneracy will modify the distribution functions of the system properties.

One final parameter that is used to quantify the nature of a plasma in a high density state where quantum effects will be prevalent is the Brückner parameter, r_S, which is closely related to the classical coupling parameter and is calculated as the ratio of the mean inter-particle distance to the Bohr radius,

$$r_S = \frac{d}{a_B}. \tag{1.11}$$

This parameter can be of use for quantifying coupling in highly degenerate systems where the uniformity of particles at the Fermi temperature removes temperature dependence from the parameters of the system and so the inter-particle distance dependence in Γ_{ee} remains but its temperature scaling no longer behaves as it would in a non-degenerate system. In these cases, $r_S < 1$ implies that a system will act as a strongly coupled quantum system and $r_S > 1$ implies that a system will act as a weakly coupled quantum system.

For completeness, it should also be noted that in the case of high velocity particle interactions in quantum systems, extra scattering contributions from diffraction processes should be included although these effects are generally not significant at the energy levels of the work detailed in this thesis and so are not considered.

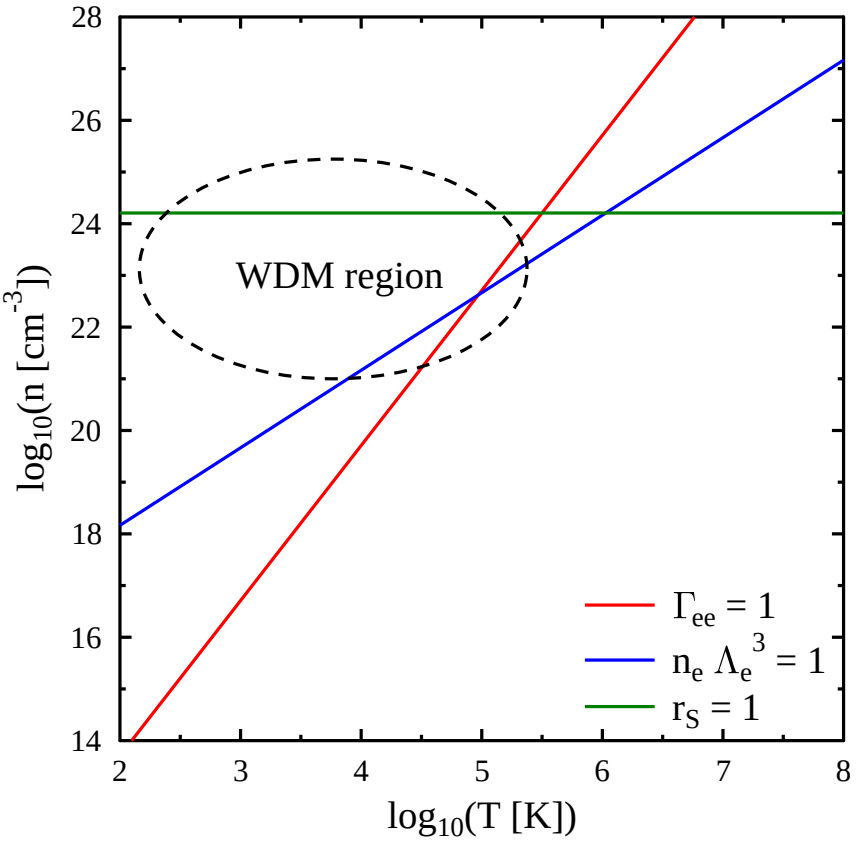

Figure 1.1: Density-temperature plane showing the region of existence of warm dense matter. Limiting cases of the classical electron coupling parameter and the degeneracy are also drawn to show where regimes of strong coupling and electron degeneracy begin. Also marked is the threshold of significance for the Brückner parameter, which marks regimes of strong electron coupling in the degenerate regime.

1.2.3 Warm dense matter

A region of HEDM that can be of particular physical interest is the region of warm dense matter (WDM) in which both the correlation effects and the quantum effects mentioned can occur. WDM is expected to exist at the centres of large gas giant planets and also in inertial fusion scenarios which are of interest to this research. Laboratory WDM is often created by irradiating a solid with a high energy laser or particle beam. The high density of the resulting states mean that the WDM has a sufficiently high opacity such that particle beams or high energy x-ray sources are also required for probing the plasma.

Figure 1.1 shows a density-temperature plane labelling the regions in which these effects manifest and the region in which warm dense matter is considered to exist. The warm dense matter regime is considered to exist at temperatures that are roughly one order of magnitude above and below $T = 1\,\mathrm{eV}$ and inspection of the intersections of the parameters marked on figure 1.1 puts the WDM regime in a region where both the coupling and degeneracy parameters pass their critical values. The implication of this is that often when modelling plasmas in the WDM regime, both quantum and correlation effects of a plasma are important for an accurate simulation [Drake [2006]]. As a result of this, the modelling of warm dense matter can often prove difficult as effects of degeneracy and strong coupling can sometimes prevent the use of more established techniques that are applied to plasmas or indeed those that are applied to modelling solid matter.

1.3 Physics of inertial confinement fusion (ICF)

Currently, there is great scientific and economic interest in developing a safe, clean method of power generation with an abundant fuel source. The hope is that the next generation of power reactors will be capable of providing the world with a stable supply of sustainable electric power in the coming years. One of the more prominent scientific approaches in recent years has been the work into the development of an inertial confinement fusion reactor. Although producing a working model has proved to be a significant challenge [Lindl and Moses [2011]] to the scientific community, the global fusion effort is continually progressing and significant progress has been made in recent years [Michel et al. [2011]; Glenzer et al. [2011b]; Hammel et al. [2011]]. Finding a clean source of nuclear power would have significant advantages, in terms of stability, longevity and ecological impact, over intermittent environmental alternatives or improved efficiency of fossil fuel concepts. As a result, many governments are now lending significant backing to fusion projects around the world.

1.3.1 Nuclear physics

Nuclear power in any form exploits interactions of nuclei in which a transition is made that lowers the total potential of the nucleon configuration and releases energy. Generally, this energy is released in the form of photons, particle creation and kinetic energy of particle products. This energy is equal to the total change of the nuclear binding energies between the initial and final states. In the case of fusion, the interaction that is usually employed is that of fusing isotopes of hydrogen to create

helium with high energy particle by-products.

$$^{2}_{1}\mathrm{D} + {}^{3}_{1}\mathrm{T} \rightarrow {}^{4}_{2}\mathrm{He} + {}^{1}_{0}\mathrm{n}, \tag{1.12}$$

Deuterium-tritium fusion, shown in equation (1.12), is often chosen for laboratory fusion experiments. This is firstly because it has a large fusion interaction cross-section, which occurs at achievable temperatures ($T \sim 10\,\mathrm{keV}$), and secondly because it has a high energy yield per fusion interaction of $\Delta E = 17.59\,\mathrm{MeV}$. $3.5\,\mathrm{MeV}$ of this energy is distributed as kinetic energy of the alpha-particle and the remaining $14.1\,\mathrm{MeV}$ provides the kinetic energy of the neutron. Although, the energy yield is 'high', proposed fusion reactors would need to have a vast amount of these fusion interactions happening within a plasma fuel to sustain the plasma at fusion conditions. The fusion energy of the alpha-particles would, in general, quickly dissipate back into the plasma through charged particle, collisional interactions contributing to the plasma heating. However, the uncharged high energy neutron is free to escape the plasma bulk to be absorbed externally in order to heat a moderator or coolant, for example water. The reactor can then exploit the rapid expansion from the boiling phase change of the heated water in order to turn turbines, and generate electricity.

1.3.2 Conditions to be reached

In 1955, John D. Lawson derived a relationship which gives a measure of the energy production, from fusion reactions, of a body of hydrogen plasma. Originally classified, the work was published in 1957 and from then it was accepted that, in order to produce net energy from a body of fusion plasma, any working fusion concept should at least satisfy the Lawson criterion [Lawson [1957]]. The Lawson criterion could be expressed as a product of three properties of the plasma system. Quoted here for the break-even criteria of deuterium-tritium interactions, the Lawson criterion can be expressed as

$$nT\tau = 10^{21}\mathrm{keV\,s\,m^{-3}}. \tag{1.13}$$

In equation 1.13, n is the number density of the deuterium and the tritium, T is the ion temperature of the deuterium-tritium plasma in kilo-electronvolts and τ is the projected confinement time of the fusion plasma. This criterion can set limits on plasma conditions for energy break-even and plasma ignition, the latter being a regime in which sufficient energy is supplied from fusion alpha-particles to sustain fusion conditions in the plasma with no external heating. Considering the

fusion products, the mass ratio of the alpha-particle to the neutron is four to one. Conservation of momentum for the fusion reaction means that the alpha-particle will only carry a fifth of the energy released from the fusion reaction. As a result the ignition condition requires a five times greater energy density production than the break-even condition. The choice of the deuterium-tritium fusion reaction is primarily because it exhibits a high energy yield relative to similar fusion reactions and it also has a high cross-section for fusion at temperatures and densities which are being achieved in fusion experiments today. Most modern fusion experiments run at plasma temperatures on the order of $T = 10^8\,K$, which is of the order where the cross-section for deuterium-tritium fusion is maximised. Unfortunately, increasing n and τ are not complimentary goals, as creating a denser plasma makes for a less stable system that is much harder to confine. As a result, for experiments today maximising the Lawson criterion has almost become a case of concentrating almost solely on either n or τ. This means working at low density and maximising the available confinement time or working with a low confinement time and maximising the density. Inertial confinement fusion is an example of the latter approach and has been named as such because the fusion plasma is only confined by the inertia of the plasma ions. From this point the definition of inertial confinement is currently quite loose and so it is hardly surprising that there are several approaches which all lie within the scope of this definition. However, for brevity, only laser driven central hotspot inertial fusion will be looked at in any detail.

1.3.3 Alpha-particle heating

One key issue that has limited success of previous fusion experiments has been the limited efficiency of the power generation. It requires a lot of energy to heat and compress the plasma fuel to a temperature that is suitable with regards to the cross-section for fusion reactions. If the energy that is being supplied externally for heating and compression exceeds the energy that is being produced from fusion reactions then the experiment will never become a successful power generator. The requirements on externally supplied energy for heating can be significantly reduced if efficient use is made of the kinetic energy of fusion produced alpha-particles for plasma heating. In many inertial fusion concepts it is hoped that the high density of the fuel will produce such a high density of fusion alpha-particles that once the reaction has been initiated, the heating will be performed solely by alpha-particles and the fusion fuel will be consumed by a self-propagating burn wave.

1.4 Introduction to central hotspot ignition

There are several varying designs that are currently being investigated for the purposes of creating an experimental fusion reactor. Each design has its own issues with regards to plasma control, engineering difficulties in building the device and also issues in extracting a net energy product from the fusion fuel. Much experimental work has been done in recent years to explore the concept of central hotspot ignition for an inertial fusion reactor. This has been chosen because it is deemed to have the greatest chance of success as a proof of concept for future inertial fusion experiments. In central hotspot ignition schemes, fusion fuel pellets are compressed and heated in a brief period of intense irradiation from an external driver. Heating and compression then creates a small region of burning plasma at the centre of the fuel pellet in which fusion interactions are occurring. The fusion burn wave will then spread rapidly from this burning region, through the remaining compressed fuel before the confinement of the plasma is lost. In current experiments, inertial timescales are on the order of ten nanoseconds.

1.4.1 Drive phase

In the drive phase of an inertial fusion experiment, isotopes of hydrogen are heated and compressed using a high energy driver, commonly in the form of a laser beam. It is hoped that the heating and compression will initiate creation of a dense plasma, in which fusion reactions can take place. As the isotopes of hydrogen used are planned to be deuterium and tritium, the end products are helium nuclei and neutrons which will carry a high net yield energy output. The fuel capsule design for inertial fusion concepts generally incorporates an outer layer of a plastic material which has a high coupling to the incident driver radiation. This outer layer covers a thicker inner layer of cryogenic deuterium-tritium ice. This cryogenic ice layer encases a central sphere of deuterium-tritium gas. The purpose of the thin outer layer is to absorb the driver energy and to ablate under illumination from this driver. Conservation of momentum means that the radially outward ablation of material exerts a radially inwards compressing force on the fuel layers beneath the ablator layer. This compression results in pressures on the order of 10^6 times atmospheric pressure, equivalent to $P = 100\,\mathrm{GPa}$. The central fuel is compressed to a density on the order of $\rho = 1000\mathrm{gcm}^{-3}$ and the work done on this fuel by the compression forces significantly raises the internal energy of the material, increasing its temperature by PdV heating. Sufficient density and temperature must be produced such that a small region of burning plasma is created in the centre of the fusion fuel. It is from

this region that the alpha heating burn wave is initiated and the release of fusion energy is begun.

The success of the inertial confinement fusion project is heavily dependent upon whether or not a design can be conceived which will successfully initiate a burn wave. The burn wave is a sequential heating process which is mediated by the kinetic energy deposition interactions of fusion produced alpha-particles. Using external drivers to provide sufficient heating and compression to raise the entire fuel pellet to fusion conditions would require vastly too much energy to be viable as an efficient form of power generation. A major advantage of the burn wave concept is that it utilises the excess energy of fusion produced alpha-particles to provide this extra required heating.

1.4.2 Burn phase

The burn phase describes the time during which the energy from fusion produced alpha-particles is being used to heat the compressed fuel which neighbours the hotspot up to fusion temperatures. The fusion alpha-particles will deposit more kinetic energy per unit distance travelled in the cool dense outer fuel region than they deposit in the hotspot. This will aid the heating process because this energy deposition will increase the temperature of the dense fuel. This is because the fusion alpha-particles will experience a greater stopping power in the cooler, denser fuel ($T \sim 10^6\,\mathrm{K}, n_e \sim 10^{27}\,\mathrm{cm}^{-3}$) that is outside of the fusion hotspot ($T \sim 10^8\,\mathrm{K}, n_e \sim 10^{25}\,\mathrm{cm}^{-3}$). The target fusion conditions for the fuel are at a temperature of approximately $10^8\,\mathrm{K}$ and a density of approximately $1000\,\mathrm{gcm}^{-3}$ [Glenzer et al. [2011a]]

The configurations suggested for successful inertial confinement fusion will cause the initiation of very large temperature and density gradients within the fuel capsule. It is hoped that a small region of plasma will be at sufficient temperature and density conditions to be able to locally satisfy the Lawson criterion given in equation 1.13. However, this will not initially be true for the whole body of the plasma fuel as the compressed fuel that surrounds the hotspot region will be of higher density and lower temperature. In order for any inertial fusion concept to work, further plasma heating must occur after the drive phase has ended through the process of fusion alpha heating. It is hoped that the region of fusion temperature plasma, created in the central region of the capsule, will spread radially outwards. The energy required for this process is predicted to come from the charged alpha-particle fusion products which will be quickly stopped within the fuel once a fusion reaction occurs. Modelling some of the energy transfer processes of this burn phase

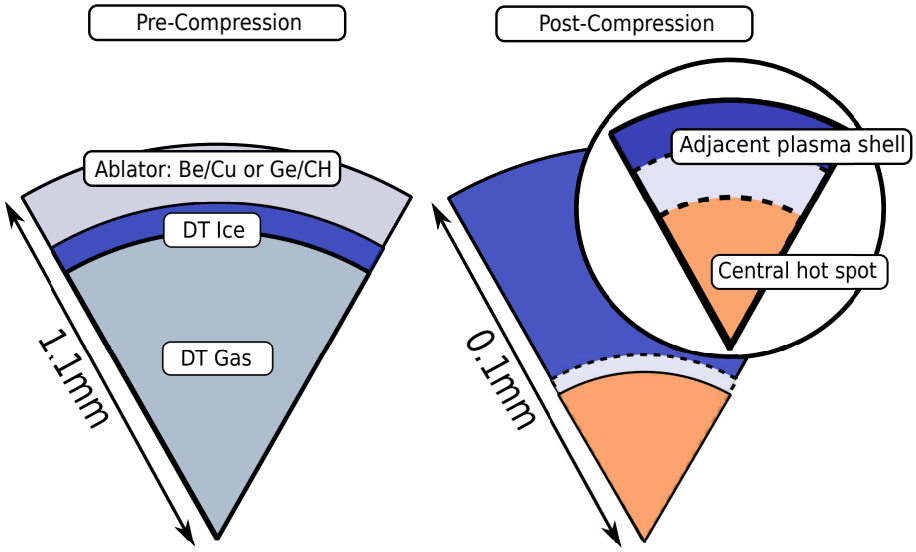

Figure 1.2: Diagram of the internal structure of an inertial confinement fuel pellet pre-compression and post-compression. The layering of the pellet structure, in the fashion shown here, aids stability of compression whilst providing a sufficient fuel source for fusion.

is the topic of research being investigated in chapter 5 of this thesis.

1.4.3 Capsule structure and Inertial Fusion Configurations

One element of inertial fusion that remains unchanged across different experiment designs is the basic structure of the fuel capsule. Although the capsule design has many subtleties introduced for optimisation of each case, there are basic principles which are mostly agreed throughout. Firstly, all inertial fusion concepts need to work at very high densities. Since these densities are much higher than those of the initial fuel pellet used in the proposed NIF design, the ignition of a fuel pellet will require an initial phase in which the fusion fuel undergoes extreme compression and heating. For effective compression of such a fuel capsule, it is desirable to suppress instabilities, such as Rayleigh-Taylor, which will cause mixing of the cooler denser fuel into the fusion hotspot. The fuel capsule is spherical in shape because the symmetry greatly aids stability of the compression design. Further to this, most designs incorporate a layered structure to the fuel target, i.e. an ablator layered over deuterium-tritium ice, layered over deuterium-tritium gas. One simple, early inertial fusion configuration is the direct drive, central hotspot configuration. In this design the capsule compression happens by the ablation method described earlier

and the driver radiation is incident directly onto the outer ablator layer of the fuel pellet. However, calculations imply that this direct drive design is not the optimal design for energy efficiency. Current prominent fusion experiments such as the National Ignition Facility and Laser Mega-Joule all run in an indirect drive configuration. In the indirect drive configuration, the initial drive energy is not incident of the capsule directly, but is incident on some intermediate body which then emits radiation that irradiates the fuel capsule to initiate the compression. The industry standard design for this intermediate body is the hohlraum which is an open ended, cylinder which the fuel pellet is placed inside. Some designs propose using Uranium-238 for this cylinder, though the material chosen for the Hohlraum on the National Ignition Facility is gold. The light from the laser driver enters the hohlraum through the two 'laser entry holes' at each end of the cylinder. Inside, the laser irradiates the walls of the hohlraum, ionising the gold. The super heated gold plasma emits x-rays, which then provides an isotropic, uniform source of high power illuminating radiation for the fuel capsule. Of the laser energy which enters the Hohlraum, roughly 80% is converted to x-rays. However, this conversion means that the capsule illumination is delivered at a higher photon energy than the original driver, which is beneficial because it offers an increased energy coupling to the ablator target. Indirect drive configurations are commonly used in fusion experiments because the resulting illumination of the fuel capsule is less sensitive to non-uniformities in the laser driver than designs in which the laser is directly incident on the fuel pellet. Another major advantage of indirect drive is that the increased uniformity of capsule illumination meant that the compression phase in an indirect drive configuration is less sensitive to hydrodynamic instabilities.

As a simple estimate for the requirements for fusion burn consider a sphere of plasma. Each fusion alpha must lose its energy to the background plasma inside a typical distance, R, where R is the radius of the sphere. The mean free path of the alpha is

$$\lambda_{mfp} = \frac{1}{n\sigma}$$

where n is the number density of ions and σ the collisional cross-sectional area. Hence for a burning plasma, i.e. ignition, a simple estimate leads to the requirement

$$nR > \frac{1}{\sigma}$$

Multiplying by the average ion mass and using the measured cross-section gives $\rho R > 0.3$ g/cm^2. However, the fraction of D-T fuel burnt Φ_B in a spherical burning

plasma is given by

$$\Phi_B = \frac{\rho R}{\rho R + 6}$$

Hence for a significant fraction of the fuel to burn we need $\rho R > 3$ g/cm^2 which is an order of magnitude more stringent that the condition for ignition. The central hot-spot ignition scheme relies on a pellet which has a D-T gas sphere surrounded by a shell of D-T ice. Under compression the PdV heating of the gas shell lead to a hot core with $\rho R > 0.3$ g/cm^2 thus initiating a fusion burn wave. This then ignites, and burns, the higher mass density imploding ice shell such that for the whole fuel pellet $\rho R > 3$ g/cm^2 and a significant burn fraction is achieved. In addition to this simple energy budget requirement on ρR there is also an upper limit on the total mass of D-T fuel which can be burnt in a single shot. The limit on the mass comes from the maximum energy which can be released per shot of 10 - 100 MJ. This energy limit is set by the maximum energy which can be released per shot without damaging the vacuum vessel. For such a total mass of fuel

$$M = \frac{4\pi}{3}\frac{\rho R}{\rho}$$

gives a requirement that $\rho \simeq 300$ g/cm^3 which compared to liquid D-T density of $\rho = 0.225$ g/cm^3 means the fuel pellet must be compressed by a factor of over a thousand. Furthermore so that this compression has a combined PdV plus alpha heating rate for the gas D-T hot spot which exceeds the radiative and thermal cooling this compression must be done at an implosion velocity of $300 - 400$ km/s. Critical to this whole hot-spot design therefore is a thorough understanding of alpha stopping in both compressed gaseous and solid D-T fuel.

1.4.4 Progress made by the national ignition facility (NIF)

Currently, the most prominent inertial fusion experiment in the world is the National Ignition Facility (NIF), built at Lawrence Livermore National Laboratories in Livermore, California. The NIF was designed to demonstrate the ignition concept for the first time in a laboratory inertial fusion device. Originally completed in March 2009, the NIF is still the largest inertial confinement fusion experiment in the world and also the largest laser experiment in the world. The NIF laser system irradiates the test fusion fuel pellets with 192 laser beam lines at a power of approximately $P \approx 500\,\mathrm{TW}$, delivering a total energy payload of $E \approx 1.8\,\mathrm{MJ}$ in the ultra-violet wave-band. The NIF has opted for the indirect drive, central hotspot configuration for increased energy coupling to the capsule and higher energy efficien-

cies. The conversion of the initial infra-red pulse to an ultra-violet driver is chosen because the energy coupling of the infra-red photons is stronger with the hot electrons from parametric instabilities. These have a threshold and growth rate which scales $\sim I\lambda^2$, where I is the laser intensity and λ is the wavelength. This causes a greater energy transfer from the laser driver to the light, penetrative electrons. These electrons can then be accelerated into the capsule core, transferring energy to the plasma and prematurely heating the fuel. This is not desirable because the resulting temperature increase of the core reduces the achievable compression in the core, which decreases the observed fusion rate.

The NIF was never designed to be used as a power plant and has no mechanism for utilising the energy produced from the fuel capsules. Purely aimed as a proof of concept the NIF test shots mostly use a reduced gain tritium-hydrogen-deuterium fuel mixture in the fuel pellets. This was intended to allow the investigation of the burn physics whilst maintaining a low neutron flux onto the target chamber walls. Experiments at the NIF have managed to demonstrate a suitable drive temperature for inertial fusion and also have shown great improvements in the capsule compression. The stability of this compression has caused problems in the past but recent advances such as exploitation of cross beam transfer have allowed for greater capsule illumination isotropy and improved stabilisation of the capsule shaping under compression. Unfortunately, the NIF has so far been unable to demonstrate a burning plasma in a laboratory but much progress has been made and it is hoped that this progress will continue at the same rate with work being performed on the upcoming Laser Mega-Joule experiment built near Bordeaux in France.

The work in this thesis can be applied to some of the plasma regimes that are created in inertial fusion experiments but a wider field of application is that of high energy density matter research. In this field, a wider range of techniques are employed for the creation and investigation of dense plasmas without the constraints of achieving laboratory fusion and with the simple aim of increasing understanding of exotic forms of matter [Spiller and Franchetti [2006]]. The GSI Helmholtz Centre for Heavy Ion Research in Darmstadt and its upcoming successor the Facility for Antiproton and Ion Research (FAIR) have many such experiments in which ion beams and x-ray sources are used to probe laboratory plasmas in the warm dense matter regime [Tahir et al. [2011]]. The approaches to particle energy transfer described in the following chapters are of particular use when attempting to theoretically model the use of ion beams in probing dense plasmas.

1.5 Summary of the thesis

This concludes the introduction to the topic of energy transfer processes in burning fusion plasmas. The next chapter will offer a significantly more detailed introduction to the theoretical basis of calculating energy transfer through particle interactions and ion stopping power. Chapter 3 describes the modelling of scattering interactions in ionised and partially-ionised plasma. The scattering and momentum-transport cross-sections that are required for stopping power calculations are also investigated in these regimes. The majority of the simulation work is detailed in chapters 4 and 5. Chapter 4 regards the inclusion of microscopic density fluctuations into stopping power simulations. This is investigated for a variety of plasma scenarios. The effects of the density variations are quantified in comparison with similar calculations using a uniform homogeneous density treatment. Finally, chapter 5 is on the topic of the effects of electron degeneracy on alpha-particle heating timescales in an inertial fusion scenario. This chapter aims to identify drive conditions and heating regimes in which the effects of electron degeneracy could cause unwanted reduction of the alpha-particle heating rate.

Chapter 2

Theoretical Preface

This chapter covers the theoretical basis of the simulation work that is described in the later work chapters of this thesis. The concept of particle stopping power, which is so central to this thesis, will be introduced and a brief overview of its history given. Following this, the models for stopping power which are used in this work will be described, including an account of their theoretical origin and the regimes in which each model is most applicable.

This chapter will introduce the classical Bethe model for stopping power and some extensions that are suitable for modelling stopping power in dense plasma systems. A polynomial fit will be shown for calculating stopping powers in degenerate electron systems, along with a dynamically screened, quantum kinetic approach which is also applicable to degenerate electron systems. These will be compared and the advantages of each model discussed. Also, a model will be introduced that is most applicable to non-degenerate systems which uses a binary collision approximation. This model is used to better model the effects of strong coupling in particle stopping scenarios, such as large angle scattering. Theoretical expansions beyond the models presented here will be delivered in later chapters in order to divide the presentation of theory topics. In this way, we introduce new information as and when it becomes relevant to the topic of investigation.

2.1 Charged particle stopping power

Numerous fields of current scientific research involve the transfer of energy to a given system of interest by employing a beam of fast particles. A large amount of this research uses charged particles because the Coulomb force presents an effective mechanism for accelerating these beam particles to the desired energies. A

charged particle passing through a dense, ionised, partially ionised or solid medium will commonly interact with the electrons and ions of this medium. The charged particle transfers its kinetic energy to the stopping medium through interactions such as elastic and inelastic scattering and both excitation and de-excitation processes. Combining the cumulative effect of all such processes on the energy loss of the beam, we can begin to quantify the interaction of the beam with the external medium on a macroscopic scale. This combined energy loss is generally expressed per unit time or unit length travelled by the beam particles and is referred to as the 'stopping power' of the external medium.

Modern stopping power models need to account for the effects of energy loss from inter-particle collisions. The complete range of possible collisional interactions is extremely extensive and the contributions of each interaction type can change, depending on the internal properties of the stopping medium. Target systems which have different stopping materials, ionisation states or of vastly different densities often require quite a different physical treatment in order to correctly predict their particle stopping power. There are many stopping power models that exist and throughout this chapter, the models that feature most prominently in this work will be reviewed in detail.

2.1.1 Overview of classical stopping power models

In the early 1900s, Ernest Rutherford utilised the scattering behaviour of charged particles to demonstrate the nuclear nature of atoms. This was achieved by measuring the scattering angles of an incident beam of alpha-particles on a gold foil target. Rutherford's investigations into particle scattering and the development of the Rutherford differential scattering cross-section were the initial building blocks of the field of charged particle stopping power.

In 1930, Hans Bethe developed the first model of stopping power [Bethe [1930]] which can be arrived at from classical arguments of momentum transfer to target electrons via the Coulomb potential of the incident particles. The same model can also be derived by integrating over the differential scattering cross-section, $d\sigma$, and the scattering interaction's associated energy loss,

$$-\frac{dE}{dx} = n_e \int d\sigma \cdot \Delta E, \tag{2.1}$$

where E is the energy of a particle, σ is the scattering cross-section, n_e is the electron number density of the stopping material and $-\frac{dE}{dx}$ is the rate of energy loss per unit length travelled by the particle. Originally, Bethe performed his investigations for

cold, solid matter where the dominant contribution to the total stopping power is from electron scattering interactions. The result of this calculation gives,

$$-\frac{dE}{dx} = \frac{e^4}{4\pi\epsilon_0^2}\frac{Z_b^2 n_e^{\text{bound}}}{m_e v_b^2}\ln\left(\frac{b_{\max}}{b_{\min}}\right), \tag{2.2}$$

where Z_b is the charge of the beam particles, n_e^{bound} is the number density of bound electrons in the solid target material, v_b is the velocity of the incident ion and $b_{\min/\max}$ are the minimum and maximum impact parameters for the particle collisions, which define the integration limits for the scattering cross-section. The evolution of the logarithm is approximated in many ways but to begin, for a non-relativistic case, we will simply use the following

$$-\frac{dE}{dx} = \frac{e^4}{4\pi\epsilon_0^2}\frac{Z_b^2 n_e^{\text{bound}}}{m_e v_b^2}\ln\left(\frac{2mv_b^2}{I}\right). \tag{2.3}$$

I is the approximate energy required for an ionisation interaction, known as the effective ionisation potential. The number density of bound electrons in the target and the effective ionisation potential are the only information in the Bethe model which describes the target medium. In 1933, Felix Bloch proposed an effective ionisation potential of ten electronvolts multiplied by the atomic number of the stopping medium.

The particle energy loss, as described in equation (2.3), is shown in figure 2.1 so that its functional form can be observed. It can be seen that the stopping power is heavily dependent on the velocity of the charged particle beam but also that the stopping power is maximised at an intermediate velocity, rather than being maximal at an extreme value of velocity. Due to the nature of the logarithmic term in the Bethe formula, very small beam velocities give a strongly negative stopping power. However, this behaviour is a mathematical artefact and there is no experimental evidence to support the occurrence of these negative stopping power values.

Qualitatively, particle stopping occurs in the following way. When a fast charged particle enters a stopping medium it interacts with surrounding particles and begins to lose energy. Assuming that the particle was initially fast enough that the stopping power begins in the logarithmic Bethe tail, the stopping power that the particle experiences will begin to increase as the particle loses energy. The stopping power is maximised when the particle reaches the velocity at which the scattering cross-section is maximised. Generally, this velocity is where the incident particle velocity is approximately equal to the thermal velocity of the scattering electrons $v_{th} = \sqrt{k_B T/m_e}$. Referring back to equation 2.1 we can see the dependence of the

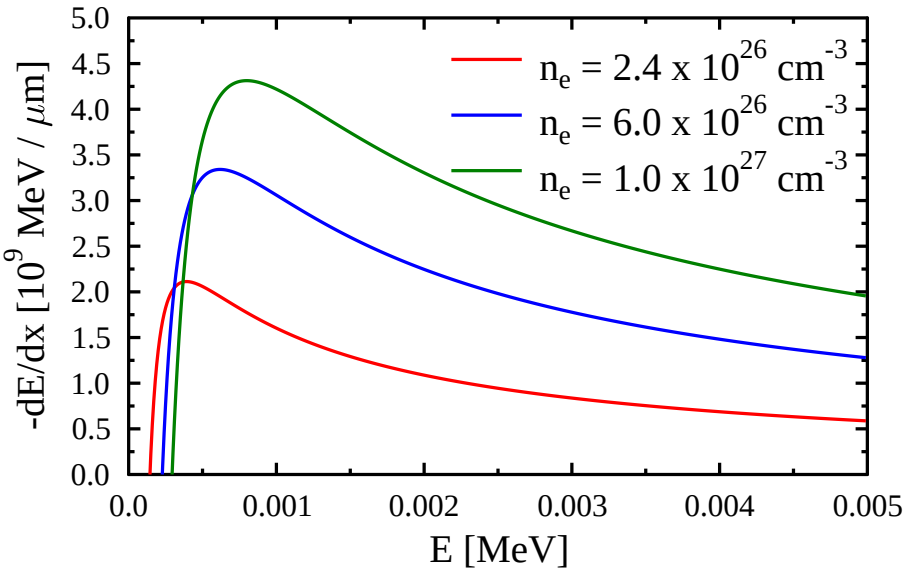

Figure 2.1: Example of the functional form of stopping power using the Bethe formula. These curves are calculated for cold electron stopping of zirconium 40+ ions at varying electron densities. The figures highlight the functional form of the stopping power, showing the maximum and the logarithmic tail for higher beam velocities. Also it should be noted that these curves do not intersect the origin. This is an unphysical result that can occur at low particle energies in the Bethe formalism. Here the logarithmic term dominates and the stopping power tends to negative infinity. This behaviour is not observed in experiment.

stopping power upon the scattering cross-section. It is this behaviour that causes the stopping power to be maximised around the target thermal velocity because the scattering interaction cross-section is also maximised at this point. As the velocity decreases further below this value, the interaction cross-section also begins to decrease and the observed stopping power is reduced. This process continues until the particle comes to rest or leaves the target medium.

When calculating the stopping power of a plasma rather than a solid body, the complexity of possible interactions is increased and several more effects need to be accounted for. These effects are such things as increased contributions to the stopping power from free electrons since the kinetic energy of the incident beam is transferred more efficiently to free electrons than it is to bound electrons. One effect of this is that, for a Bethe-like model, we replace the effective ionisation potential by the electron plasma frequency multiplied by the Planck constant,

$$-\frac{dE}{dx} = \frac{e^4}{4\pi\epsilon_0^2}\frac{Z_b^2 n_e}{m_e v_b^2}\ln\left(\frac{2mv_b^2}{\hbar\omega_{pe}}\right). \tag{2.4}$$

The Bethe model shown here has limited ranges of validity for this work and is applied in a few cases to fast particles in high temperature, low density plasmas. Although the logarithmic tail stopping power values, i.e. high incident velocity values, can show good agreement with more comprehensive models, the behaviour of this Bethe model below the Bragg peak can still give unphysical results, such as negative stopping power, for many parameters. More recently, stopping power models in plasmas have progressed from the logarithmic, Bethe formalism to a more complete, kinetic approach to modelling the system. These stopping power models are often sufficient to accurately model stopping power in dense plasmas where effects of electron degeneracy, increased coupling and collective effects begin to manifest. The details of the physical treatments employed in these models can be quite complex and so, for the purposes of this thesis, require their own description.

2.2 Thomas-Fermi Numerical Stopping Model

The Bethe model has been extended in many works in order to more accurately describe stopping power outside the regime of cold electron stopping in solid matter. There is one such numerical model that is employed in this work which is used for its accurate representation of the stopping power of degenerate electron systems in dense plasmas. The numerical interpolation model that is used here has been provided by Professor Steven Rose of Imperial College, London. The model originally obtained densities from an integration over the Thomas-Fermi ion sphere and so for convenience will be referred to as the 'Thomas-Fermi Model'.

The computational complexity of the Thomas-Fermi model that we employ is significantly less than solving for electron stopping powers using the full Lenard-Balescu Random Phase Approximation (RPA) dielectric approach which will be described in the next section. As a result, the work presented in this thesis often employs the Thomas-Fermi model for time-evolved simulations of energy deposition in degenerate electron systems. Each simulated density and temperature regime requires an initial benchmark to be made, which compares the calculated stopping powers for the Lenard-Balescu RPA dielectric model and the Thomas-Fermi model. In the regimes where good agreement is observed between the stopping powers, the Thomas-Fermi model is chosen as the logical option for computational implementation because of the increased efficiency that it offers for calculating stopping

powers.

2.2.1 Physical basis of the Thomas-Fermi model

The basis of this Thomas-Fermi model is a stopping formula of similar functional form to the Bethe model. It shares the same prefactors, it has an inverse squared dependence on the beam velocity and it also employs a Coulomb logarithm. However, the Thomas-Fermi model has been extended from the Bethe model to offer a description of electron degeneracy.

To account for effects of degeneracy, the model employs a Brysk correction controlled by a switching function in the fashion of the model of Li and Petrasso [Li and Petrasso [1993]]. The density is calculated from an integration over the Thomas-Fermi ion sphere and the electron thermal velocities are calculated from a Fermi integral over the chemical potential. In this way, a Bethe-like approach can be taken to calculating the stopping power and the electron velocities will still be calculated accurately even after the electron system of the plasma leaves the classical regime.

2.2.2 Origin of Thomas-Fermi stopping model

In the Thomas-Fermi model, collisional interactions are handled in the same fashion as the Bethe model i.e. they are described by an integration over the total differential scattering cross-section, which results in a Coulomb logarithm of some form. However, specifically the Thomas-Fermi model uses a Pade approximation in the calculation of its Coulomb logarithm which is a polynomial aimed at interpolating a fit between four of the Coulomb logarithms that are most relevant to stopping power in dense, degenerate electron systems. The result is that whichever Coulomb logarithm is largest, is dominant and is used in the stopping power formula. These Coulomb logarithms are as detailed in the 1977 works of Stanley Skupsky [Skupsky [1977]]. For the non-degenerate case, the standard logarithm from the Bethe model is used. For the case of weak degeneracy, the logarithm that is employed is

$$\ln \Lambda = \frac{1}{2}\left[\ln\left(1+\Lambda_S^2\right) - 2\right] \tag{2.5}$$

and Λ_S, which is described as the 'standard argument of the Coulomb logarithm', is given as follows

$$\Lambda_S = \sqrt{\frac{12 m_e T_e}{\hbar^2 k_D^2}} \tag{2.6}$$

k_D in this case is the Debye wave number which is defined as

$$k_D^2 = \frac{4\pi n_e e^2}{T_e} \tag{2.7}$$

For the case of strong degeneracy, another modified Coulomb logarithm is used

$$\ln \Lambda_{\mathrm{RPA}} = \frac{1}{2}\left[\ln\left(1+\Lambda_D^2\right) - 1\right] \tag{2.8}$$

and the degenerate Coulomb logarithm is defined in it's simplest form by the expression

$$\Lambda_D^2 = \Lambda_S^2 \left(\frac{T_F}{T}\right)^2 \tag{2.9}$$

and the Fermi temperature term, T_F, can be written as

$$T_F = \frac{2}{3}\eta T \tag{2.10}$$

where η is a degeneracy parameter that is chosen such that [Skupsky [1977]]

$$\int d\mathbf{v} \cdot 2\left(\frac{m}{h}\right)^3 \left[\exp\left(\frac{mv^2}{2T} - \eta\right)\right]^{-1} = n_e \tag{2.11}$$

where m is the electron mass, v is the particle velocity, T is temperature, h is the Planck constant and n_e is the electron number density.

Finally there is an 'interpolated case' for the Coulomb logarithm that Skupsky employs and is given by the following expression

$$\ln \Lambda_{\mathrm{RPA}} = \frac{1}{2}\left[\ln\left(1+\Lambda^2\right) - 1\right] \tag{2.12}$$

and the logarithm term used at the base of this expression is determined by

$$\Lambda = \Lambda_S \sqrt{0.37 + \left(\frac{T_F}{T}\right)^2} \tag{2.13}$$

The Thomas-Fermi stopping model is then formed by plugging the Pade approximated Coulomb logarithm in the Bethe model and multiplying by a degeneracy switching term which is controlled by the value of an error function, similar to the Heaviside function used in the work of Li and Petrasso [Li and Petrasso [1993]]. The general form of the Thomas-Fermi model is shown in equations (2.14-2.16)

$$\frac{dE}{dx} = -\frac{4\pi Z_b^2 e^4}{m_c v_b^2} n_c \ln(\Lambda) \times \left[\mathrm{erf}(x_0) - \left(1 + \frac{m_c}{m_b}\right)\frac{2}{\sqrt{\pi}} x_0 \exp\left(-x_0^2\right)\right], \tag{2.14}$$

where the error function argument is given by

$$x_0 = \left[\frac{m_c \epsilon_b}{m_b k_B T_c}\right]^{1/2} \left[\frac{\sqrt{\pi}}{2I_{1/2}(\eta)[1+\exp(-\eta)]}\right]^{1/3}, \tag{2.15}$$

and the Pade approximation for the Coulomb logarithm is as follows.

$$\Lambda = \frac{2m_e v_e^2}{\hbar\omega_{pe}} \frac{0.321 + 0.259x_0^2 + 0.0707x_0^4 + 0.05x_0^6}{1 + 0.130x_0^2 + 0.05x_0^4}. \tag{2.16}$$

In equations (2.14-2.16) the subscripts refer to a beam particle of species b being stopped by a medium composed of particles of species c, where m represents mass, v represents velocity and Z represents charge state. In the further definitions ϵ_b is the kinetic energy of a beam particle, $\eta = \mu/k_B T$, where μ is the chemical potential and $\omega_{pe} = \sqrt{4\pi n_e e^2/m_e}$ is the electron plasma frequency. The Thomas-Fermi model interpolates between degenerate and non-degenerate limiting cases and reproduces the Lenard Balescu results well for degenerate electron systems. Fig.2.2 shows a brief example of some stopping powers which are calculated using these models. In this figure we can see a case of moderate electron degeneracy ($n_e\Lambda_e^3 \sim 50$) in which already the peak stopping power is reduced in the Lenard-Balescu and Thomas-Fermi models compared to that of the T-Matrix model for non-degenerate plasmas. A more detailed comparison can be seen in Chapter 5 where Fig. 5.2 shows a comparison of these different stopping power models for different cases of density and temperature. The cases show a clear transition between systems with weak and strong electron degeneracy. For the case of a plasma with non-degenerate electrons we see that the Thomas-Fermi and Lenard-Balescu RPA models show good agreement with each other, but give slightly higher values of stopping power than the T-matrix model which is known to work well in this regime. For the case of extreme electron degeneracy Fig. 5.2 shows that the T-matrix model greatly over-estimates the stopping power but that the Thomas-Fermi and RPA models still show a good agreement with each other. Finally, in the case of intermediate degeneracy we see that all of the models give different results with RPA lowest and T-matrix highest.

2.3 General kinetic approach to particle stopping power

The general process for deriving a modern kinetic stopping power model begins with employing a kinetic equation which can adequately describe the system in question. The distribution function of the beam particles is then inserted into this kinetic

equation along with a physical description of the possible collisional interactions in the system between the beam and the target medium. The stopping power is obtained by re-arranging this kinetic equation to express the rate of change of kinetic energy with unit length travelled by the beam particles.

Beginning with a generalised kinetic equation which assumes no particle sinks or sources, it is clear to see that the total time derivative of the beam distribution function is controlled by the collision interaction terms, $\sum_c I_{bc}(\mathbf{p}, t)$.

$$\left(\frac{\partial}{\partial t} + \frac{\mathbf{p_1}}{m_a}\nabla_{\mathbf{R}} - \left[\nabla_{\mathbf{R}} U_a^{\text{ext}}(\mathbf{R}, t)\right]\nabla_{\mathbf{p_1}}\right) f_b(\mathbf{p_1}, t) = \sum_c I_{bc}(\mathbf{p}, t) \tag{2.17}$$

It is generally of interest to be able to model the case of such a beam travelling through a medium of arbitrary particle type. This complete kinetic description can be reduced for beam and target systems that can be assumed to be spatially homogeneous and isotropic with no external forces on the target. In such a system, the partial time derivative of the distribution function describing the particle beam can simply be written as

$$\frac{\partial}{\partial t} f_b(\mathbf{p}, t) = \sum_c I_{bc}(\mathbf{p}, t), \tag{2.18}$$

where the right hand side describes the collisional interactions of the beam particles with the particles of the background medium. The species of the beam particles are denoted with a subscript b and the species of the particles of the medium with a subscript c.

2.3.1 Determining stopping power

Integrating over the beam distribution function, the expectation value of some properties of the beam particles can be extracted. Most commonly for stopping power, this is done for the expectation of the kinetic energy or the momentum of the beam particles. The kinetic energy expectation value can be found by evaluating the following expression

$$\begin{aligned} \langle E \rangle &= \int \frac{d\mathbf{p}}{(2\pi\hbar)^3} \cdot E \cdot f_b(\mathbf{p}). \\ &= \int \frac{d\mathbf{p}}{(2\pi\hbar)^3} \frac{p^2}{2m_b} f_b(\mathbf{p}). \end{aligned} \tag{2.19}$$

Differentiating this with respect to time and inserting the form of the collision term from equation (2.18) into equation (2.19) we can obtain the rate of change of kinetic energy of the beam with respect to time,

$$\frac{\partial}{\partial t}\langle E\rangle = \frac{1}{n_b}\sum_c \int \frac{d\mathbf{p}}{(2\pi\hbar)^3}\frac{p^2}{2m_b} I_{bc}(\mathbf{p}) \tag{2.20}$$

If however, at the point of equation (2.19) the expectation value of the beam particle momentum is solved for, instead of solving for the expectation value of the kinetic energy, then the following equation can be obtained

$$\frac{\partial}{\partial t}\langle p\rangle = \frac{\partial}{\partial x}\langle E\rangle = \frac{1}{n_b}\sum_c \int \frac{d\mathbf{p}}{(2\pi\hbar)^3}\frac{\mathbf{p}\cdot\mathbf{v}}{v} I_{bc}(\mathbf{p}) \tag{2.21}$$

The beam velocity vector, $\mathbf{v}$, has been introduced and is defined as the vector with magnitude equal to the beam velocity and whose direction lies along the direction of travel of the particle beam, which is denoted as the x-direction. In equation (2.21) the velocity is used to extract only the linear forward momentum component of the beam particles. Newton's second law states that the rate of change of momentum is given by a force and so, by considering work done by the beam particles against this force, it is easy to consider equation (2.21) as not being the rate of change of momentum with time, but as the familiar stopping power form of kinetic energy lost per unit length. Stopping powers can be calculated from equation (2.21) by inserting a distribution function that describes the particle beam. For the simple example case of a one-dimensional particle beam, of uniform particle momentum, $\mathbf{p}_b$, the distribution function can be written as

$$f_b(\mathbf{p}) = (2\pi\hbar)^3 n_b \delta(\mathbf{p} - \mathbf{p}_b). \tag{2.22}$$

This process of derivation is the process by which the quantum kinetic models of stopping power that are described in this thesis are derived. By varying the assumptions about the beam distribution, varying the kinetic equations employed and varying the methodology for describing collisions, it is possible to describe the physics of many different particle stopping scenarios.

2.4 Models for collision integrals

Any kinetic particle stopping model will require collisional interactions to correctly evolve the distribution functions of the system. In this section, an overview of some different collision integrals will be presented and the regimes in which they

most effectively describe the dominant contributions to the stopping power will be highlighted.

2.4.1 Kinetic stopping power including dynamic screening

To derive the kinetic stopping power model used here, which includes a description of the effects of electron degeneracy, we will again refer to the generalised process for deriving energy loss models for beam particles using a quantum kinetic equation as previously described in section 2.3. We will specialise that general approach here to our systems by employing a dielectric formalism for calculating the screened potentials [Lindhard [1954]; Ichimaru [1992]; Peter and Meyer-ter-Vehn [1991]]. In this form the rate of change of energy per unit time or length are given by equations (2.20, 2.21). Only the electron interactions are considered in the collision integral sum. Here, the collision integrals for the beam interactions with electrons are expressed in the first Born approximation. The Born approximation is a first order truncation of the Born series expansion, which is a series that is used to express the final state of each scattering interaction [Kremp et al. [2004]].

$$\begin{aligned} I_{be}(\mathbf{p}_b, t) &= \frac{1}{\hbar}\int \frac{d\mathbf{p}_e d\bar{\mathbf{p}}_b d\bar{\mathbf{p}}_e}{(2\pi\hbar)^6} \left|V_{eb}^S\left(\mathbf{p}_e - \bar{\mathbf{p}}_e\right)\right|^2 \\ &\quad \times\delta\left(\mathbf{p}_e + \mathbf{p}_b - \bar{\mathbf{p}}_e - \bar{\mathbf{p}}_b\right) 2\pi\delta\left(E_{eb} - \bar{E}_{eb}\right) \\ &\quad \times\left\{\bar{f}_e\left(1-f_e\right)\bar{f}_b\left(1-f_b\right) - f_e\left(1-\bar{f}_e\right) f_b\left(1-\bar{f}_b\right)\right\} \end{aligned} \tag{2.23}$$

Equation (2.23) gives the Lenard-Balescu collision integrals, where E_{eb} is the sum of the kinetic energy of the electron and the beam particle, V_{eb}^S, is the screened Coulomb potential, $\mathbf{p}_b$ and $\mathbf{p}_e$ are the momenta of the beam particle and the electron that are colliding, f_b and f_e are the distribution functions which describe the beam and the target electron system and terms with an overbar correspond to quantities after the collision, whereas those without an overbar relate to quantities before the collision.

In order to describe the particle interactions in this approach we will be modelling collisions in a screened potential, V^S approximation. The method we use for calculating the effective potential in this model is by screening the bare potentials of the system with the retarded dielectric function [Kremp et al. [2004] p. 136]

$$V_{ab}^s(\mathbf{q}\omega, \mathbf{R}t) = \frac{V_{ab}(q)}{\varepsilon^{R/A}(\mathbf{q}\omega, \mathbf{R}t)} \tag{2.24}$$

The retarded dielectric function $\varepsilon^{R/A}(\mathbf{q}\omega, \mathbf{R}t)$, shown in equation (2.24), describes how the permittivity of the target medium which screens the potential varies with

respect to velocity and frequency of an incident particle using the momentum parameter $\mathbf{q}$ and the frequency ω. The temporal retardation of the screening is described using the spatial coordinate $\mathbf{R}$ and time coordinate t. The general expression given in equation (2.24) describes the screened potential between two particles a and b within the plasma, described as a modified Coulomb interaction potential. By using a reduced interaction scheme we can form an expression to calculate the dielectric function explicitly. This random phase approximation (RPA) scheme was originally conceived in 1953 by Bohm and Pines [Bohm and Pines [1953]]. RPA considers only the lowest order two-vertex Feynman diagrams of particle interactions between particles of the same species. The real and imaginary parts of the retarded dielectric function can be written in the following form [Kremp et al. [2004]].

$$\begin{aligned} \mathrm{Re}\,\varepsilon(\mathbf{q},\omega) &= 1+\sum_{\alpha,s_\alpha^2}\frac{4\pi\hbar^2e_a^2}{q^2}\mathcal{P}\int\frac{d\mathbf{p}}{(2\pi\hbar)^3}\frac{f_a(\mathbf{p}+\mathbf{q})-f_a(\mathbf{p})}{\hbar\omega+E_a(\mathbf{p})-E_a(\mathbf{p}+\mathbf{q})} \quad (2.25)\\ \mathrm{Im}\,\varepsilon(\mathbf{q},\omega) &= \sum_{\alpha,s_\alpha^2}\frac{4\pi\hbar^2e_a^2}{q^2}\int\frac{d\mathbf{p}}{(2\pi\hbar)^3}\pi\hbar\delta\left(\hbar\omega+E_a(\mathbf{p})-E_a(\mathbf{p}+\mathbf{q})\right)\\ &\quad\times\{f_a(\mathbf{p})-f_a(\mathbf{p}+\mathbf{q})\} \quad (2.26)\end{aligned}$$

In equations (2.25) and (2.26), the 1 from the real component is the vacuum value and the other terms describe the effect of the medium on the dielectric function. The prefactor, $\frac{4\pi\hbar^2e_a^2}{q^2}$ is the Coulomb potential because the particles being described have charge. The energy difference terms $(\hbar\omega+E_a(\mathbf{p})-E_a(\mathbf{p}+\mathbf{q}))$ ensures energy conservation during the excitation or de-excitation interactions. The momentum difference terms $(f_a(\mathbf{p})-f_a(\mathbf{p}+\mathbf{q}))$ are included to describe the change in excitation energy which results from a particle changing state during an excitation or de-excitation interaction. We now take this generalised expression and impose a thermodynamic equilibrium onto the plasma system that we are modelling. Now we know that for Fermions, such as an electron gas, we can assign the electron gas a Fermi distribution and so include a treatment of degeneracy in this manner. In this case, the distribution function will be given by

$$f_a(p)=\frac{1}{\exp\left[\beta\left(\frac{p^2}{2m_a}-\mu_a\right)\right]+1} \quad (2.27)$$

where we use $\beta=1/k_BT$ and the chemical potential is denoted by μ_a. Enforcing this form of the distribution function allows a convenient analytical form to be used for the imaginary part of the dielectric function. This form uses the symbolic

abbreviation,

$$E_a^{\pm} = \left(\pm \frac{q}{2} - \frac{m_a \hbar \omega}{q} \right)^2, \tag{2.28}$$

and allows the imaginary part of the dielectric function for a plasma in thermodynamic equilibrium to be neatly expressed as [Gluck [1971]]

$$\operatorname{Im} \varepsilon(\mathbf{q}, \omega) = \sum_{\alpha, s_\alpha^2} \frac{m_a^2 e_a^2 k_B T}{\hbar q^3} \ln \left\{ \frac{1 + \exp\left[\beta \left(-\frac{E_a^-}{2m_a} + \mu_a \right) \right]}{1 + \exp\left[\beta \left(-\frac{E_a^+}{2m_a} + \mu_a \right) \right]} \right\} \tag{2.29}$$

This real and imaginary component form is what will be required for the calculation of stopping power in the dielectric model used in this work.

Lenard-Balescu Random Phase Approximation (RPA) dielectric function stopping power

In the previous section, we mentioned an approximate method for calculating the dielectric function from the work of Bohm and Pines [Bohm and Pines [1953]]. The Random Phase Approximation, RPA, considers only the lowest order two-vertex Feynman diagrams of particle interactions between particles of the same species and so by neglecting the effects of higher order interaction paths, we were able to write the imaginary component of the dielectric function explicitly in equation (2.26). In this section, a derivation of an expression for a Lenard-Balescu RPA dielectric function expression for the stopping power will be shown [Kraeft and Strege [1988]; Gericke et al. [1996]; Arista and Brandt [1981]]. For the case of this derivation, the distribution function $f_b(\mathbf{p}_b, t)$ will be defined as a particle beam with finite velocity and a fixed direction of travel which will be defined here as the x-direction. This derivation requires some assumptions namely that

- There is a short initial time interval of plasma equilibrium which allows the application of the dielectric function for calculating the screened potential.
- The spatial density of the beam particles is sparse enough such that interactions between beam particles can be neglected
- The beam particle distribution function is sharply peaked, which is required in our calculation of the collision integral. The distribution function of the beam is defined in equation (2.22)

Now, for convenience of transcription, the following notation for the momenta will be used

$$\mathbf{p}_b = \mathbf{p} \qquad \mathbf{p}_e = \mathbf{p}' \tag{2.30}$$

we plug equation (2.23) into equation (2.21) which gives us an extensive integral form for the stopping power of a weakly coupled electron gas using the RPA dielectric function description of the screening.

$$\begin{aligned}\frac{\partial}{\partial x}\langle E\rangle &= \frac{1}{n_b}\int \frac{d\mathbf{p}}{(2\pi\hbar)^3}\frac{\mathbf{p}\cdot\mathbf{v}}{v}\frac{1}{\hbar}\int \frac{d\mathbf{p}'d\bar{\mathbf{p}}d\bar{\mathbf{p}}'}{(2\pi\hbar)^6}\left|\frac{V_{eb}\left(\mathbf{p}'-\bar{\mathbf{p}}'\right)}{\varepsilon^R\left(\mathbf{p}'-\bar{\mathbf{p}}', E(p')-E(\bar{p}')\right)}\right|^2 \\ &\times\delta\left(\mathbf{p}'+\mathbf{p}-\bar{\mathbf{p}}'-\bar{\mathbf{p}}\right)2\pi\delta\left(E(p)+E(p')-E(\bar{p})-E(\bar{p}')\right) \\ &\times\left\{\bar{f}_e\left(1-f_e\right)\bar{f}_b\left(1-f_b\right)-f_e\left(1-\bar{f}_e\right)f_b\left(1-\bar{f}_b\right)\right\}\end{aligned} \tag{2.31}$$

where V_{eb} is the scattering potential, ε^R is the retarded dielectric function screening the potential, quantities with over-bars are values prior to the collision and quantities without over-bars are post collision. It is assumed that the kinetic energies here behave as $E = p^2/2m$. The dielectric function provides dynamic screening of the electron potential. From the beam density assumption it follows that the value of the beam distribution function is small, i.e. $f_b << 1$. Then it is necessary to define a transfer momentum and a transfer energy

$$\begin{aligned}\mathbf{k} = \mathbf{p}-\bar{\mathbf{p}} \qquad & -\mathbf{k}' = \mathbf{p}'-\bar{\mathbf{p}}' \\ \hbar\omega = E(p)-E(\bar{p}) \qquad & -\hbar\omega' = E(p')-E(\bar{p}')\end{aligned} \tag{2.32}$$

Introducing this transfer momentum, transfer energy and the discussed form of the beam distribution (2.22), which allows terms of $(1-f_b)$ to be treated as unity before and after the collision, allows equation (2.31) to be expressed in a compacted form with the addition of some delta functions to enforce the transfer momentum and energy relations.

$$\begin{aligned}\frac{\partial}{\partial x}\langle E\rangle &= 2\pi\hbar(2\pi\hbar)^6\int\frac{d\mathbf{p}}{(2\pi\hbar)^3}\frac{d\mathbf{p}'}{(2\pi\hbar)^3}\frac{d\mathbf{k}}{(2\pi\hbar)^3}\frac{d\mathbf{k}'}{(2\pi\hbar)^3}\int d\omega d\omega'\frac{\mathbf{p}\cdot\mathbf{v}}{v} \\ &\times\left|\frac{V_{eb}\left(-k'\right)}{\varepsilon^R\left(-k',-\hbar\omega'\right)}\right|^2\delta\left(\mathbf{k}-\mathbf{k}'\right)\delta\left(\hbar\omega-\hbar\omega'\right)\delta\left(\hbar\omega-E(\mathbf{p})+E(\mathbf{p}-\mathbf{k})\right) \\ &\delta\left(\hbar\omega'-E(\mathbf{p}'+\mathbf{k}')+E(\mathbf{p}')\right)\left\{\delta\left(\mathbf{p}-\mathbf{k}-m\mathbf{v}\right)f(\mathbf{p}'+\mathbf{k}')\left(1-f(\mathbf{p}')\right)\right. \\ &\left.-\delta(\mathbf{p}-m\mathbf{v})f(\mathbf{p}')\left(1-f(\mathbf{p}'+\mathbf{k}')\right)\right\}\end{aligned} \tag{2.33}$$

performing the available delta function integrals over k and ω allows this expression to be simplified considerably, but results in the equation being separated into two terms

$$\begin{aligned}\frac{\partial}{\partial x}\langle E\rangle &= 2\pi\hbar\int\frac{d\mathbf{k}}{(2\pi\hbar)^3}\int d\omega\left|\frac{V_{eb}(\mathbf{k})}{\varepsilon^R(\mathbf{k},\omega)}\right|^2\delta\left(\hbar\omega-E(\mathbf{k}+m\mathbf{v})+E(m\mathbf{v})\right)\\ &\times\left\{\frac{(\mathbf{k}+m\mathbf{v})\cdot\mathbf{v}}{v}\int\frac{d\mathbf{p}'}{(2\pi\hbar)^3}\delta\left(\hbar\omega-E(\mathbf{p}'+\mathbf{k})+E(\mathbf{p}')\right)f(\mathbf{p}'+\mathbf{k})\left(1-f(\mathbf{p}')\right)\right.\\ &\left.-\frac{mv^2}{v}\int\frac{d\mathbf{p}'}{(2\pi\hbar)^3}\delta\left(\hbar\omega-E(\mathbf{p}'+\mathbf{k})+E(\mathbf{p}')\right)f(\mathbf{p}')\left(1-f(\mathbf{p}'+\mathbf{k})\right)\right\}\end{aligned}\tag{2.34}$$

Now it is convenient to employ some relations between Fermi and Bose functions. These are mathematical identities used for convenience to equate our existing set of Fermi functions to a combination of Bose functions and the imaginary part of the dielectric function. From these identities it is possible for us to further symmetrise the two terms of equation (2.34) which will further simplify the form. Introducing the Bose distribution, $n_B(\tilde{E})=1/\left[\exp(\beta\tilde{E})-1\right]$, we use the identity

$$f(\mathbf{p})\left(1-f(\mathbf{p}+\mathbf{k})\right)=\left(f(\mathbf{p}+\mathbf{k})-f(\mathbf{p})\right)n_B\left[E(\mathbf{p})-E(\mathbf{p}-\mathbf{k})\right]\tag{2.35}$$

which can be applied to both terms of equation (2.34) using different arguments to the Bose function, although it will be seen that the relation between these arguments will be reduced to a difference in sign between the terms.

$$\begin{aligned}\frac{\partial}{\partial x}\langle E\rangle &= 2\pi\hbar\int\frac{d\mathbf{k}}{(2\pi\hbar)^3}\int d\omega\left|\frac{V_{eb}(\mathbf{k})}{\varepsilon^R(\mathbf{k},\omega)}\right|^2\delta\left(\hbar\omega-E(\mathbf{k}+m\mathbf{v})+E(m\mathbf{v})\right)\\ &\times\left\{\frac{(\mathbf{k}+m\mathbf{v})\cdot\mathbf{v}}{v}n_B(\hbar\omega)\int\frac{d\mathbf{p}'}{(2\pi\hbar)^3}\delta\left(\hbar\omega-E(\mathbf{p}'+\mathbf{k})+E(\mathbf{p}')\right)\right.\\ &\times\left[f(\mathbf{p}')-f(\mathbf{p}'+\mathbf{k})\right]\\ &-\frac{mv^2}{v}n_B(-\hbar\omega)\int\frac{d\mathbf{p}'}{(2\pi\hbar)^3}\delta\left(\hbar\omega-E(\mathbf{p}'+\mathbf{k})+E(\mathbf{p}')\right)\\ &\left.\times\left[f(\mathbf{p}'+\mathbf{k})-f(\mathbf{p}')\right]\right\}\end{aligned}\tag{2.36}$$

Now we employ a Dirac identity [Kremp et al. [2004]], which relates the momentum distribution and Coulomb potential that we have here to the imaginary component

of the dielectric function. This identity is given as

$$\mathrm{Im}\varepsilon = \pi\hbar V_{ee}\int \frac{d\mathbf{p}'}{(2\pi\hbar)^3}\delta\left(\hbar\omega - E(\mathbf{p}'+\mathbf{k}) + E(\mathbf{p}')\right)\left[f(\mathbf{p}'+\mathbf{k}) - f(\mathbf{p}')\right] \tag{2.37}$$

Inserting equation (2.37) into equation (2.37) allows equation (2.36) to be further condensed into the following form

$$\begin{aligned}\frac{\partial}{\partial x}\langle E\rangle &= 2\int\frac{d\mathbf{k}}{(2\pi\hbar)^3}\int d\omega\left|\frac{V_{eb}(\mathbf{k})}{\varepsilon^R(\mathbf{k},\omega)}\right|^2\delta\left(\hbar\omega - E(\mathbf{k}+m\mathbf{v}) + E(m\mathbf{v})\right)\\ &\times\left\{\frac{(\mathbf{k}+m\mathbf{v})\cdot\mathbf{v}}{v}n_B(\hbar\omega)\frac{1}{V_{ee}(\mathbf{k})}\mathrm{Im}\varepsilon(\hbar,\omega)\right.\\ &\left.+\frac{mv^2}{v}n_B(-\hbar\omega)\frac{1}{V_{ee}(\mathbf{k})}\mathrm{Im}\varepsilon(\hbar,\omega)\right\}\end{aligned} \tag{2.38}$$

This gives us a ratio of two Coulomb potentials which is determined by the beam charge, $V_{eb}(\mathbf{k})/V_{ee}(\mathbf{k}) = Z_b$. Also, we are now free to perform a variable transform of $\hbar\omega \to -\hbar\tilde{\omega}$ since the imaginary component of the dielectric function is an odd function. The stopping power is then expressed as

$$\begin{aligned}\frac{\partial}{\partial x}\langle E\rangle &= -2Z_b\int\frac{d\mathbf{k}}{(2\pi\hbar)^3}\int d\omega V_{eb}(\mathbf{k})\,\mathrm{Im}\varepsilon^{-1}(\mathbf{k},\omega)n_B(\hbar\omega)\\ &\times\delta\left(\hbar\omega - E(\mathbf{k}+m\mathbf{v}) + E(m\mathbf{v})\right)\left\{\frac{(\mathbf{k}+m\mathbf{v})\cdot\mathbf{v}}{v} - \frac{mv^2}{v}\right\}\end{aligned} \tag{2.39}$$

The momentum space integral is then free to be separated into spherical component form, and by assuming the kinetic energies are ideal $E(\tilde{p}) = \frac{\tilde{p}^2}{2m}$ and defining a new angular variable in momentum space, $x = \cos\theta_k$ the form of the stopping power can be reduced to

$$\begin{aligned}\frac{\partial}{\partial x}\langle E\rangle &= -\frac{(2\pi)^2 Z_b}{\pi(2\pi\hbar)^3}\int_0^\infty dk k^2 V_{eb}(k)\int d\omega\mathrm{Im}\varepsilon^{-1}(k,\omega)n_B(\hbar\omega)\\ &\times\int_{-1}^{1}dx\delta\left(\frac{\hbar\omega}{kv} - \frac{k}{2mv} - x\right)\frac{kx}{kv}\end{aligned} \tag{2.40}$$

Solving the delta function integration over the x variable, inserting the value of the Coulomb potential as, $V_{ee}(k) = (4\pi e^2\hbar^2)/(k^2)$, and simply expressing the momen-

tum variable as a wave number, i.e. $p = \hbar k$, we then obtain the stopping power in the final form [Gericke and Schlanges [1999]]

$$\frac{\partial}{\partial x}\langle E\rangle = \frac{2Z_b^2 e^2}{\pi v^2}\int_0^\infty \frac{dk}{k}\int_{\frac{\hbar k^2}{2m_b}-kv}^{\frac{\hbar k^2}{2m_b}+kv} d\omega \left[\omega - \frac{\hbar k^2}{2m_b}\right] \mathrm{Im}\epsilon^{-1}(k,\omega) n_B(\omega) \tag{2.41}$$

2.4.2 Binary collision approach to stopping power, describing strong scattering interactions

For systems which do not exhibit electron degeneracy and for systems with a strong coupling between the beam particles and the target electrons, a binary collision approach can be employed for calculating the charged particle stopping power [Sigmund [1982]; de Ferrariis and Arista [1984]; Ordonez and Molina [1994]]. In this section a stopping power model will be described that is best applied to non-degenerate, strongly-coupled plasma.

Previously, with the Lenard-Balescu RPA dielectric approach there were descriptions included of dynamic screening, collective effects in the weak coupling regime and also the effects of electron degeneracy in the stopping medium could be described. However, in the non-degenerate regime ($n_e\Lambda^3 < 1$) the previous approach is no longer computationally sensible to employ. This is because it introduces an unnecessary computational complexity in describing the collective effects which do not contribute significantly to the energy loss in the non-degenerate regimes. Also in the strongly-coupled regime the previous approach is no longer valid because of the assumptions made during its derivation regarding the form of the stopping medium. The previous assumptions also break down here because the Born approximation was used, which is no longer valid once the mean value of the potential energy per particle is comparable to the kinetic energy per particle, as in the case of strong coupling. The advantage of a binary collision approach is that it can describe complex effects such as multiple scattering, large angle scattering and effects of strong correlation which cannot be described correctly when using RPA. The disadvantages of the binary collision model that is used here are that the binary collision approach cannot accurately describe collective effects or any level of degeneracy.

Binary collision stopping power from the Boltzmann kinetic equation

In some situations, RPA will be too simplistic an approximation to correctly describe the system. Some examples of such systems are scattering interactions where the Born approximation is no longer valid or for the explicit description of bound

states. The ladder approximation is employed in these situations, meaning that the second order Feynmann diagram contributions are considered when describing the interaction. This addition allows descriptions of multiple particle screening and Pauli blocking.

Describing the effects of strong correlation using a binary collision model is best done in the framework of a ladder approximation to the quantum Boltzmann kinetic equation. In this derivation, a T-matrix model for scattering interactions in a Debye potential is used. It is assumed that all collisions are binary, i.e. two-body only, and that any long range Coulomb forces in the system are statically screened, reducing their radius of effect. The derivation of this stopping power model involves insertion of the Boltzmann collision integral in the quantum Boltzmann kinetic equation to find the stopping power. The Boltzmann collision integral for binary collisions between particles of momenta $\mathbf{p}'$ and $\mathbf{p}''$, with self energies taken in the ladder approximation, has the following form

$$\begin{aligned} I_a^B(\mathbf{p}',t) &= \frac{1}{V\hbar}\sum_b \int \frac{d\mathbf{p}''d\bar{\mathbf{p}}'\bar{\mathbf{p}}''}{(2\pi\hbar)^9} \left|\left\langle \mathbf{p}'\mathbf{p}'' \left| T_{ab}^R(E) \right| \bar{\mathbf{p}}''\bar{\mathbf{p}}' \right\rangle\right|^2 2\pi\delta(\bar{E}_{12}-E_{12}) \\ &\quad \times\{\bar{f}_a\bar{f}_b(1-f_a)(1-f_b) - f_af_b(1-\bar{f}_a)(1-\bar{f}_b)\}_t \end{aligned} \tag{2.42}$$

The transition probabilities of the two-particle collisions are now defined by the on-shell two-particle T-matrix and so due to the particle number limitation, bound states are excluded. In scattering theory, the T-Matrix describes the relation between the initial and final states of a scattering interaction in which the matrix elements describe all possible scattering interactions through which the initial state will be transformed to the final state. In this way, the T-Matrix is simply a matrix representation of the coefficients of a convergent Born series approximation to the scattering interaction. In this case, the Born series describes an iterative approach to calculating solutions to the Lippmann-Schwinger equation which offers a quantum mechanical approach to two-particle scattering. Solving this equation allows the calculation of the final state of the scattered body from the initial, incident state and the scattering field [Newton [1982]]. Simply inserting these collision terms into the general equation for kinetic stopping power, shown in equation (2.21), gives the following expression for the generalised particle energy loss with respect to time,

$$\frac{\partial}{\partial x}\langle E\rangle = \frac{1}{V\hbar}\frac{1}{n_b}\sum_c \int \frac{d\mathbf{p}'}{(2\pi\hbar)^3}\frac{d\mathbf{p}''}{(2\pi\hbar)^3}\frac{d\bar{\mathbf{p}}'}{(2\pi\hbar)^3}\frac{d\bar{\mathbf{p}}''}{(2\pi\hbar)^3}\frac{\mathbf{p}'\cdot\mathbf{v}}{v}\left|\langle \mathbf{p}'\mathbf{p}''|T^R_{bc}|\bar{\mathbf{p}}''\bar{\mathbf{p}}'\rangle\right|^2$$
$$\times 2\pi\delta(E_{bc}-\bar{E}_{bc})\left\{f_b(\bar{\mathbf{p}}')f_c(\bar{\mathbf{p}}'')-f_b(\mathbf{p}')f_c(\mathbf{p}'')\right\} \quad (2.43)$$

the subscripts printed here represent the beam particles, b and the particles that compose the target medium, c. Imposing the initial uniform single-valued momentum distribution of the beam particles, one can obtain

$$\frac{\partial}{\partial x}\langle E\rangle = \frac{(2\pi\hbar)^3}{V\hbar}\sum_c \int \frac{d\mathbf{p}'}{(2\pi\hbar)^3}\frac{d\mathbf{p}''}{(2\pi\hbar)^3}\frac{d\bar{\mathbf{p}}'}{(2\pi\hbar)^3}\frac{d\bar{\mathbf{p}}''}{(2\pi\hbar)^3}\frac{\mathbf{p}'\cdot\mathbf{v}}{v}\left|\langle \mathbf{p}'\mathbf{p}''|T^R_{bc}|\bar{\mathbf{p}}''\bar{\mathbf{p}}'\rangle\right|^2$$
$$\times 2\pi\delta(E_{bc}-\bar{E}_{bc})\left\{\delta(\bar{\mathbf{p}}'-\mathbf{p}_b)f_c(\bar{\mathbf{p}}'')-\delta(\mathbf{p}'-\mathbf{p}_b)f_c(\mathbf{p}'')\right\} \quad (2.44)$$

Now switching to the centre of mass frame of the collision introduces new co-ordinates, $\mathbf{p}$ and $\mathbf{P}$, which are defined as

$$\mathbf{p} = \frac{m_c\mathbf{p}'-m_b\mathbf{p}''}{m_b+m_c} \quad (2.45)$$
$$\mathbf{P} = \mathbf{p}'+\mathbf{p}'' \quad (2.46)$$

It follows that the generalised prime notation co-ordinates are expressed in the centre of mass frame as

$$\mathbf{p}' = \frac{m_b}{m_b+m_c}\mathbf{P}+\mathbf{p} \quad (2.47)$$
$$\mathbf{p}'' = \frac{m_c}{m_b+m_c}\mathbf{P}-\mathbf{p} \quad (2.48)$$

The T-matrix then transforms as

$$\left|\langle \mathbf{p}'\mathbf{p}''|T^R_{bc}|\bar{\mathbf{p}}''\bar{\mathbf{p}}'\rangle\right|^2 = \delta^2(\mathbf{P}-\bar{\mathbf{P}})\left|\langle \mathbf{p}|T^R_{bc}|\bar{\mathbf{p}}\rangle\right|^2$$
$$= \frac{V}{(2\pi\hbar)^3}\delta(\mathbf{P}-\bar{\mathbf{P}})\left|\langle \mathbf{p}|T^R_{bc}|\bar{\mathbf{p}}\rangle\right|^2 \quad (2.49)$$

where the additional δ-functions are to ensure momentum conservation and the volume term comes from the integral of $\delta(0)$ over all momentum-space.

In order to transform the momentum integral into the centre of mass frame

co-ordinates, the following relations are used

$$\begin{aligned} d\mathbf{p}'d\mathbf{p}'' &= (-1)\, d\mathbf{p}d\mathbf{P} \\ d\bar{\mathbf{p}}'d\bar{\mathbf{p}}'' &= (-1)\, d\bar{\mathbf{p}}d\bar{\mathbf{P}}. \end{aligned} \tag{2.50}$$

Then by inserting the centre of mass T-matrix expression into equation (2.44), one obtains the stopping power expression in the following form,

$$\begin{aligned} \frac{\partial}{\partial x}\langle E\rangle &= \frac{(2\pi\hbar)^3}{V\hbar}\sum_c \int \frac{d\mathbf{p}}{(2\pi\hbar)^3}\frac{d\mathbf{P}}{(2\pi\hbar)^3}\frac{d\bar{\mathbf{p}}}{(2\pi\hbar)^3}\frac{d\bar{\mathbf{P}}}{(2\pi\hbar)^3} \\ &\quad \frac{\left(\frac{m_b}{m_b+m_c}\mathbf{P}+\mathbf{p}\right)\cdot\mathbf{v}}{v}\frac{V}{(2\pi\hbar)^3}\delta(\mathbf{P}-\bar{\mathbf{P}})\left|\langle\mathbf{p}|T^R_{bc}|\bar{\mathbf{p}}\rangle\right|^2 \\ &\quad \times 2\pi\delta\left(\frac{p^2}{2m_{bc}}-\frac{\bar{p}^2}{2m_{bc}}\right) \\ &\quad \left\{\delta\left(\left(\frac{m_b}{m_b+m_c}\bar{\mathbf{P}}+\bar{\mathbf{p}}\right)-\mathbf{p}_b\right) f_c\left(\frac{m_c}{m_b+m_c}\bar{\mathbf{P}}-\bar{\mathbf{p}}\right)\right. \\ &\quad \left.-\delta\left(\left(\frac{m_b}{m_b+m_c}\mathbf{P}+\mathbf{p}\right)-\mathbf{p}_b\right) f_c\left(\frac{m_c}{m_b+m_c}\mathbf{P}-\mathbf{p}\right)\right\} \end{aligned} \tag{2.51}$$

which can be contracted to the following form by rearrangement and evaluating the δ-function integrals over $\mathbf{P}$ and $\bar{\mathbf{P}}$, which gives

$$\begin{aligned} \frac{\partial}{\partial x}\langle E\rangle &= \frac{2\pi}{\hbar}\sum_c \int \frac{m_c^3}{m_{bc}^3}\frac{d\mathbf{p}}{(2\pi\hbar)^3}\frac{d\bar{\mathbf{p}}}{(2\pi\hbar)^3} \\ &\quad \left|\left\langle\mathbf{p}\left|T^R_{bc}\right|\bar{\mathbf{p}}\right\rangle\right|^2 \delta\left(\frac{p^2}{2m_{bc}}-\frac{\bar{p}^2}{2m_{bc}}\right) \\ &\quad \left\{\frac{(\mathbf{p}_b-\bar{\mathbf{p}}+\mathbf{p})\cdot\mathbf{v}}{v}-\frac{\mathbf{p}_b\cdot\mathbf{v}}{v}\right\} f_c\left(\frac{m_c}{m_b}\mathbf{p}_b-\frac{m_c}{m_{bc}}\bar{\mathbf{p}}\right) \end{aligned} \tag{2.52}$$

In this new reference frame, we can use the angular homogeneity of the interaction to separate the integration over momentum space out into angular and radial components. As a first step, angles can now be defined between the momentum vectors to give their relative directions.

$$\begin{aligned}\angle(\mathbf{p},\bar{\mathbf{p}}) &= \theta \\ \angle(\mathbf{p}_b,\mathbf{p}) &= \theta_1 \\ \angle(\mathbf{p}_b,\bar{\mathbf{p}}) &= \theta_2\end{aligned} \tag{2.53}$$

Thus, whilst condensing the integral from equation (2.52), a second variable change can now be performed using the angular coordinates $\cos\theta = x$, $\cos\theta_1 = x_1$ and $\cos\theta_2 = x_2$. Noting the following identity for our spherical co-ordinate system,

$$\cos\theta_1 = \cos\theta\cos\theta_2 + \sin\theta\sin\theta_2\cos\phi_x. \tag{2.54}$$

Now the momentum space integral can be rewritten in spherical component form to express the binary collision stopping power in terms of these new angular variables as the following expression

$$\begin{aligned}\frac{\partial}{\partial x}\langle E\rangle = \frac{(2\pi)^3}{\hbar}\sum_c \frac{m_c^3}{m_{bc}^2}\int_0^\infty \frac{dp}{(2\pi\hbar)^6}p^3\int_{-1}^{1}dx\int_{-1}^{1}dx_2\left|\left\langle\mathbf{p}\left|T_{bc}^R\right|\bar{\mathbf{p}}\right\rangle\right|^2_{|\bar{\mathbf{p}}|=|\mathbf{p}|} \\ \times\frac{\mathbf{p}_b\cdot\mathbf{v}-\bar{\mathbf{p}}\cdot\mathbf{v}+\mathbf{p}\cdot\mathbf{v}-\mathbf{p}_b\cdot\mathbf{v}}{v}f_c\left(\frac{m_c\mathbf{p}_b}{m_b}-\frac{m_c}{m_{bc}}\mathbf{p},\,x_2\right)\end{aligned} \tag{2.55}$$

Then we can use the following relationship to express the on-shell T-matrix term in terms of the differential scattering cross-section [Joachain [1975]]

$$\left|\left\langle\mathbf{p}\left|T_{bc}^R\right|\bar{\mathbf{p}}\right\rangle\right|^2_{|\bar{\mathbf{p}}|=|\mathbf{p}|} = \frac{(2\pi\hbar)^6}{(2\pi)^4\hbar^2 m_{bc}^2}\frac{d\sigma_{bc}(p,\Omega)}{d\Omega} \tag{2.56}$$

In order to condense this expression further, it is convenient to introduce the momentum transport cross-section, $Q_{bc}^T(p)$, which can be defined as

$$Q_{bc}^T(p) = \int_0^{2\pi}d\phi_x\int_{-1}^{1}d\cos\theta(1-\cos\theta)\frac{d\sigma_{bc}(p,\Omega)}{d\Omega} \tag{2.57}$$

The distribution function for the particles of the plasma target medium, denoted by $f_c\left(\frac{m_c}{m_b}\mathbf{p}_b-\frac{m_c}{m_{bc}}\mathbf{p},x_2\right)$, describes a Boltzmann distribution of the form

$$f_c\left(\frac{m_c}{m_b}\mathbf{p}_b - \frac{m_c}{m_{bc}}\mathbf{p}, x_2\right) = n_c\Lambda_c^3 \exp\left(-\frac{m_c}{2k_BT}\left(\frac{p^2}{m_{bc}^2} - \frac{p_b^2}{m_b^2}\right)\right)\exp\left(\frac{m_c p p_b x_2}{m_b m_{bc} k_B T}\right) \tag{2.58}$$

where $\Lambda_c = \sqrt{2\pi\hbar^2/m_c k_B T}$ is the thermal wavelength and n_c is the number density of plasma particles of species c. Then the expression for the full T-matrix stopping power is reached by integrating over the beam momentum for the Boltzmann distribution [Gericke and Schlanges [1999]]

$$\begin{aligned}\frac{\partial}{\partial x}\langle E\rangle &= \frac{-1}{(2\pi)^2\hbar^3}\sum_c \frac{m_c^2}{m_{bc}^3 m_b} n_c\Lambda^3 \frac{k_BT}{v}\int_0^\infty dp\, p^3 Q_{bc}^T(p) \\ &\times\left\{\exp\left(-\frac{m_c}{2k_BT}\left(\frac{p}{m_{bc}} - v\right)^2\right)\left[1 - \frac{m_{bc}k_BT}{m_c p v}\right]\right. \\ &\left. - \exp\left(-\frac{m_c}{2k_BT}\left(\frac{p}{m_{bc}} + v\right)^2\right)\left[1 + \frac{m_{bc}k_BT}{m_c p v}\right]\right\}\end{aligned} \tag{2.59}$$

2.4.3 Combined model: Dynamic screening and strong scattering

Particle stopping cases for plasmas where the velocity of the incident particles is high compared to the thermal velocity of the electrons of the target medium may experience significantly different potential screening to that predicted by the Debye model. This is a result of the finite time with which the plasma electrons relax into their quasi-neutral equilibrium after being perturbed by the incident ion. The Lenard-Balescu, RPA dielectric model for stopping power includes these dynamic effects by default but for the binary collision T-matrix model this effect requires additional treatment. The model described here is a combined model for including dynamic screening into the strong scattering, binary collision approach shown before. This combined model is proposed in the work of Gericke and Schlanges [Gericke and Schlanges [1999]].

The combined model incorporates dynamic screening through introducing a velocity dependent modification to the Debye screening length. The screening length is modified from the typical Debye screening length in the following manner

$$\kappa = \kappa_D\left(1 + \left(\frac{v}{v_{th}}\right)^2\right)^{-1/2} \tag{2.60}$$

where, in the general Debye screening model, the original inverse screening length

is given by the expression,

$$\kappa_D = \frac{4\pi n_e}{k_B T}, \tag{2.61}$$

which is the inverse Debye length of the electrons only. This change means that the screening parameter, κ, is increased with increasing beam velocity, which decreases the effective range of the ion potentials within the target plasma. The screening is modified to be velocity dependant because it is found that at higher beam velocities the plasma is unable to form perfect screening clouds around the ion beam path. The stopping power can then be calculated from applying the velocity dependent screening length to the potential 'seen' by each beam particle. After this, it is still necessary to calculate the associated scattering wavefunction phase shifts, which, in turn, can be used to calculate the appropriate interaction cross-sections as explained in section 2.4.2 regarding the binary collision approximation to particle stopping power.

It is frequently desirable to be able to reduce the intensive computation that is necessary in order to numerically solve for the full T-Matrix stopping power. As a result, an analytical fit to the quantum mechanical T-matrix approach can be used to calculate the stopping power of a plasma [Gericke [2002]]. This fit to the combined T-Matrix model with dynamic screening is expressed as a polynomial in orders of the beam velocity. When compared with PIC simulations , the fit shows best agreement for stopping power calculations in cold, strongly-coupled plasma regimes [Gericke [2002]]. This model requires only the incident particle charge and the classical coupling parameter for the electrons in the target. The fit polynomial is written in the form

$$\frac{\partial}{\partial x} < E > \left[\frac{3(k_B T)^2}{e^2}\right] = \frac{A_1\bar{v} + A_2\bar{v}^2 + A_3\bar{v}^3 + A_4\bar{v}^4 \ln(c_1\bar{v}^2 + 1)}{1 + A_5\bar{v} + A_6\bar{v}^2 + A_7\bar{v}^3 + A_8\bar{v}^4 + A_9\bar{v}^5 + A_4 c_2 \bar{v}^6}$$

where the coefficients, A_{1-9}, are given in table 2.1. A breakdown of all of the remaining variables that are required to completely define the numerical T-matrix stopping power fit are detailed in full here,

$$\begin{aligned} x &= \ln(Z_b \Gamma_{ee}^{3/2}) \quad , \quad \bar{v} = \frac{v}{v_{th}} \\ c_1 &= 2m_e \frac{v_{th}^2}{\hbar\omega_{pe}} \quad , \quad c_2 = \frac{3a_B(k_B T)^3}{Z^2 e^2 \hbar^2 \omega_{pe}^2} \end{aligned} \tag{2.62}$$

Table 2.1: List of beam velocity coefficients for the polynomial fit to the combined stopping power model for T-Matrix binary collision stopping power with a dynamic screening description.

Coefficient	Expression	Condition
A_1	$A_1 = \exp(1.78x - 1.01)$	none
A_2	$A_2 = \exp(2.561x - 1.15)$	none
A_3	$A_3 = \exp(3.141x - 2.41)$	none
A_4	$A_4 = \exp(4.11x - 6.63)$	$x > 0.548$
	$A_4 = \exp(1.52x - 5.21)$	$0.548 > x > -2.649$
	$A_4 = \exp(2.09x - 3.70)$	$x < -2.649$
A_5	$A_5 = \exp(-1.05 + 0.195(x + 3.13)^2)$	$x > -3.13$
	$A_5 = \exp(-1.05)$	$0.548 > x < -3.13$
A_6	$A_6 = \exp(0.42x - 1.084)$	none
A_7	$A_7 = \exp(4.58x - 10.104)$	$x > 1.83$
	$A_7 = \exp(-1.73)$	$x < 1.83$
A_8	$A_8 = \exp(1.338x - 1.93)$	none
A_9	$A_9 = \exp(2.612x - 6.11)$	none

where Γ_{ee} and v_{th} are given by equations (1.6) and (1.9) respectively. In this thesis, the polynomial fit model is used for all of the T-Matrix calculations of electron contributions to stopping power in non-degenerate systems because of the massive reduction in computational effort that the fit offers.

2.5 First stopping power calculations for comparison

The basis of much of the work in this thesis is the application of stopping power calculations to numerical simulations of particle stopping. The first step in building these simulations is being able to calculate stopping powers. I have written routines which perform these stopping power calculations for the T-Matrix and the Thomas-Fermi model based on a set of inputs such as kinetic energy of an incident particle, and the temperature and density of the stopping medium. I have also written some iterative particle codes which evolve particles in time to simulate the effects of a stopping medium on incident particles of any species. These codes are written in a format of my choosing which is generic across the input and output parameters of the various stopping power models that I have programmed. As a result, I am able to interchangeably vary the stopping power model that is being used to evolve the particles which I am simulating. These particle evolution routines that I have written are most commonly used to return datasets showing, for example, the variation of stopping power with beam particle energy or the variation of stopping power with penetration depth along the flight path of a single particle. Figure 2.2 provides an example of the former dataset produced with a couple of the stopping power routines. In this case, the routine which is used to calculate the Lenard-Balescu stopping power was not implemented by me as it had been previously written by Jan Vorberger. Figure 2.2 shows the variation of stopping power with incident particle energy calculated with several stopping power models. The models used in this figure are the combined T-matrix model mentioned in this section, which has no treatment of degeneracy, and both the Thomas-Fermi model and the Lenard-Balescu RPA dielectric stopping power model, which both have a treatment of degeneracy. However, the RPA dielectric model is used less in simulation work because of the numerical of complexity of solving the double integrals which result from its kinetic approach compared to the relative numerical ease of solving for the Thomas-Fermi stopping power. The plasma regime shown in figure 2.2 is for a case of intermediate degeneracy in the electron system. The value of the degeneracy parameter in this figure is on the order of $n_e\Lambda_e^3 \sim 50$. Figure 2.2 shows examples of the effects of using a proper treatment of degeneracy upon stopping power calcu-

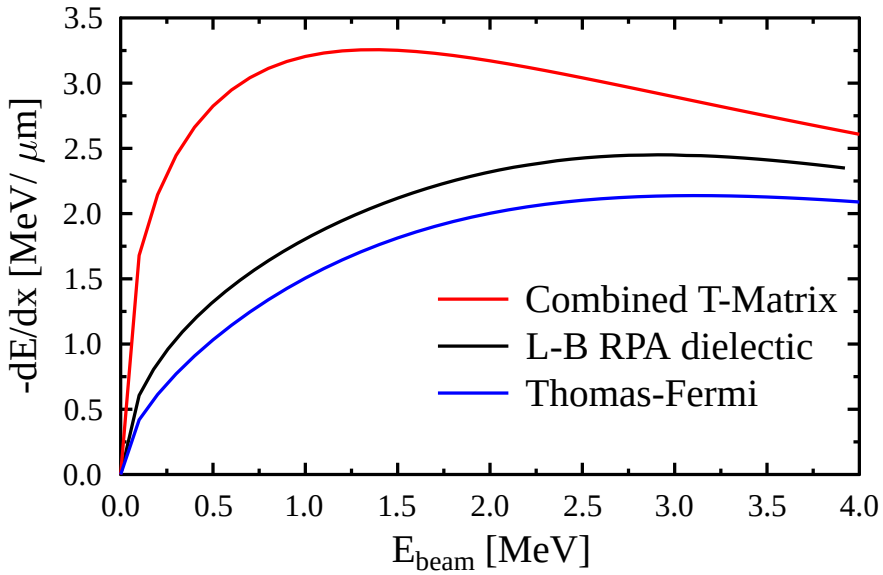

Figure 2.2: Comparison of the stopping power variation with incident particle energy for several models. Calculations are done using the combined T-matrix dynamic screening model, the Thomas-Fermi model and the Lenard Balescu RPA dielectric model. Stopping power calculations shown here are for alpha-particles stopping in a dense plasma with an electron density of $n_e = 10^{25}\,\mathrm{cm}^{-1}$ and an electron temperature of $T_e = 10^6\,\mathrm{K}$.

lations, as in the RPA dielectric method and the Thomas-Fermi model, compared with example calculations for the same stopping parameters without the degeneracy treatment in the combined T-Matrix data. There is an increase in the beam energy at which the stopping power is maximised due to the limiting degeneracy effects of the temperature of the target electrons. Also the peak value of the stopping power is significantly increased in the T-Matrix calculations compared with the degenerate models which will result in reduced energy deposition and longer particle ranges in a degenerate medium. Figure 2.2 is for intermediate degeneracy $n_e\Lambda_e^3 \sim 50$ and for cases of higher degeneracy, these effects become more pronounced.

This concludes the stopping power theory chapter. The stopping power models that have been described in this chapter can be used to accurately describe particle stopping in a wide range of plasma scenarios and in a limited range of solid-matter scenarios. These are the primary tools that are employed in the simulation work that is presented in the remainder of this thesis. Most commonly used will be the combined T-matrix model shown in equation (2.62), which is of particular

use in numerical simulations of particle stopping in non-degenerate, dense plasma systems, and the Thomas-Fermi model shown in equation (2.14) which is of particular use in numerical simulations of particle stopping in degenerate, dense plasma systems. There are still further theoretical topics which will need to be introduced later, although their limited domain of relevance to this work has meant that they will be introduced in the chapters to which they are applicable. The stopping power principles and models that have been covered in this chapter have relevance to each of the work chapters of this thesis.

Chapter 3

Collision cross-sections for stopping power

In the previous chapter it was seen that in many cases the dominant contribution to stopping power is from the energy loss contributions of electron scattering interactions. As a result, the cross-sections for these interactions become a fundamental quantity in many stopping power models and so calculating the cross-sections is an important step in the determination of stopping power. The scattering and momentum transport cross-sections can both be determined through a summation over all possible scattering interactions and their associated phase-shifts. The summations themselves are often computationally simple, but each scattering phase-shift requires multiple solutions to the Schrödinger equation to be calculated. This means that the full calculation can often be quite time consuming. In the case of lower energy states, the scattering wavefunctions will often need to be solved to very large radii. The repeated calculation of these solutions to the Schrödinger equation can take a significant amount of computing power.

This chapter will demonstrate the calculation of the interaction cross-sections, which are used to model ion stopping power. This chapter will also introduce a modification to these models for the case of a partially-ionised plasma, where the plasma ions are described using the Hartree-Fock equation. A comparison is then made between the Hartree-Fock results for the momentum transport cross-section of a Be^{2+} ion and the momentum transport cross-sections which result from the $Z = 2$ and $Z = 4$, unscreened Coulomb potentials.

3.1 Scattering cross-sections for collisions

In the majority of the stopping power scenarios that we model in this thesis, scattering interactions are the most commonly observed collisional interaction. As a result, the scattering cross-sections are an important quantity for describing stopping power. This can be from the theoretical derivation of the Bethe model or as directly inserted into the binary collision model that was described in section 2.4.2. In the binary collision model, collisions are handled by the direct calculation of solutions to the Schrödinger equation for free electrons scattering in the potential of an incident ion. Total cross-sections are then calculated by a summation over single-particle phase-shifts from these scattering wavefunctions [Newton [1982] p. 301]. When any kind of particle scatters through a potential, the result is a phase-shift in the particle wavefunction. This phase-shift can be measured by comparison with the wavefunction of an identical electron that has propagated freely and not undergone a scattering interaction. Solutions to the single-particle Schrödinger equation show that, in the absence of an external potential, a free wavefunction can be expressed in the form

$$u_l \simeq \sin\left(kr - \frac{1}{2}\pi l\right) \tag{3.1}$$

The process of scattering through the potential of some scattering body alters the form of the incident wave, such that the amplitude is modified and also that a shift, δ_l, is introduced into the wavefunction phase. At a large distance from the scattering potential, the local effect of the potential will have decayed to zero and the wavefunction of the scattered electron will take the following form,

$$\psi_l^{(+)} \simeq \exp\left(i\delta_l\right)\sin\left(kr - \frac{1}{2}\pi l + \delta_l\right). \tag{3.2}$$

This phase-shift can be used in calculations as a measure of the effect that the potential has had on the incident wave during the scattering interaction, e.g. for equal impact parameters and momenta, a stronger scattering potential will result in a larger phase-shift. In much of this work, models of stopping power are derived by considering elastic scattering of multiple particles in the centre of mass frame of the system. On transformation to the laboratory frame it is found that the previous direction change of the resultant momentum vector is now manifested as momentum transfer between particles. The phase-shifts can be calculated using analytical methods or they can be calculated numerically by propagating a free wavefunction and a scattering wavefunction from the same origin and directly measuring the phase-shift. Figure 3.1 shows an example of a free wavefunction plotted against the

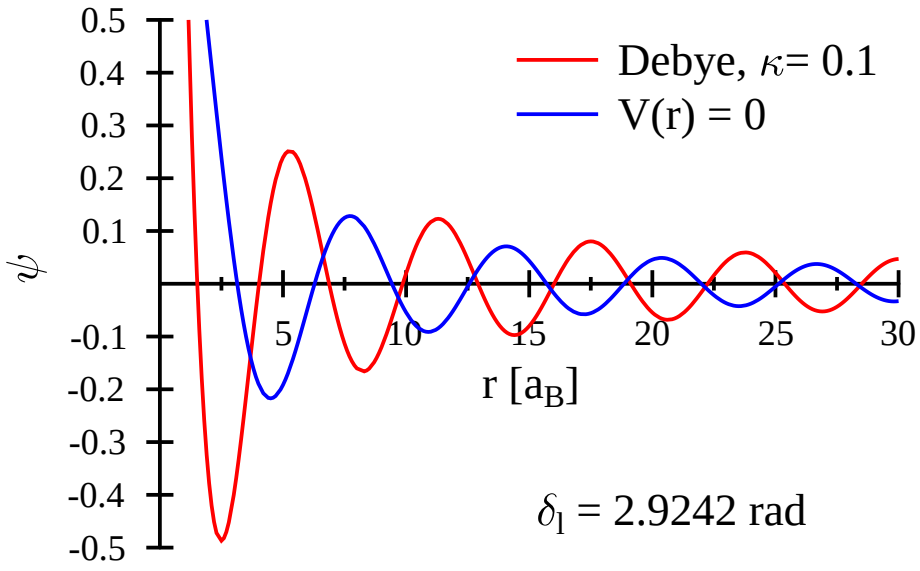

Figure 3.1: Example wavefunctions from numerical scattering phase-shift calculations for electrons. The blue curve, $V(r) = 0$, shows the free solution with a zero potential term in the Schrödinger equation. The red curve is the solution for an identical electron propagating through a Debye potential with an inverse screening length of $\kappa = 0.1\,\mathrm{a_B}^{-1}$. The observed phase shift is approximately 2.92 radians.

wavefunction of a scattered particle so that the phase-shift is visible. The analytical calculation is usually done in the following fashion [Newton [1982] p. 350]. The spherical solutions to the non-interacting single particle wavefunctions are described by Ricatti-Bessel and Ricatti-Neumann functions. It is possible to calculate the expected phase-shift analytically using combinations of these functions and the radial wavefunction solution, which can be written as [Kremp et al. [2004] p. 207]

$$\tan\delta_l(k) = \frac{\hat{j}_l'(kd)u_l(k,d) - \hat{j}_l'(kd)u_l'(k,d)}{\hat{n}_l'(kd)u_l(k,d) - \hat{n}_l'(kd)u_l'(k,d)} \tag{3.3}$$

where j denotes a Ricatti-Bessel function, n denotes a Ricatti-Neumann function, d is the range of the 2-body interaction potential, k is the wavenumber $p/\hbar$ and a prime denotes a derivative with respect to the radial coordinate, r, at a range of $r = d$. The total scattering cross-sections can then be obtained from partial wave expansions by summing over the phase-shifts for all angular momentum values using

the following equation

$$\sigma_{ab}^{\text{tot}}(p) = \frac{4\pi\hbar^2}{p^2}\sum_{l=0}^{\infty}(2l+1)\sin^{"}\delta_l(p). \tag{3.4}$$

This is valid for the case that a and b are not identical particles.

In the derivation of binary collision stopping power, the dependence upon these scattering cross-sections was included using the momentum transport cross-section, defined in equation (2.57). The calculation of the scattering cross-sections from phase-shifts can be extended to calculate the momentum transport cross-section directly from the scattering phase-shifts and is given by [Kremp et al. [2004] p. 207]

$$Q^T = \frac{4\pi\hbar^2}{p^2}\sum_{l=0}^{\infty}(l+1)\sin^2(\delta_l(p)-\delta_{l+1}(p)). \tag{3.5}$$

From this method, it is easy to see that the significant physics in the T-matrix binary collision stopping power model comes from the differences in this calculated momentum transport cross-section. This summations over scattering interactions simulated on a particle level is how the T-matrix model incorporates the binary collision physics.

3.1.1 Single Particle Schrödinger equation: Numerov solver

In order be able to calculate wavefunction phase-shifts it is first necessary to be able to solve the single-particle Schrödinger equation. The solutions to this equation are single-particle wavefunctions. The scattering phase-shift for a given particle in a known potential can be obtained by solving the Schrödinger equation of the system and comparing the solution to the solution for the case where the potential term is zero. Wave-functions which describe many-particle systems can be constructed as a superposition of interacting single-particle wavefunctions. However, no fully analytical solutions to the Schrödinger equation exist for any many-particle systems.

Binary collisions between particles of largely asymmetric mass (e.g. electron scattering contributions to ion stopping power) are most easily modelled as the particle of lower mass scattering through the static potential of the particle with higher mass. If the particle of higher mass is treated as a point particle emitting a static potential, this system can be described with a single-particle wavefunction for the scattering electron. As such, an analytical solution exists for the hydrogen atom and for hydrogen-like atomic systems, in which a nucleus of any mass is modelled as a single particle of sufficiently large mass that acts as a static potential. However,

because no fully analytical solutions exist for complex particle systems, numerical approaches are extremely widely utilised.

This work handles the single-particle case using numerically calculated single-particle wavefunctions. These solutions can be obtained using an effective iterative method for solving a particular class of second order differential equations known as the Numerov method [Numerov [1924]]. The algorithm is an iterative method for solving second order differential equations that have no dependence on the first order derivative, for cases where at least two closely-spaced initial points of the solution are known. As part of this work, I have written a Numerov solver which I apply in many cases to find solutions to the single-particle Schrödinger equation. This code is original work although the use of this algorithm for this application has been used many times before. As a result, it is important that I specify here that the work done to produce this solver and the associated wavefunctions has not been published by myself in any academic journal. The accuracy of the numerical solver written for this research was tested by calculating bound state wavefunctions whose energies were benchmarked against the analytically calculated and experimentally verified energy levels of the Hydrogen atom.

3.1.2 Radial Scrödinger equation

The Numerov algorithm, and the scattering state analysis we have applied, both work on a particular form of the Schrödinger equation. First it is useful to exploit the independence of angular and radial variables of particle wavefunctions and so isolate the radial component of the single particle Schrödinger equation. Beginning with the time independent Schrödinger equation for an electron in the Coulomb potential of a nucleus

$$-\frac{\hbar^2}{2\mu}\nabla^2\psi - \frac{Ze^2}{4\pi\epsilon_0 r}\psi = E\psi, \tag{3.6}$$

where $\mu = m_e m_p/(m_e + m_p)$ is the reduced mass of the electron-nucleus system in question. Then, assuming the wavefunction of the form $\psi(r,\theta,\phi) = R(r)\Theta(\theta)\Phi(\phi)$, an often seen separation of variables calculation allows the radial component of the Schrödinger equation to be isolated as the following, which is given in atomic units,

$$\frac{1}{r^2}\frac{\partial}{\partial r}\left(r^2\frac{\partial R}{\partial r}\right) + \left(E + \frac{2Z}{r} - \frac{l(l+1)}{r^2}\right)R = 0. \tag{3.7}$$

Equation (3.7) is the radial Schrödinger equation for the electron-nucleus system. Solving this equation is done in this work by introducing a new wavefunction $u(r) =$

$r \cdot R(r)$. This then removes the dependence of the radial Schrödinger equation on the first derivative of the wavefunction and allows the Numerov algorithm to be employed. It is easily shown now that this equation reduces to

$$\left(\frac{\partial^2}{\partial r^2} + E + \frac{2Z}{r} - \frac{l(l+1)}{r^2}\right) u(r) = 0. \tag{3.8}$$

This form of the radial Schrödinger equation, without the first order derivatives, can easily be solved numerically using the Numerov algorithm.

3.1.3 The Numerov method

The Numerov method is a numerical finite-difference method for solving second order differential equations with no dependence on first order derivatives Numerov [1924]. The Numerov method relates three points on the solution, separated by a step length 'h', and offers an algorithm for iteratively calculating the solution at a further step length. First the differential equation to be solved should be written in the form,

$$\frac{d^2}{dr^2}\psi(r) + \Omega(r) = 0. \tag{3.9}$$

The Numerov formula itself, giving the relationship between the solution points separated by fixed step lengths, can then expressed in the following form

$$\psi_{i+1} = 2\psi_i - \psi_{i-1} - \frac{h^2}{12}(\Omega_{i+1} + 10\Omega_i + \Omega_{i-1}), \tag{3.10}$$

where $\psi_{i+1} = \psi(r+h)$, $\psi_i = \psi(r)$ and $\psi_{i-1} = \psi(r-h)$. Equation (3.10) is the result of taking the Taylor expansion for ψ_{i+1} and ψ_{i-1}, summing the results, which cancels several terms in odd powers of the step-length, h, and then neglecting terms of sixth order and above under the assumption that the step length is small and so higher order terms become negligible. This truncation and the cancelling of odd order terms leaves an iterative series that is fourth order in the step-length and can be applied to solve second order differential equations that have no dependence on the first order derivative.

The algorithm leaves freedom to set $\Omega(r) = -f(r)u(r)$, where $f(r)$ is an arbitrarily chosen function and so for the intended uses here it is logical to choose

$$f(r) = \left(\frac{l(l+1)}{r^2} - E - \frac{2Z}{r}\right). \tag{3.11}$$

For the specific case of solving for a radial wavefunction in a Coulomb potential, the

Numerov algorithm is given by

$$\left[1-\frac{h^2}{12}f(r+h)\right]u(r+h)=\left[2+\frac{10h^2}{12}f(r)\right]u(r)-\left[1-\frac{h^2}{12}f(r-h)\right]u(r-h),. \tag{3.12}$$

Since the initial solution conditions that will be inserted into the solver are known at the $r=0$ boundary, this current form of the algorithm will cause complications. The wavefunction $u(r)=rR(r)$ will be equal to zero when the radial co-ordinate is zero and so information will be lost and the algorithm will not obtain the correct solution for $u(r+h)$. In order to avoid these complications the following substitution is made

$$z(r)=\left[1-\frac{h^2}{12}f(r)\right]u(r). \tag{3.13}$$

This substitution allows the Numerov algorithm to be further contracted and written in the following form

$$z(r+h)=2z(r)-z(r-h)+h^2f(r)u(r) \tag{3.14}$$

From this point, by inserting sufficient initial conditions, it is possible to solve the radial Schrödinger equation for a radial electron wavefunction over a desired radius. Now, the two initial points at the lower boundary necessary to employ the Numerov method must be decided. At low radii the function $u(r)$ takes the approximate form [Gericke [2000]],

$$u(r)\sim(2l+1)^{-1}r^{l+1} \tag{3.15}$$

which can determine the first value of the wavefunction for non-zero radius, $r=h$. The value of $u(h)$ can then be used to determine the corresponding value of $z(h)$. The $r=0$ value to be used in the Numerov algorithm, needs to be calculated from $z(r)$ in order for the Numerov solver to work correctly. Substituting the full expression for $f(r)$ into the equation for $z(r)$, which gives

$$z(r)=\left[1-\frac{h^2}{12}\left(\frac{l(l+1)}{r^2}-E-\frac{2Z}{r}\right)\right]\frac{r^{l+1}}{2l+1}, \tag{3.16}$$

it can be seen that there can be some terms which are not dependent on the radial co-ordinate. These remaining terms give the value of $z(0)$ for the boundary conditions of the algorithm. The values of $z(0)$ are simply tabulated here for different orders of the angular momentum quantum number, l.

$$z(0) = \begin{cases} \frac{1}{6}Zh^2 & : \quad l = 0 \\ -\frac{1}{18}h^2 & : \quad l = 1 \\ 0 & : \quad l > 1 \end{cases} \tag{3.17}$$

It is useful here to note that these expansions along with the Numerov algorithm are presented here as described in previous works (Gericke [2000]). This section provides a description of the theoretical basis of simulation codes that I have written and the mathematics is not a written account of new work done.

3.2 Scattering in partially-ionised plasmas

In many materials, the temperature and density conditions may be such that there is no molecular structure and much of the material is ionised but that some atomic bound states exist. In this regime, the material can still be described as a plasma but considerations should be made for the modified behaviour resulting from the partial-ionisation. In cooler, denser plasmas, it is often the case that the plasma is not fully ionised and that some electrons will remain in bound states. When considering stopping power in such a partially-ionised system, the contributions from scattering interactions with bound electron states will also need to be included. Partial-ionisation of a plasma can arise through suitable temperature conditions, where the average thermal kinetic energy is insufficient of overcome the atomic binding energies of available bound states. A contributing factor at higher densities is pressure ionisation. In this case, the density is sufficiently high that the particle self-energy can excite bound electron states and the bound electrons begin to ionise as the density increases.

In this work, Hartree-Fock theory is employed to model an ion which is screened by bound electrons. The potential solutions will be compared to those of bare Coulomb potentials. Hartree-Fock theory allows for the calculation of a self consistent set of electron wavefunctions and accounts for both the potential screening of the electron wavefunctions and also the electron-electron interaction terms. The mechanics of Hartree-Fock theory will be introduced later in this section.

3.2.1 Pressure Ionisation and the Mott transition

A possible scenario in which a plasma becomes partially-ionised is when a low temperature plasma is compressed to a sufficiently high density, that the particle self-

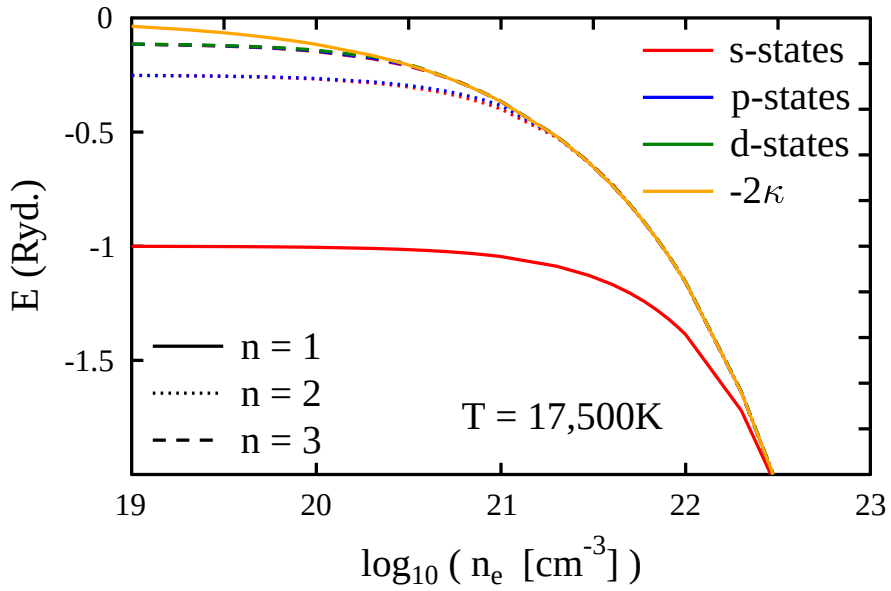

Figure 3.2: Calculations of decreasing binding energies for the hydrogen atom. These calculations detail the increase in self energy and the disappearance of the individual bound states for a temperature of $T = 17,500\,K$.

energies are great enough to overcome the electron binding energies of the higher bound states of the system. The data shown in figure 3.2 are the results of simulations that I have written and performed. The data show the lowering of electron binding energies in the hydrogen atom as the level of Debye screening is increased. My simulations calculate many bound electron wavefunctions in Debye screened potentials and plot the eigenvalues of the bound state energies against the electron density. The Debye screening is calculated from the electron density, assuming that the simulation is of a Hydrogen plasma. The code solves the Schrödinger equation many times, iterating the energy eigenvalue to find the bound state solutions. These solutions are located through analysis of the behaviour of the numerical solution at high radii. Numerical instabilities cause the value of the wavefunction to blow up to infinite magnitude, but the sign of this infinity is flipped as the energy eigenvalue crosses an equilibrium solution. Although the results presented here are only for hydrogen states, the solver has been used to apply the same methodology to heavier nuclei as well.

The calculations shown in figure 3.2 imply that as the density of a material increases, the particles' self-energy from constant Coulomb interaction increases. At some density this self-energy will reach a point such that it is greater than or equal

to the binding energies of the atomic electrons of the material. At this point, even at low temperatures, the self-energy contribution is sufficient to overcome the binding energy and ionise the material. The calculated energy values are then compared to the electron self energy in this system which is represented by the -2κ line, whilst the other lines represent the individual binding energies of the available bound states. It can be seen that as the density increases, the self-energy also begins to quickly increase and soon the ambient electron energy is sufficiently high that the bound states at higher excitations can no longer exist in the system. After a density increase of a few orders of magnitude the hydrogen is now a fully-ionised plasma, which was ionised simply by increasing its density. As previously implied, ionisation in this fashion is known as the 'Mott transition' or 'pressure ionisation'. This effect is observed at least in part in inertial fusion fuel pellets where the material densities are high enough to cause ionisation in some degree before the initial compression phase has even begun. If the local density is sufficiently high, any given material will begin to ionise and exhibit some plasma properties. This effect is often important when considering the behaviour of very dense, low temperature plasmas.

3.2.2 Levinson's theorem and limiting scattering behaviour

The disappearance of bound electron states can also be seen from the perspective of calculating positive energy scattering states as well as from negative energy bound states. In this case, Levinson's theorem can be employed to infer the number of available bound states in a system based on the low energy scattering behaviour.

The data shown in figure 3.3 are also from a simulation written by myself. This is another application of the Numerov solver to the single-particle Schrödinger equation in the field of a hydrogen nucleus. However, these calculations are for scattering electron states as opposed to bound electron states, as were shown previously. To produce figure 3.3 I wrote a simulation which solves for two electron states simultaneously, one of which is scattering in the potential of a screened hydrogen nucleus and one of which is a free state, i.e. the potential term is equal to zero. These solutions are calculated in parallel until such a radius that the effect of the nuclear potential is decided to have decayed to zero. This was determined in the code as the radius at which the wavelengths of the two solutions were equal to a tolerance of $\lambda_1/\lambda_2 = 1 \pm 10^{-6}$. From this point the solutions were propagated until the relative phase-shifts could be accurately recorded. The simulation calculated these phase-shifts for several cases, resolved over five orders of magnitude in linear momentum and angular momentum quantum number values of zero to fifty. The primary purpose of these phase-shifts was for calculating momentum transport

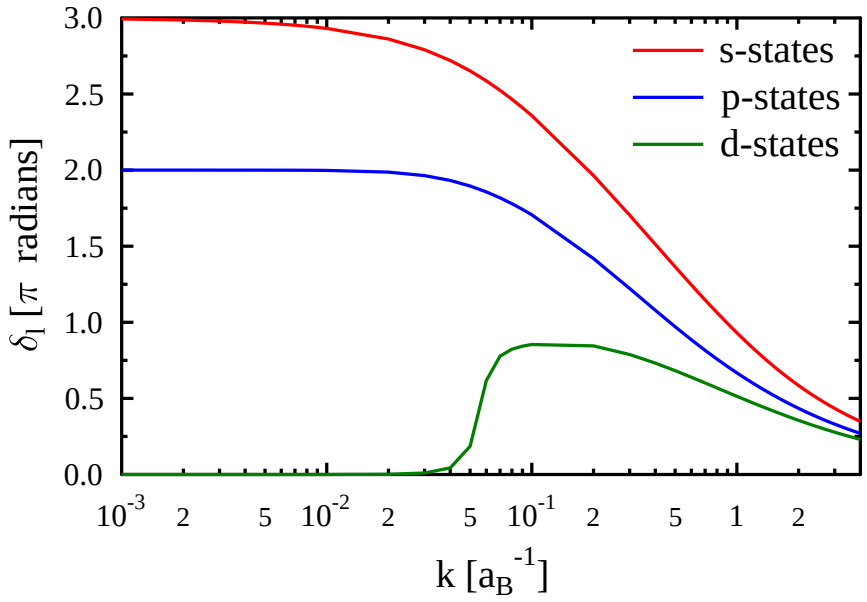

Figure 3.3: Phase shift calculations for electron-proton scattering over a wide range of impact momenta in a screened potential consistent with a dense hydrogen plasma. This graph shows that theoretical calculations are consistent with Levinson's theorem, regarding the scattering phase shift for zero impact momenta. This graph implies the existence of the 1s, 2s, 2p, 3s and 3p states but the finite energy splitting between angular momenta means the 3d state is above the self energy threshold and will not exist in this system.

cross-sections in order to obtain T-matrix stopping power values.

It has already been seen that an effective method for calculating the total scattering cross-section for a given scattering interaction is to calculate the scattering phase-shifts over a wide range of momenta. For the calculation of the momentum transport cross-section it was important to compare phase-shifts across different values of angular momenta, l. However, a distinct behaviour emerges for the case that a single l-value is considered and the phase-shifts are calculated only for differing values of linear, impact momentum. As the linear momentum of the incident particle gets progressively lower, it can be seen that the scattering phase-shifts tend to fixed values for the zero momentum phase-shift. Levinson's theorem is comprised of two equations which allow the value of this zero momentum phase-shift to be calculated from the number of possible existing bound states in the scattering system [Newton [1982] p.312].

The first equation of Levinson's theorem is

$$\delta_0(0) = m\pi, \tag{3.18}$$

where m is the number of s-wave bound states, except at the "transitional" strengths, where it is seen that

$$\delta_0(0) = \left(m + \frac{1}{2}\right)\pi. \tag{3.19}$$

This second equation states that with zero available bound states in the system and zero impact momenta, there will still be a finite, non-zero contribution to the observed scattering phase-shift. Figure 3.3 shows the limiting scattering behaviour for a dense hydrogen plasma. It shows three available s-states ($n = 1, 2, 3$), two available p-states ($n = 2, 3$) but due to the finite energy splitting of the 3s, 3p, and 3d levels we see that there are no available d states in this system.

3.3 Hartree-Fock theory

As previously stated, no fully analytical solutions to the Schrödinger equation exist for any systems that are more complex than a hydrogen atom. For more complex, many-particle systems, Hartree-Fock theory is often employed to calculate a self-consistent approximation to the real electron wavefunctions. In this approximation, the electron wavefunctions are obtained from solutions to the time independent Hartree-Fock equations which are given as follows

$$\begin{aligned} E_i u_i(r) &= \left[\frac{\partial^2}{\partial r^2} - \frac{l(l+1)}{r_i^2} + \frac{2Z}{r_i}\right] u_i(r) \\ &\quad - \sum_{j=0}^{n} \left(\frac{2\int \psi_j^* \psi_j d\mathbf{r}_j}{|\mathbf{r}_i - \mathbf{r}_j|}\right) u_i(r) + \sum_{j=0}^{n} \left(\frac{2\int \psi_j^* \psi_i d\mathbf{r}_j}{|\mathbf{r}_i - \mathbf{r}_j|}\right) u_j(r) \end{aligned} \tag{3.20}$$

where here, as in the Schrödinger equation of similar form, E_i is the energy eigenvalue of the ith wavefunction, $u_i(r)$ is the ith wavefunction multiplied by the radial coordinate to control the boundary conditions, l is the angular quantum number, Z is the charge in Coulombs of the local potential and the $\psi_{i,j}$ terms represent wavefunctions that are not multiplied by the radial coordinate. As we can see, the Hartree-Fock equations have an analogous form to the Schrödinger equation, only with two extra summation terms to account for the electron-electron interactions. The first of these is the Hartree term, which treats each electron as a charge distribution and integrates over space to calculate their influence on the local wavefunction by way of the Coulomb potential. In the Hartree term ψ_i represents the wavefunc-

tion that we are solving for, E_i is the eigenvalue of ψ_i and the summation over all ψ_j terms represents potential corrections that result from interactions of ψ_i with the other particles in the system. For the simple example of the Helium atom, ψ_i would be an electron wavefunction and ψ_j is the wavefunction of the second bound electron. In this case the Hartree term is simply a correction to the Coulomb potential of the nucleus which results from the electrostatic repulsion between the two bound electrons.

The second summation term is the exchange term which acts to enforce Pauli-blocking of states. This term is only non-zero when the i and j indices both refer to electrons in similar spin states. The most common application of Hartree-Fock theory is the numerical minimisation of the energy eigenvalues for the system in order to find an approximation to the ground state.

3.3.1 Calculated Hartree-Fock potential, Be^{2+}

I wrote a time independent Hartree-Fock code which solves the Hartree-Fock equations in three dimensional Cartesian space and is used to investigate simple multi-particle bound states. The code has been of use to this work though has limited applications. Some time working in Kiel has taught me that a more widely used method of numerically solving the Hartree-Fock equations is not to uniquely resolve the solution wavefunctions over grid points in three dimensional space but to construct the solution wavefunctions similar to the process of approximating a function using spherical harmonics. Unfortunately, time constraints have prevented me from implementing this code myself for use with this work and so the solutions presented have been resolved using my initial implementation. This Hartree-Fock code can be used to calculate a self-consistent configuration of electron wavefunctions for multiple particle bound states. The code is useful in this work because it allows the effective nuclear potential to be calculated beneath the radius of the electron orbits. This is important for calculations of scattering interactions and so will allow further analysis to produce stopping power calculations in partially-ionised systems.

Figure 3.4 shows some output from the time independent Hartree-Fock code when applied to the case of a beryllium 2+ ion. In this example, the two orbiting 1s electrons have orthogonal spins and so the evaluation of the Fock exchange term is trivial. The calculated potential clearly deviates from one limiting potential case to another. At low radii ($r < 0.1a_B$) the calculated potential behaves very much like the case of a $Z = 4$ Coulomb potential so that at these low radii the test charge effectively sees an unscreened Beryllium nucleus. At higher radii ($r > 0.5a_B$) the potential behaves like a $Z = 2$ Coulomb potential and so the test charge effectively

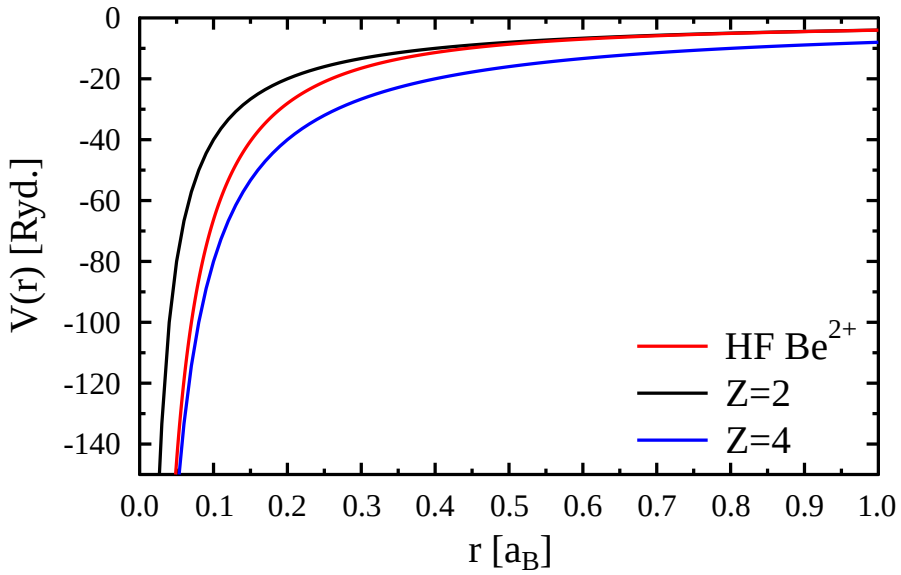

Figure 3.4: Effective radial potential surrounding a Be^{2+} ion. The potential is modified by screening of a self consistent electron configuration which is calculated from a time independent Hartree-Fock code. Also shown are the unscreened Coulomb potentials of a Z = 2 and a Z = 4 nuclear core.

sees a fully screened Be^{2+} ion. At the radii between these limiting cases there is some transitional behaviour as the potential varies smoothly from one limit to the other. Fortunately, from a numerical point of view, this behaviour can be described quite well by an analytical fit to the screened ion-ion potential in a partially-ionised plasma system [Vorberger et al. [2012]].

$$V_{ii}^{\text{eff}}(r) = \left[\frac{Z_1^2 e^2}{r} + \frac{\left(Z_c^2 - Z_1^2\right) e^2}{r} \exp\left(-br\right)\right] \exp\left(-\kappa r\right). \tag{3.21}$$

In equation (3.21), Z_1 is the charge state of the ion, Z_c is the ion's nuclear charge and the exponent b is a tunable fitting parameter. Figure 3.5 shows the accuracy of the fit detailed in equation (3.21) as it is applied to the previous example of the Be^{2+} ion. The observed agreement is very close over the important transitional region of the potential and the fit returns both limiting cases for large or small radii. This result significantly reduces the computational effort of calculating phase-shifts in a partially-ionised plasma.

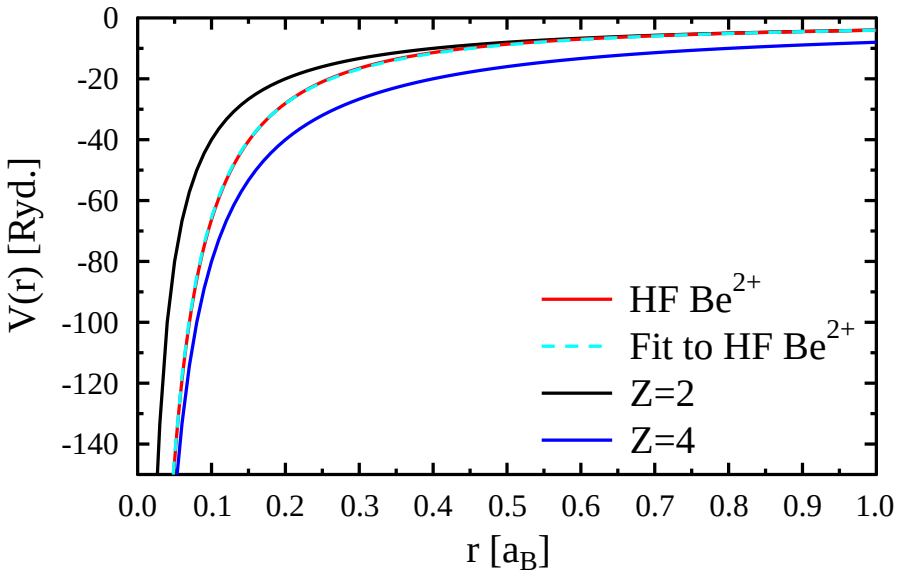

Figure 3.5: Effective radial potential surrounding a Be^{2+} ion. The potentials shown are the same as those shown in figure 3.4 with an analytical fit overlain to show the agreement. The fit is determined by an exponential radial decay between two limiting potentials and is detailed in [Vorberger et al. [2012]]. The exponent used in the exponential prefactor to the fit decay was 4.5.

3.4 Calculations of phase-shifts and Q^T

The methodology described in section 3.1 can then be applied, inserting the screened ionic fit potential into the Schrödinger equation in order to calculate scattering phase-shifts. Once a suitable range of these phase-shifts has been produced, they can be post-processed in order to obtain the corresponding momentum transport cross-sections using equation (3.5). These momentum transport cross-sections will highlight any peaks of important behaviour in the stopping power such as increased contributions due to the availability of unoccupied bound states.

For the analysis in this section I have calculated the scattering phase shifts for the interaction of electron scattering in screened ionic potentials. To do this I have used a code that I have written for calculating scattering phase-shifts, as described in section 3.2.2. This was applied to ionic potentials with spatially variant screening provided by the bound electrons. The screened potentials in the code are produced using an analytical fit detailed in [Vorberger et al. [2012]] to reduce numerical effort. However, as shown in figure 3.5, the analytical potentials were chosen to provide an

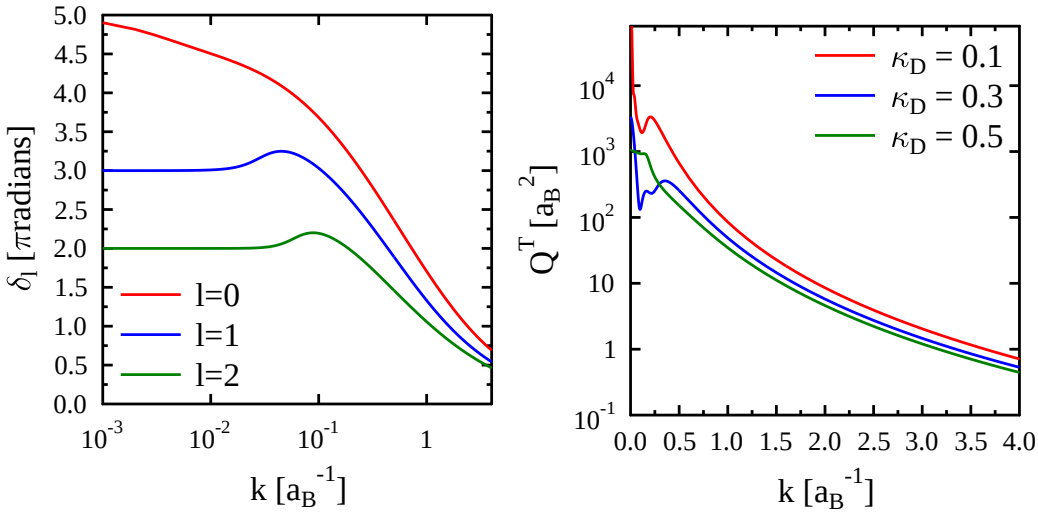

Figure 3.6: Scattering analysis for a $Z = 2$ Debye screened potential. Left: Scattering phase-shifts against impact momentum for a few values of angular quantum number, calculated with a screening of $\kappa = 0.1\, a_B^{-1}$. Right: Momentum transport cross-section for a small range of κ, calculated by summation over 50 values of angular momentum quantum number.

accurate match to the potentials that I have calculated for these ionic states using my time-independent Hartree-Fock solver.

3.4.1 Scattering calculations in Debye screened potentials

The phase-shifts and their corresponding momentum transport cross-sections were calculated for the limiting cases of the Hartree-Fock potential i.e. $Z = 2$ and $Z = 4$ Coulomb potentials. For the scattering calculations Debye screening was included on all these potentials to account for the long-range screening of the potential by neighbouring plasma ions.

Figure 3.6 shows the scattering phase-shifts and the associated momentum transport cross-section calculations for a $Z = 2$ Debye screened potential. The phase shifts for the $l = 0, 1, 2$ cases all tend to positive values for low impact momentum which shows that there are available bound states within the system. Noting that the y-axis has a logarithmic scale, the momentum transport cross-sections give quite different values for different screening lengths at low impact momenta. However, at higher k values the transport cross-section calculations begin to converge. At low values of impact momentum, effects from the existence of bound states appear as resonances in the momentum transport cross-section. These can cause significant

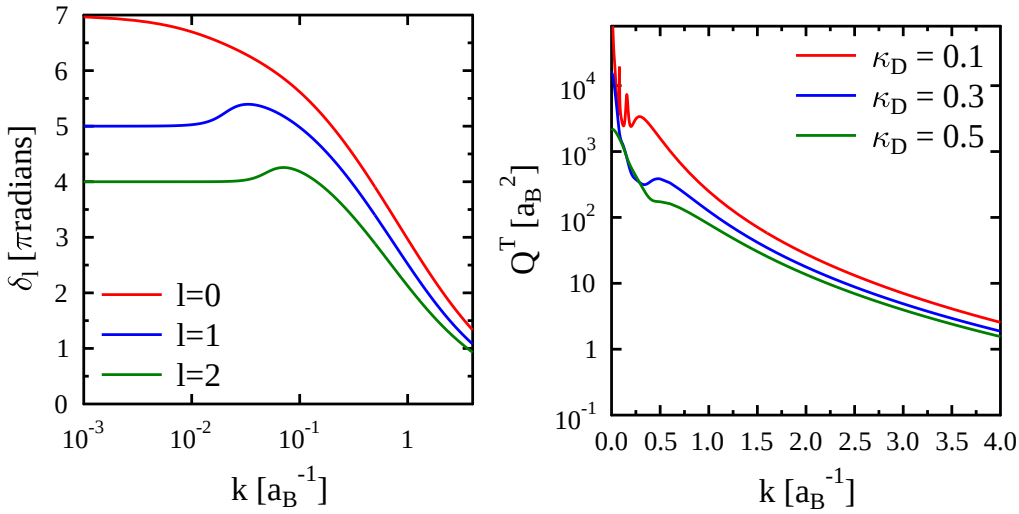

Figure 3.7: Scattering analysis for a $Z = 4$ Debye screened potential. Left: Scattering phase-shifts against impact momentum for a few values of angular quantum number, calculated with a screening of $\kappa = 0.1\, a_B^{-1}$. Right: Momentum transport cross-section for a small range of κ, calculated by summation over 50 values of angular momentum quantum number.

alterations to the corresponding calculations of the stopping power.

Figure 3.7 is the same combination of scattering phase-shift calculations and associated momentum transport cross-sections, only calculated for a $Z = 4$ Debye screened potential. The phase-shifts take a similar functional form to those of the lower charged Debye screened scattering calculations. However, these phase-shifts tend to higher values for low impact momenta because the higher nuclear charge offers deeper bound states for the incoming electrons. The transport cross-sections show quite similar behaviour with that of the previous Debye screened example, only with a consistently larger calculated value of Q^T. This would correspond accordingly to an increase in the calculated stopping power. Bound state resonances are also seen in the low momentum behaviour of the momentum transport cross-section which, in the case of lower screening, are evident as a series of tightly grouped peaks.

3.4.2 Hartree-Fock, Be^{2+}

Finally, the same analysis is performed for the fit to the Hartree-Fock potential of the Be^{2+} ion. In this case, the calculated scattering phase-shifts are very similar to those calculated for the $Z = 2$ Debye screened case. This is because there is only a very limited range, close to the nucleus, over which the Hartree-Fock potential is

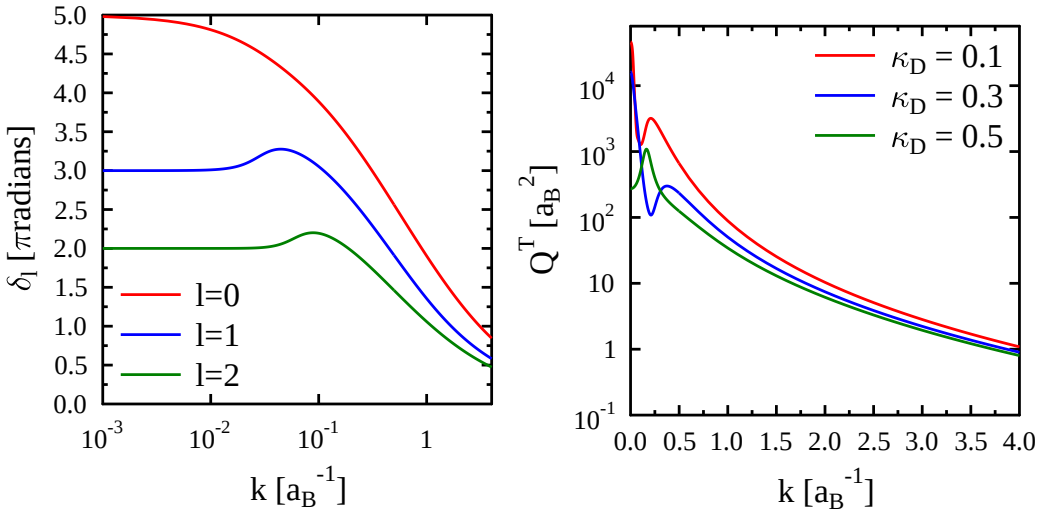

Figure 3.8: Scattering analysis for the analytical fit to the calculated Hartree-Fock potential of the Be^{2+} ion. Left: Scattering phase-shifts against impact momentum for a few values of angular quantum number, calculated with a screening of $\kappa = 0.1\, a_B^{-1}$. Right: Momentum transport cross-section for a small range of κ, calculated by summation over 50 values of angular momentum quantum number

not acting as the limiting case of the $Z = 2$ potential. The low momenta phase-shift limits are the same in both cases but, at higher momenta, direct comparisons with the $Z = 2$ case show some noticeable deviations in the calculated phase-shift values between the two cases. The momentum transport cross-section again shows a similar behaviour of becoming divergent for low values of momentum and convergent for higher values of impact momentum. However, the appearance of the resonances is different from both of the preceding cases, producing fewer, broader deviations of the momentum transport cross-section.

Hopefully, these effects should translate to a measurable deviation when modelling ions in partially-ionised plasmas. The differences should highlight the significance level of modelling ions with populated bound states as particles with distributed charge screening, rather than modelling these ions simply as unscreened charge states of lower magnitude.

3.5 Energy loss contributions from ionisation

In any system which is not fully ionised it is likely that incident ions can cause ionisation interactions. In addition to the scattering interactions that have previously

been considered, these ionisation interactions will provide additional contributions to the energy loss of incident ions travelling through the partially-ionised medium. In order to investigate these contributions the first logical step seems to be to calculate how frequently these ionisation interactions are likely to occur. From this, estimates can be made for the size of any additional contributions to the stopping power. These initial estimates will act as an indication of how significant the effects of these ionisation interactions are likely to be on the final stopping power. In this approach, we consider the energy transferred between two ions which pass at some distance of closest approach and compare this energy transfer to the binding energy of any electrons in the system that are available for ionisation. For this approximation, we will model the incident ion as a point particle and we will use time-dependent Hartree-Fock theory to model the ions of the stopping material as extended bodies with variable bound electron configurations. Figure 3.9 offers a simple representation of this scenario.

To estimate the magnitude of the contributions from these ionisation interactions we will calculate the distance of closest approach between an incident ion and a bound state electron at which there can be sufficient energy transfer for the bound state electron to ionise. From this point, we can then estimate a volume around each bound ion that when incident ions enter, there is a probability of an ionisation interaction. Comparing the volume of these spheres with the volume of the stopping medium will offer a measure of the likelihood of ionisation interactions from incident ions.

As a first approximation, we consider a distance of closest approach that is sufficiently large with respect to the Hartree-Fock electron orbits such that we can consider the potential of the Hartree-Fock ion to be seen as a Coulomb potential by the incident ion. We then assume that the limit of the energy transfer to the bound electron is the work done against the Coulomb potential by the incident ion. In this approach, the maximum work done against the Coulomb potential will be given as

$$w = \frac{Z_a Z_b e^2}{4\pi\epsilon_0 X} \tag{3.22}$$

where Z_a is the charge of the incident ion, Z_b is the resultant charge of the partially-ionised ion of the stopping medium that we aim to model with Hartree-Fock theory and X is the distance of closest approach of the ion path.

We can easily find the limiting closest approach for ionisation by using the limiting case that the work done against the Coulomb potential is exactly equal to

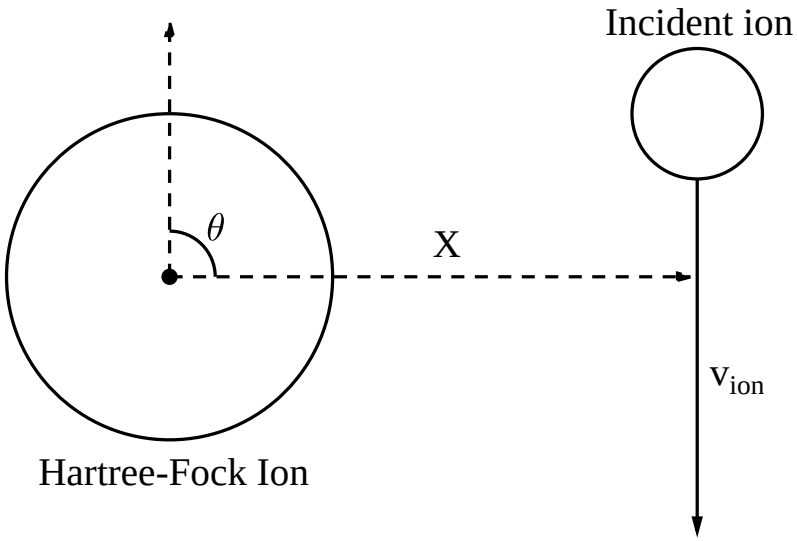

Figure 3.9: Diagram showing the geometry of the ion interaction which creates the need for a time-dependent Hartree-Fock approach to the modelling. An incident ion passes a Hartree-Fock ion at rest with some distance of closest approach, X.

the binding energy of the bound electron.

$$\frac{Z_a Z_b e^2}{4\pi\epsilon_0 X} = E_{\text{binding}} \quad \rightarrow \quad X = \frac{Z_a Z_b e^2}{4\pi\epsilon_0 E_{\text{binding}}} \tag{3.23}$$

Now it is possible to define a 'volume of ionisation' around the static ion. If the path of an ion with sufficient kinetic energy enters this volume then ionisation interactions would be possible. This volume would be defined as a sphere of radius, X, whose volume is given as

$$V_{\text{ionisation}} = \frac{4}{3}\pi \left(\frac{Z_a Z_b e^2}{4\pi\epsilon_0 E_{\text{binding}}} \right)^3 \tag{3.24}$$

Assuming nothing about the structure of the stopping medium and taking this volume as a ratio of the available volume per particle in the medium, we obtain a rough estimate of the probability of an ionisation interaction occurring.

$$P_{\text{ionisation}} = \frac{V_{\text{ionisation}}}{V/N} = \frac{4\pi n_{i,bound}}{3} \left(\frac{Z_a Z_b e^2}{4\pi\epsilon_0 E_{\text{binding}}} \right)^3 \tag{3.25}$$

where V is the total volume of the stopping medium and N is the number of ions with bound electrons in the stopping medium, hence N/V is the number density of

ions with bound electrons, $n_{i,bound}$. To quantify this estimate briefly, we will take the case of simulated partially-ionised Beryllium profiles, calculated by Jan Vorberger which have been used in chapter 4 of this work. Given a partially-ionised Beryllium medium with an electron density on the order of $10^{23}\,\mathrm{cm}^{-3}$, for an incident alpha-particle, this ratio works out to be approximately 0.4%. This means that the spheres of maximum closest approach for ionisation occupy 0.4% of the total volume of the stopping medium, which is a large enough fraction to warrant further investigation.

3.5.1 Ionisation Modelling

In order to improve the initial energy transfer assumption of the Hartree-Fock ion being treated as a static point-like Coulomb potential, it would be better to have the electron orbit modelled as an extended body and better again to allow the electron wavefunction to respond in real-time to the potential of the incident ion. To do this we aimed to employ some time-dependent Hartree-Fock modelling.

This work was planned to use 'Kiel MCTDHF' [Hochstuhl and Bonitz [2011]], which is a multi-configurational, time dependent Hartree-Fock (MCTDHF) code written by David Hochstuhl whilst working in the group of Professor M. Bonitz at Christian-Albrechts-Universität zu Kiel. MCTDHF is often done by approximating the solution wavefunction for a given system using a summation over single-particle, unscreened spin-orbital wavefunction solutions. In this way it works much like approximating any function with an expansion over known spherical harmonics. Applying this method using a truncated infinite series of spin-orbital wavefunctions (configuration interaction method) can be very computationally intensive. To mitigate this, Kiel MCTDHF uses a reduced set of spin orbitals which are selected from the infinite series for each specific solution. In some regimes, Kiel MCTDHF converges significantly faster than applying the full configuration interaction method, however, in more complex systems, the work of calculating which reduced set of spin-orbitals to use can become as computationally intensive as calculating the coefficients for every spin-orbital in the series. Using computational Hartree-Fock imposes some limitations on the number of electrons that can be simulated and so this method of ionisation modelling is best suited to light elements or plasmas with only weak partial ionisation.

3.5.2 Convergence testing for spherical expansion of incident ion potential

The nature of the geometry in which the Kiel MCTDHF solves the time-dependent Hartree-Fock equations requires that we have a spherical harmonic expansion to describe the potential of our incident ion as seen from the Hartree-Fock ion in figure 3.9. The expression for the time-evolution of the position of the incident ion, represented in spherical coordinates with the Hartree-Fock ion at the origin of the system is given by the following.

Initially, the Cartesian position vector of the incident ion is given by

$$\mathbf{x}_\alpha = (X_0,\ 0,\ Z_\alpha(t)) = (X_0,\ 0,\ Z_0 + vt) \tag{3.26}$$

where the initial z-location of the incident ion, Z_0, is large and negative and the distance of closest approach, X_0, is a finite positive value.

To translate the expression for the variation of the z position in time into a spherical representation, we define the line $\theta = 0$ as lying along the Cartesian z-axis so we can write

$$Z_0 = -X_0 \tan\left(\theta_0 - \frac{\pi}{2}\right). \tag{3.27}$$

Inverting this expression for θ and imposing the linear variation of $Z_\alpha(t) = Z_0 + vt$ from equation (3.26) we can then say at a later time, t,

$$\theta_\alpha(t) = \frac{\pi}{2} + \arctan\left(\frac{vt}{X_0} - \tan\left(\theta_0 - \frac{\pi}{2}\right)\right) \tag{3.28}$$

which is such that from equations (3.26-3.28) we get the following description of the time-evolution of the z-coordinate of the incident ion as

$$Z_\alpha(t) = -X_0 \tan\left(\theta_\alpha(t) - \frac{\pi}{2}\right) = -X_0 \tan\left(\theta_0 - \frac{\pi}{2}\right) + vt \tag{3.29}$$

The radial component of the particle position can then be calculated as

$$r_\alpha(t) = \sqrt{X_0^2 + Z_\alpha^2(t)} = X_0\left[1 + \tan^2\left(\theta_\alpha(t) - \frac{\pi}{2}\right)\right]^{1/2} \tag{3.30}$$

and so from equations (3.28) and (3.30) we obtain the full full position vector of the incident particle as

$$\mathbf{r}_\alpha(t) = \left[X_0\left[1 + \tan^2\left(\theta_\alpha(t) - \frac{\pi}{2}\right)\right]^{1/2}, \frac{\pi}{2} + \arctan\left[\frac{vt}{X_0} - \tan\left(\theta_0 - \frac{\pi}{2}\right)\right], \phi_\alpha\right]. \tag{3.31}$$

For the generalised vector co-ordinate, $\mathbf{r}$, we are looking for the value of the Coulomb potential from the incident ion which takes the form

$$V(r,\theta,\phi,t) = \frac{-Q_\alpha Q_{\mathrm{HF}}}{4\pi\epsilon_0\ |\mathbf{r}-\mathbf{r}_\alpha(t)|} \tag{3.32}$$

where Q_α is the charge of the incident ion and Q_{HF} is the charge of the Hartree-Fock ion. In our spherical coordinate system, the equations for Cartesian co-ordinates are,

$$x = r\sin\theta\cos\phi \tag{3.33}$$

$$y = r\sin\theta\sin\phi \tag{3.34}$$

$$z = r\cos\theta \tag{3.35}$$

and so the distance $|\mathbf{r}-\mathbf{r}_\alpha(t)|$ is given by

$$\begin{aligned} |\mathbf{r}-\mathbf{r}_\alpha(t)| = & \Big\{ \left[r\sin\theta\cos\phi - r_\alpha(t)\sin\left(\theta_\alpha(t)\right)\cos\left(\phi_\alpha(t)\right)\right]^2 \\ & + \left[r\sin\theta\sin\phi - r_\alpha(t)\sin\left(\theta_\alpha(t)\right)\sin\left(\phi_\alpha(t)\right)\right]^2 \\ & + \left[r\cos\theta - r_\alpha(t)\cos\left(\theta_\alpha(t)\right)\right]^2 \Big\}^{1/2} \end{aligned} \tag{3.36}$$

The potential can then be expressed as a series of spherical harmonics with time dependent coefficients

$$V(r,\theta,\phi,t) = \sum_{lm} C_{lm}(t)Y_{lm}. \tag{3.37}$$

The coefficients of the spherical harmonic expansion can be obtained from the following integral over the potential and the spherical harmonic functions

$$C_{lm}(t) = \int_0^{2\pi}\int_0^{\pi} \sin(\theta)V(r,\theta,\phi,t)Y_{lm}(\theta,\phi)d\theta d\phi \tag{3.38}$$

where the spherical harmonics are generally written as

$$Y_{lm}(\theta,\phi) = \sqrt{(2l+1)\frac{(l-m)!}{(l+m)!}}P_{lm}(\cos(\theta))e^{im\phi} \tag{3.39}$$

and the associated Legendre polynomials, P_{lm}, are given as

$$P_{lm} = \frac{(-1)^m}{2^l l!}(1-\cos^2(\theta))^{\frac{m}{2}}\frac{d^{l+m}}{d\cos\theta^{l+m}}(\cos^2\theta-1)^l \tag{3.40}$$

Combining these expressions into one gives us an expression for the time-dependent

coefficients of our spherical harmonic expansion. This describes the potential of our incident ion, as seen by the static Hartree-Fock ion that we wish to model with Kiel MCTDHF. By this process, equation (3.38) now becomes

$$\begin{aligned} C_{lm}(t) &= \frac{(-1)^m}{2^l l!}\sqrt{(2l+1)\frac{(l-m)!}{(l+m)!}}\int_0^{2\pi}\int_0^{\pi}\sin\theta\cdot\left(1-\cos\theta^2\right)^{\left(\frac{m}{2}\right)} \\ &\quad\times\frac{-Q_\alpha Q_{\mathrm{HF}}}{4\pi\epsilon_0\ |\mathbf{r}-\mathbf{r}_\alpha|}\left[\frac{d^{l+m}}{d\cos\theta^{l+m}}\left(\cos\theta^2-1\right)^l\right]\exp(im\phi)d\theta d\phi. \quad (3.41) \end{aligned}$$

In order to calculate a single spherical harmonic expansion, at a single point in time, this integral needs to be solved for $2l+1$ permutations of m and l to get the series of coefficients. As the coefficients are functions of r, each case of m and l values needs to be resolved in sufficient resolution in r to obtain the functional form of the coefficient. This is a computationally intensive task and does hinder the potential effectiveness of this modelling approach. Figure 3.10 shows an example of a dimensionless calculation of the potential that results from the spherical harmonic expansion we have described here. Having derived this expansion, I wanted to assess the general functional form of the potential before attempting to integrate the time-dependent coefficient expansion into the Kiel MCTDHF code. I learned Mathematica and wrote a Mathematica code to solve my equations over a relatively low radial resolution such that I could simply plot the potential, seen in figure 3.10. The potential has the general form that I expected and linear analysis of the data points shows that the potential has a moderately good agreement to a $1/r$ potential centred around the Cartesian coordinates $(1, 0, 0)$.

Unfortunately, this work did not reach a conclusion. Nothing further was done with this expansion and so the time-dependent perturbation effects of incident ions on bound electron wavefunctions are still yet to be calculated in any meaningful quantitative capacity.

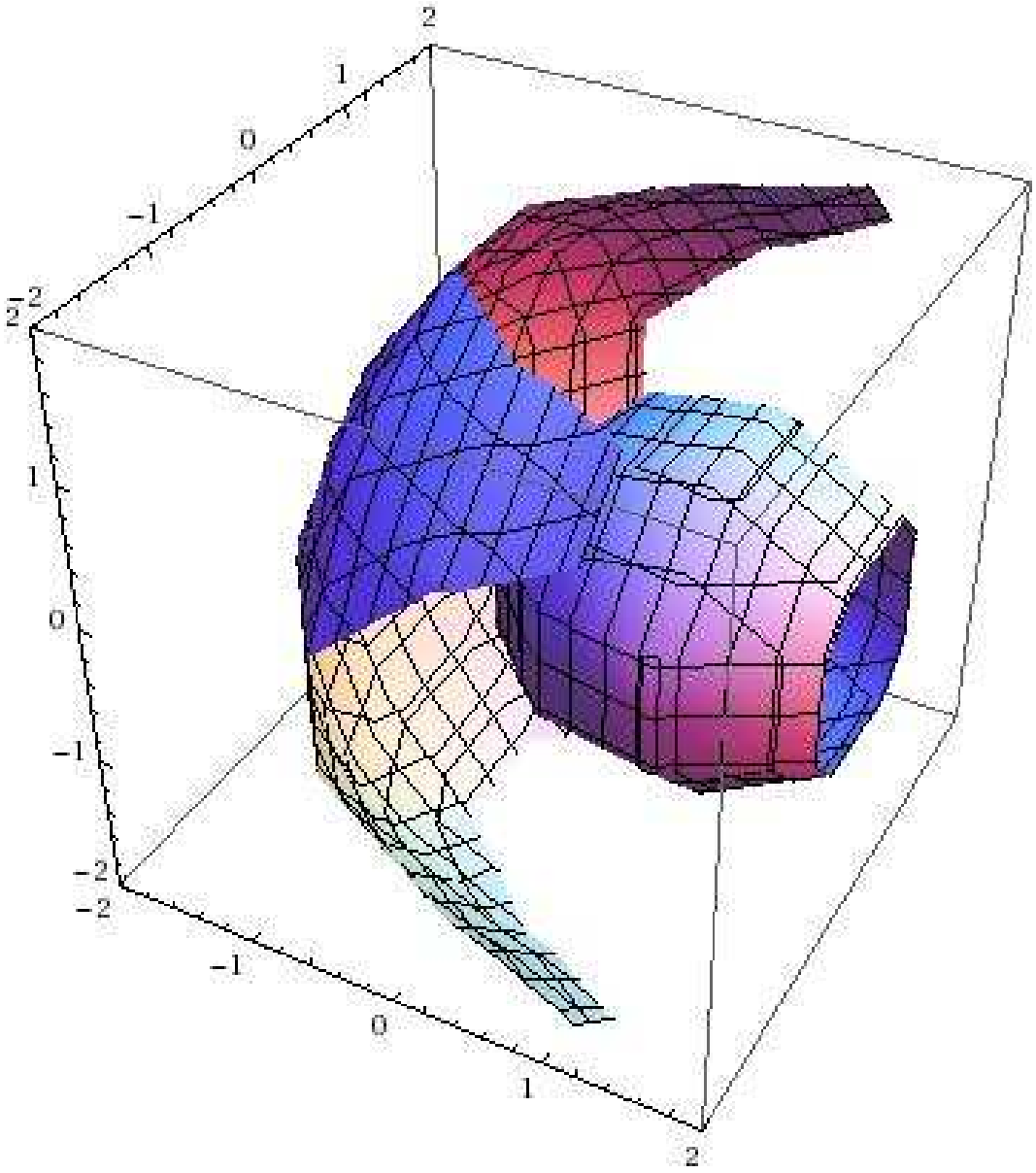

Figure 3.10: Dimensionless calculation of potential to assess the functional form of the spherical harmonic expansion described. Isosurfaces of potential plotted for the case that the incident ion is directly at the point of closest approach with a distance of closest approach of 1.

Chapter 4

Effects of microscopic density variations on stopping power

When modelling any physical scenario, a sensible first step is to make some initial assumptions about the system and then to test the regimes of validity of your assumptions. When modelling particle stopping, the target medium is commonly assumed to be an isotropic body of uniform electron density. Unfortunately however, this assumption is flawed at any level of detail where the microscopic variations of the target are of interest. The electron density profile of any atomic or ionised matter will always maintain significant internal structure. This is a result of the strong Coulomb interactions between the ions and electrons of the target medium. Electron density profiles of atomic or ionised matter can exhibit large variations in the magnitude of the local electron density and these variations occur on a microscopic spatial scale. In this chapter we investigate the effect that these microscopic density fluctuations can have on calculations of particle energy deposition. The simulation results for these energy deposition scenarios are then compared with similar calculations that employ a uniform mean density approximation.

In order to describe the variable electron density profiles, density functional theory - molecular dynamics (DFT-MD) simulations are performed. These provide us with a three-dimensional picture of the variable electron density in our target medium. From this, density profiles for a one-dimensional particle trajectory can be extracted, which are used for single-particle energy deposition calculations. Specifically, this chapter investigates particle stopping in DFT-MD profiles of dense, fully-ionised hydrogen and solid density, partially-ionised beryllium. These investigations were performed with the aim of investigating energy transfer dynamics in the fuel and ablator of an inertial fusion capsule.

4.1 Electron density variations in matter

All electron systems in matter exhibit a notable degree of structure at a particle level. This work aims to test the simple assumption that a target medium can be modelled as a structure of uniform electron density for the purposes of electron stopping power calculations. This section will briefly discuss the origins of the internal structure of natural target media in order to justify the need for an awareness of these variations and their regimes of significance.

We begin with the case of a solid, atomic or molecular material. It is known that the electrons exist in bound, atomic states, localised at the locations of the nuclei. As a result, the majority of the electrons of such a medium will not exist as a uniform electron medium. Any description which assumes that the electrons are distributed uniformly will not provide an accurate description of the local electron density of the medium. Electron structure is still found when considering the next material example of a fully-ionised plasma. In such a fully-ionised plasma, the demand for rigorous atomic structure is no longer a necessity but structure in the electron density profile still remains. The medium electrons no longer exist primarily in bound states but at higher energy free states. Now however, their behaviour can be described using the Debye model of a quasi-neutral plasma. The Debye model states that electrons form screening clouds around the plasma ions in order to maintain the quasi-neutrality of the bulk plasma on a macroscopic scale. As a result, even in the case of a fully-ionised quasi-neutral plasma, one should still observe a notable level of structure in the electron density profile and not a distribution which is homogeneous and flat. Without much effort, one should be convinced of the assertion that, on a microscopic scale, there is very little basis to the assumption that the electron distribution in any material is uniform and single-valued. However, this mean density approximation is widely used for stopping power calculations to good effect and so it is of interest to know in which regimes, if any, that the effects of these microscopic density variations become prominent.

The importance of refining the mean density assumption lies in the derivation of quantum kinetic models of stopping power, where interactions are being considered on a particle level. In many regimes, models derived at this precision will provide a more accurate representation of the stopping behaviour than classical collisional models. Also, the quantum models have the potential to provide greater energy deposition resolution if the density profile of the stopping medium is also known to a greater precision. A key aspect which could cause deviation from an averaged treatment is the simple observation that stopping power does not scale lin-

early with density of the stopping medium. As a result, the greater the magnitude of the density deviations from a measured mean, the less accurately a mean density approximation will represent the observed stopping behaviour.

Simulations have been performed which calculate particle energy deposition for the case of a target medium modelled as a uniform body with a single fixed value electron density. Further simulations have also been performed for identical particle stopping scenarios where the target electron density profile is modelled through DFT-MD calculations. The simulation results of the two density treatments are compared and the variations in the calculated stopping powers, energy deposition profiles and particle ranges are quantified.

4.2 Introducing Density Functional Theory (DFT)

It has been stated previously that single-particle systems can be described mathematically by wavefunctions that are solutions to the single-particle Schrödinger equation. Although, when considering more complex systems of many particles, the system can still be described by a composite wavefunction. In this scenario, the wavefunction will be a solution to the n-particle Schrödinger equation. This equation can be written as

$$\left[\sum_i \left(-\frac{\hbar^2}{2m_e}\nabla^2_{\mathbf{r}_i} + V_{\text{ext}}(\mathbf{r}_i) + V_{e-e}(\mathbf{r}_i)\right)\right]\Psi(\mathbf{r}) = E\Psi(\mathbf{r}), \tag{4.1}$$

where $V_{\text{ext}}(\mathbf{r}_i)$ is the external Coulomb potential, $V_{e-e}(\mathbf{r}_i)$ is an electron interaction potential, E is the energy eigenvalue of the system and $\Psi(\mathbf{r})$ is the many-particle wavefunction. Solving for the wavefunctions of complex many-particle systems can be complicated and so certain assumptions may simplify this process. DFT simplifies the system by solving for a set of single-particle wavefunctions in an effective potential. This effective potential is tuned to represent the local effects of the n single-particle potentials of the surrounding medium. In systems where an assumption of periodicity at some scale can be made, the full DFT calculation is often greatly simplified. Naturally, from the full description of a periodic system element, a description of a medium of arbitrary size can be produced.

DFT can provide an accurate representation of the electronic structure of a dense plasma and so is useful in modelling the systems that we are attempting to describe. DFT is built on the Hohenberg-Kohn theorem which states that the ground state electron density completely describes a physical system [Hohenberg and Kohn [1964]]. Once the ground state electron density profile is known, every

physical property of the system can be calculated from functionals of this ground state density, where the density can be determined from the wavefunction by the relation,

$$\rho = |\psi|^2 = \psi\psi^*. \tag{4.2}$$

The density is therefore independent of the phase of the wavefunction and so no effects of phase dependence are observed in the physical quantities of the system. The Kohn-Sham ansatz can be employed to connect the original many-particle system to a secondary, non-interacting system under the premise that the original ground state density must be preserved [Kohn and Sham [1965]]. Using atomic units, the Hamiltonian of the non-interacting system can be written as [Martin [2004]]

$$H^{\sigma}_{KS} = \frac{1}{2}\nabla^2 + V^{\sigma}_{KS}(\mathbf{r}), \tag{4.3}$$

where V^{σ}_{KS} is the Kohn-Sham effective potential seen by the electrons. This potential will reproduce the original ground state density and consists of several contributions, which are given as

$$V^{\sigma}_{KS}(\mathbf{r}) = V_{\text{ext}}(\mathbf{r}) + V_{\text{Hartree}}[n] + V^{\sigma}_{\text{xc}}[n]. \tag{4.4}$$

$V_{\text{ext}}(\mathbf{r})$ is the real potential from ions in the system and external fields, $V_{\text{Hartree}}[n]$ is the Hartree potential, determined by the local density and $V^{\sigma}_{\text{xc}}[n]$ is the exchange correlation potential which is also determined by the local density. Determining the exchange correlation term is often difficult and in many correlated systems this term will need to be approximated. These approximations introduce some uncertainty into this method of calculation [Martin [2004]]. Much work has been done on refining the values of this exchange correlation term. Two effective methods are the local density approximation (LDA) and the generalised gradient approximation (GGA). LDA assumes that for any given particle, the exchange correlation energy is the same as the energy of a homogeneous electron gas with equal density to the system being investigated. This method can be refined, incorporating the effects of spin, which is known as the local spin density approximation (LSDA). GGA makes a local approximation to the exchange correlation energy, taking the gradient of the density into account. For many systems this consideration results in an improvement in the accuracy of the final calculated ground state density. To investigate a system using DFT, the Kohn-Sham equations are solved in a self-consistent manner. An initial ground state density can be estimated and then, also inserting an estimation of the total potential, the generalised Schrödinger equation must be solved for the electron

wavefunctions.

$$\left[-\frac{1}{2}\nabla^2 + V_{KS}^{\sigma}(\mathbf{r})\right]\psi_i^{\sigma}(\mathbf{r}) = \varepsilon_i^{\sigma}\psi_i^{\sigma}(\mathbf{r}), \tag{4.5}$$

where ε_i^{σ} and $\psi_i^{\sigma}(\mathbf{r})$ are the particle energy eigenvalues and wavefunctions respectively. These updated wavefunction solutions give a new value for the electron density. From this density, a new potential can be calculated and again the Schrödinger equation can be solved, resulting in a new electron density. Repeating this process until convergence is reached, the system will quickly relax into its true ground state density.

Originally DFT assumed a system was in its absolute ground state, with zero temperature. Later work included effects of temperature such as the work of Mermin [Mermin [1965]]. This temperature modelling is important for the application of DFT in the work presented in this thesis. Since their conception, DFT calculations have also been successfully combined with molecular dynamics (MD) simulations, which was achieved in 1985 by Car and Parrinello [Car and Parrinello [1985]]. Originally, the work of Car and Parinello assumed that the global electron structure would be constant for many MD steps and so to lower the computational intensity, their approach performed many MD steps for each complex DFT calculation. However, this method was reversed in the Born-Oppenheimer approach in which it is assumed that the lightweight electrons respond instantly to the motion of the heavier ions and so a DFT convergence of the electron wavefunctions is calculated for each ion MD step. This approach gives improved results over the Car and Parrinello technique.

As one might expect, the unification of the DFT modelling with the dynamic processes of the ions increases the level of accuracy in the resulting calculated electron structure. A side-effect of employing this technique is that the system must now also be allowed to reach a thermodynamic equilibrium, i.e. the ion structure must be allowed to relax into a self-consistent configuration, before physical properties can be calculated. All DFT-MD simulations undertaken in the course of the work presented in this thesis were performed by J. Vorberger using the simulation package VASP [Kresse and Hafner [1993]]. These calculations are employed to a considerable extent in the treatment of microscopic density fluctuations described in this chapter.

4.3 Effects of variable density on ion stopping in fully ionised plasmas

The introduction to this chapter has established the necessary tools to employ a treatment of microscopic density fluctuations in a target material. We can now begin simulating energy deposition calculations and looking for discrepancies with similar calculations that employ a mean density approximation. There is currently limited experimental evidence regarding stopping power calculations in dense plasmas. We can not say that the mean density approximation is invalid in such a system. Indeed, there is also insufficient evidence to say that a proper treatment of these density fluctuations will significantly improve the accuracy of our energy deposition calculations. In this chapter several simulations are performed which model the ion stopping in systems which exhibit significant microscopic density fluctuations. The aim of this is to test the uniform density assumption from the theoretical perspective.

For this work I have written some data processing and simulation routines. I wrote a code which generates the one-dimensional density profiles seen along the alpha-particle flight path to check that the density variations would be significant. This code takes a DFT-MD profile as an input, which is a three-dimensional profile of density values, presented as a cubic grid of variable size and resolution with periodic boundary conditions. These DFT-MD profiles were generated for this work by Jan Vorberger. To extract the one dimensional density profile of a flight path through the DFT-MD box, my code generates a vector of an arbitrary direction with an arbitrary footpoint and resolves density values along this vector. This is done by applying a three-dimensional linear interpolation scheme that I have written to the eight density-valued grid points which border the location at which the density is being interpolated. This density interpolation scheme was then incorporated into a branch of a second code that I have written which is a one-dimensional particle stopping code. This code calculates stopping power values along the flight path of a single particle and iterates this stopping power over small path-length increments to slow down the simulated particle. The combination of the two gives me a product which takes a DFT-MD profile and some particle parameters as its inputs and returns some one-dimensional profiles. These profiles are of local density, stopping power and energy deposition, each resolved along the flight path of the incident particle. I have adapted this code to work with the Lenard-Balescu degenerate stopping power solver and the T-Matrix and Thomas-Fermi models which I have written and implemented although, as stated in chapter 2, the original formulae are

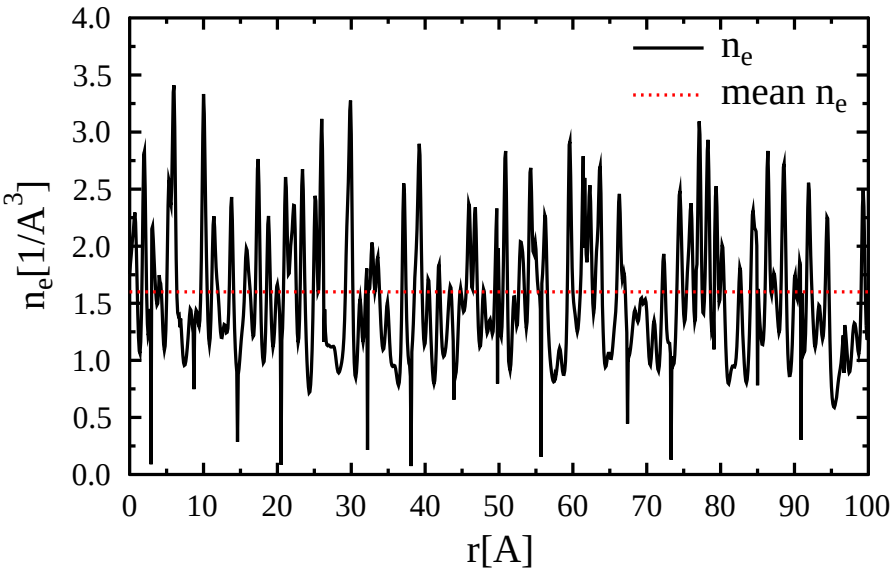

Figure 4.1: Extracted one dimensional, electron density line profile, given as an example to show the form of a DFT-MD variable density profile. This profile was extracted from a simulation box for fully-ionised dense hydrogen. The mean electron density was given by $n_e = 1.661 \times 10^{24}\,\mathrm{cm}^{-3}$ and the temperature used was $T = 10,000\,\mathrm{K}$

not my own.

This work assumes that the energy deposition of each simulation particle occurs along a straight one-dimensional path. In order to calculate the density profile along each single-particle flight trajectory, a one-dimensional density profile is extracted from the full three-dimensional DFT-MD simulation box. As a first assumption, in this work the DFT-MD density profiles are treated as static over the timescales required for particle stopping. However, one extension to this work which did not reach completion was to use time-dependent Hartree-Fock simulations to investigate the degree of variation in the electron density profiles over larger timescales. Perhaps more significantly, this would also have allowed simulation of perturbations in the electron density profile of the target that would be caused by the potential of the incident ion. Unfortunately, no conclusions of significance to this extended work were reached.

In figure 4.1 we see a clear example of a one dimensional electron density line profile that has been extracted from a three dimensional DFT-MD simulation box. The case in question is for a fully-ionised, dense hydrogen plasma, such as

might be found in the fuel of an inertial confinement fusion pellet. We can see that, despite the total ionisation, the free electron profile is not uniform and still shows significant variations in the observed electron density.

The observed fluctuations above and below the mean are of similar magnitudes to each other and constitute a similar spatial scale. One alternative form to that seen in figure 4.1 would be a profile with a large spatial extent being below the mean density and a few localised peaks of electron density much greater than the mean value . These two profiles will likely manifest quite different energy deposition behaviour because the stopping power is not linearly proportional to the electron density and so the energy deposition of the second case should be consistently lower than the mean density treatment. With the even spatial distribution of electron density above and below the mean, it is hoped that the macroscopic observables such as the energy deposition profile might still show a significant correlation with the deposition calculations for an identical plasma system using a mean density approximation. This result would be treated as justification for us using the mean density approximation for later work in similar plasma regimes. If the agreement is not observed then this will reduce the accuracy of future energy deposition calculations for burning fusion plasma applications. This is because the unaccounted variations in density would result in an increased blurring of beam energies and local heating rates due to there being a larger distribution in the calculated values.

In this investigation, we frequently use the particle range as a comparison metric to describe the cumulative stopping power a particle has experienced. The particle range is the depth to which a particle can penetrate a target medium before that incident particle has deposited all its kinetic energy. An integration over the energy deposition profile along the particle trajectory up to the particle range will return the initial particle energy. As a result, the value of the range can give some basic information about the form of the energy deposition profile. Energy deposition profiles often have a distinct recognisable form. As a particle travels through a stopping medium, it deposits energy and so it slows down and experiences a different stopping power. In each particle stopping scenario there is an optimal kinetic energy for particle stopping where the interaction cross section between the incident particle and the stopping medium is maximised. High energy particles which have kinetic energies above this optimum value will experience an increase in stopping power as they slow towards the stopping peak. All particles with energies below the optimal stopping level will experience decreasing stopping power as they slow. The result of this is the creation of a ‘Bragg peak’ where the interaction cross section is maximised which leads to high energy particles having an area of increased energy deposition

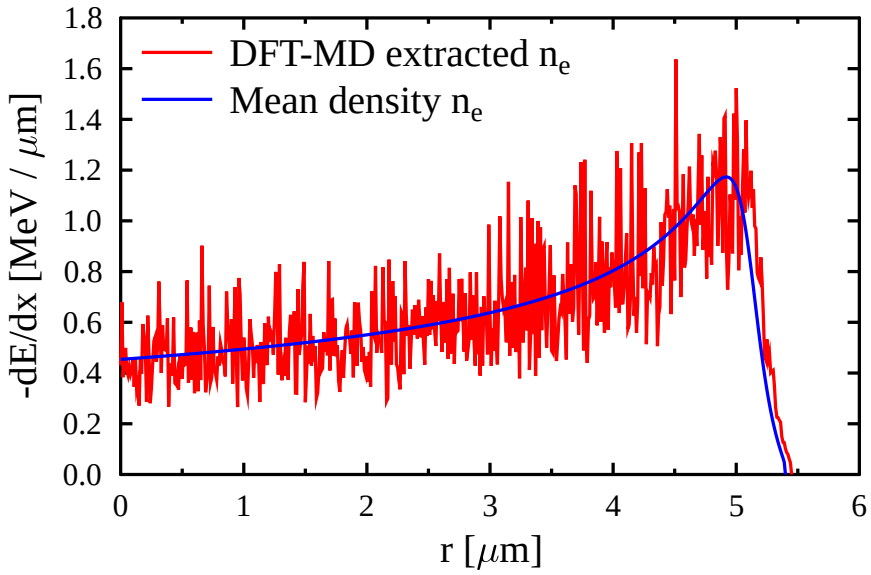

Figure 4.2: This is a comparison of alpha-particle energy deposition profiles using the Thomas-Fermi stopping model. The figure compares stopping calculations which use density values obtained from a DFT-MD profile with similar calculations using the constant mean density approximation. The plasma has a temperature of $T = 10,000\,\mathrm{K}$ and a mean electron density of $n_e = 1.661 \times 10^{24}\,\mathrm{cm}^{-3}$. The initial kinetic energy of the alpha-particles is $E = 3.5\,\mathrm{MeV}$.

near to the end of the ion range. Figure 4.2 shows the comparison of two 3.5 MeV alpha-particle energy deposition profiles. Both profiles are produced from the same plasma conditions only each case uses a different treatment of the electron density when performing stopping power calculations. It can of course be seen that, in the variable density case, there are large local fluctuations in the stopping power which are a result of the large variations in local electron density, as shown in figure 4.1. Despite these large fluctuations the general functional form of the energy deposition profile is similar to that of the mean density case and the calculated ion range is also similar to that of the mean density case. The blue mean density curve on this graph shows energy deposition against penetration depth and gives an example of a Bragg peak and the ion range. The red curve is an energy deposition profile for the same stopping conditions but with the effects of variable DFT-MD density included in the stopping power calculations.

4.3.1 Investigation into variations from beam angle and entrance location

In this work, we model real systems of non-uniform density with a periodic approximation, which in this case is the DFT-MD density profiles. When doing this, it is important to test the validity of the assumption of periodicity. Initially, this is done here by looking for aspects of the periodic profiles that might cause large variations in our energy deposition calculations. Here, we attempt to investigate the treatment of these effects in isolation.

First, it was of interest to this work to examine the effects of varying the specific point at which the beam particles are initially incident on the DFT-MD profile. It was also of interest to investigate the effects of varying the angle of this incidence. The choice of the initial point of incidence might cause unexpectedly large variations in cases where the incoming ion is initially incident in close proximity to a plasma ion, or indeed the opposing case of being initially incident in a region of significantly lower density outside the Debye spheres of all nearby plasma ions. It would be unfavourable to find that improper treatment of these single ion events would have a significant effect on the overall energy deposition profile. If a strong dependence upon the initial impact location were observed, this would make the accurate modelling the single particle case of a real physical situation significantly harder because of the difficulty encountered in identifying the initial point of incidence of the beam ions on the target material's periodic structure.

In order to attempt to isolate the effect of the point of impact, this investigation was performed by setting an alpha-particle trajectory through the DFT-MD density profile and then producing energy deposition profiles and measuring particle ranges over a variety of energies for particles that were incident at different displacements along this single path. These deposition calculations can be repeated, comparing variable and uniform density cases of several different initial impact points and beam trajectories through the three-dimensional DFT-MD profile.

Another free parameter that arises in the variable density approach is the orientation of the incident particle path through the DFT-MD profile. Like the initial point of impact, this orientation requires no consideration in the mean density case and is only of interest for variable density simulations. The effects of varying this orientation have also been investigated here for the case of a fully ionised hydrogen plasma. Due to the inhomogeneous nature of the DFT-MD electron density profile, it is possible that varying the angle of incidence of the ions may cause large changes in the resulting energy deposition profiles. This would imply that travel through a medium in one direction is not necessarily equivalent to travel through the same

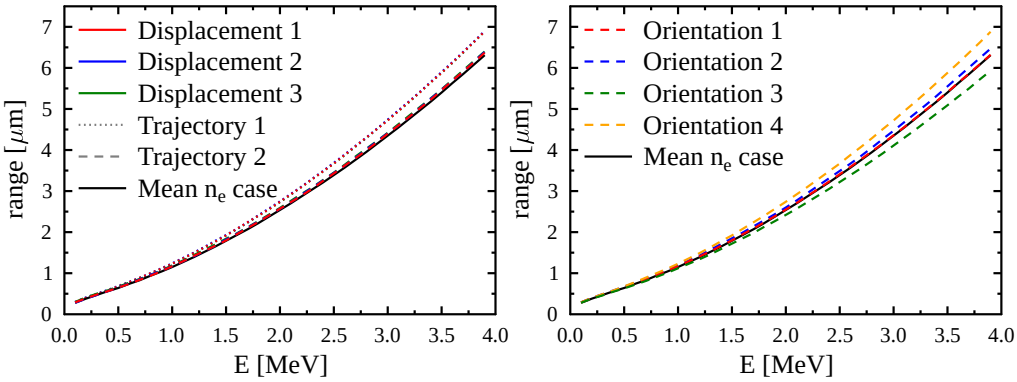

Figure 4.3: Investigation into effects of variable DFT-MD density description. The frame on the left shows examples from the investigation into varying the point of impact and its affect on particle ranges when compared to the calculated mean density approximation range values. Six cases are shown which give excellent agreement between displacement cases for a single trajectory and also show examples of trajectory cases which show agreement and deviation with respect to the mean density approximation. The frame on the right shows examples from the investigation into beam orientation where, for a fixed point of initial impact, the direction of travel through the DFT-MD profile is varied. This figure shows variation in particle ranges that are above and below the calculated ranges for the mean density approximation. All energy deposition curves were calculated in a DFT-MD electron density profile of a dense hydrogen plasma with mean electron density $n_e = 1.661 \times 10^{24}\,\mathrm{cm}^{-3}$ and temperature of $T = 10,000\,\mathrm{K}$.

medium in another direction. If this dependence is observed, the correct modelling of charged particle energy deposition on a microscopic scale would require an increase in the complexity of current simulation target models, at least on the level of reduced symmetry arguments. An investigation was done calculating particle ranges, for different initial particle energies, on an extracted density profile of fixed point of impact for several cases of angular orientation of the particle trajectory.

Figure 4.3 shows some of the relevant results from these investigations. The investigation into the point of impact concluded that, for a given particle trajectory, varying the point of impact in small increments along this trajectory has negligible effect on the final particle range, causing only range differences on the order of the DFT-MD simulation width ($\sim 1\,\mathrm{nm}$). This implies that there are no highly localised effects which cause the energy deposition profiles to be significantly altered. However, when comparing cases of different trajectories which maintained the same orientation to the DFT-MD material some significant deviation in the calculated ranges could be seen and the deviating cases diverged from the mean density cal-

culations with increasing beam energy. This shows that for completely separate paths through the DFT-MD profile, cumulative effects of the density variations are allowed to compound. Divergence from the mean density calculations is not assured though and cases are seen which deviate both above and below the mean density calculations. Over several energy values it is not uncommon to find cases which show good agreement with the mean density range calculations.

The investigation into the orientation of the beam is also summarised in figure 4.3. It shows that, by fixing the point of impact but changing the initial direction of travel, a deviation in the particle ranges can also be observed when compared to the mean density calculations. This is to be expected because the variation in the trajectory orientation produces a completely different density profile which has already been shown to result in deviation of the calculated ranges. Interestingly, the maximum deviations that were found in the cases and energy range tested were approximately equal to the maximum deviations seen in the previous test for different impact points with aligned trajectories. This is evidence for the claim that there is no preferential direction of travel through the DFT-MD simulation material. This finding also aids us in managing the computational complexity of simulating energy deposition processes in burning fusion plasmas. This is because the relative independence of the energy deposition on the orientation of the beam implies that the assumption of a spherical symmetry when considering the energy deposition behaviour is indeed reasonable. Again, it can be found that for any given point of impact, some beam orientations will often be found to agree with the calculated mean density ranges over a considerable energy regime.

In general, for both of the investigations undertaken, cases were found to give range calculations within a moderate deviation above and below the mean density approximation behaviour. Evidently the accurate simulation of a single particle case would be near impossible to match with a single particle experiment. However, in the many particle case there is likely to be a statistical describable distribution around the mean density behaviour. This distribution of ranges and energy deposition profiles should also be reflected in experiment.

4.3.2 Range comparisons between DFT and uniform electron density

There are several hypothetical cases in which the observation of large variations in electron density on a microscopic spatial scale is probable. The results of these variations should definitely be observable in the energy deposition profile of an incident particle. These variations are also quite likely to have an impact on macroscopic

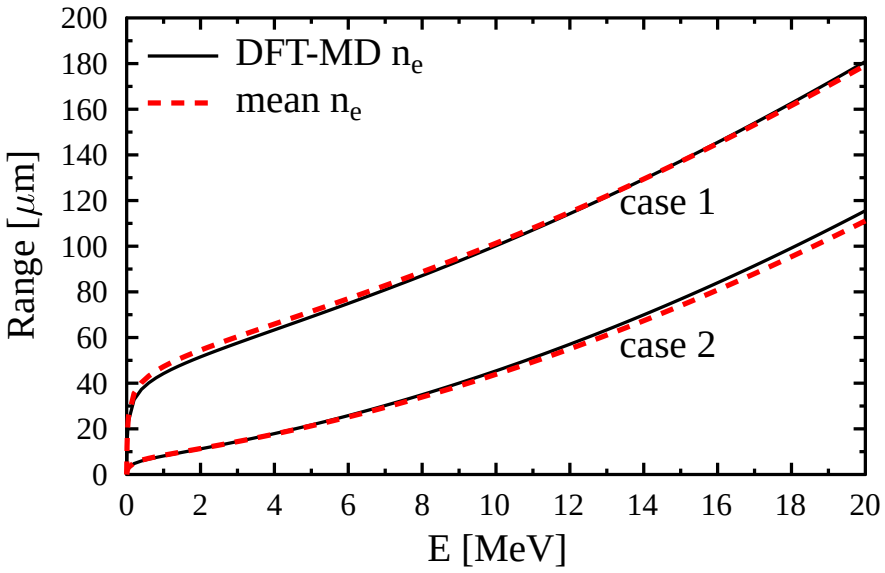

Figure 4.4: Comparison of particle ranges in DFT-MD variable density profiles with particle ranges calculated using a mean density approach. Incident particles are alpha-particles with initial kinetic energies between $0 - 20\,\mathrm{MeV}$.
Case 1 represents a fully ionised hydrogen plasma with conditions of $n_e = 1.661 \times 10^{24}\,\mathrm{cm}^{-3}$ and $T = 10,000\,\mathrm{K}$. Case 2 represents a similar hydrogen plasma with conditions of $n_e = 1.661 \times 10^{24}\,\mathrm{cm}^{-3}$ and $T = 20,000\,\mathrm{K}$.

observables of the particle trajectory, such as the ion range. Some of our previous simulations have shown good consistency in particle ranges between mean density calculations and variable density calculations. These cases have occurred in fully-ionised plasma scenarios where the beam path length is many times greater than the width of the periodic density profile. These results imply that the energy deposition profiles of incident particles can often be well approximated using a uniform, mean density treatment. This hypothesis relies on the case that for a fully ionised plasma the stopping medium will exhibit an approximately even spatial distribution of density fluctuations above and below the mean electron density. However, the simulation data also implies that there are many situations where the mean density treatment significantly underestimates the straggling of the energy deposition that arises in the variable density, DFT-MD stopping simulations. In order to investigate these cases further, a few particle stopping cases were simulated over a greater energy range to see if we could still find paths that commonly showed agreement with the mean density calculations. To investigate this hypothesis, the range comparison

investigation was extended beyond the scope of 3.5 MeV alpha-particles. Simulations were run for much higher kinetic energies and also for lower kinetic energies. This comparison was made for initial alpha-particle kinetic energies over the range of $0 - 20$ MeV. The range comparison between the two density treatments was applied to two fully ionised plasma cases of dense hydrogen with mean electron densities of $n_e = 1.661 \times 10^{24}\,\mathrm{cm}^{-3}$ and temperatures of $T = 10,000$ K and $T = 20,000$ K respectively. Figure 4.4 shows a plot of the resulting ranges calculated from energy deposition simulations. The simulation data shows a clear trend in each of the two cases. It should also be noted that there appears to be no significant divergence between the density treatments for increasing stopping range. This implies that the cumulative effects that are introduced from spanning multiple widths of the periodic DFT-MD profile will not lead to significant divergence from the mean density behaviour in some cases. These results add some support to the claim that in the case of a fully-ionised plasma system, the mean density approximation does give a good description of the electronic stopping behaviour of the plasma.

4.3.3 Effects of Density Variations on Energy Straggling in Charged Particle Beams

A beam of particles which enter a target medium of non-uniform density will not follow exactly identical paths to each other. As a result, in the case of an initially mono-energetic beam, the differences in the small variations of the energy deposition profiles of each particle will result in 'straggling' of the beam particle energies. Straggling implies that, at any given depth in the target material, the beam particles will no longer have a mono-energetic distribution of their kinetic energies. Instead, the kinetic energies of the beam particles will have a measurable spread which is denoted as the straggling of the beam. This straggling is calculated from the standard deviation of the beam particle energies as a function of target penetration depth. The straggling , $\sigma(E)$, can be simply determined as

$$\sigma(E) = \sqrt{\frac{1}{N}\sum_{i=1}^{N}(E_i - \bar{E})^2}, \tag{4.6}$$

where N represents the number of particles in the beam and $\bar{E}$ is the mean kinetic energy of these particles. With greater penetration depth, the cumulative effects of the beam straggling are expected to become more prominent and the distribution of the beam particles is expected to widen. This straggling can be calculated for the particle energies and also for the particle stopping powers. The energy straggling

shows how the distribution of particle energies will change with penetration depth and the stopping power straggling will show how the local heating will change will penetration depth. This investigation is looking for large differences in the alpha-particle energy deposition profiles that arise as a result of the DFT-MD density variations. The simulation analysis will calculate the straggling of these quantities and statistically quantify the expected variation in both the local beam particle energies and the local energy deposition, thus, heating rate.

The initial kinetic energy chosen will always be sufficiently high that the ion range within the material will allow the particle to span many of the periodic DFT-MD density profile simulation widths. For this investigation, the initial entry point of the beam ion into the DFT-MD profile will be assigned at random, as will the angle of the ion path through the simulation profile. The aim of these actions is to equally sample the inhomogeneities in the DFT-MD profile and investigate the variations in the resulting energy deposition profiles. This investigation will also be of interest for the later simulation work shown in this thesis, as it will give indications to the expected variance calculated heating and energy values. These variations will have to be estimated because the simulation work presented in chapter 5 treats the simulated stopping medium as a single uniform density object rather than as a variable density profile. The straggling analysis is first performed for dense hydrogen and then repeated for partially-ionised beryllium to investigate the effects of having prominent localised ion peaks in the DFT-MD profile. It is expected that for the case of a partially-ionised plasma the observed deviations in the energy deposition profiles will be larger than those seen in the fully-ionised hydrogen case. This is because the large, highly localised, peaks in electron density will cause far greater density deviations than the fully-ionised case. These large variations are likely to reduce the accuracy of the mean density approximation. Figure 4.5 shows an example comparison of two energy deposition profiles. It can be seen that, not only are there large deviations in the local stopping power, but also the calculated particle range differs by $\sim 5\%$ between the DFT-MD case and the mean density case.

As an overview, figure 4.6 shows simulations of the beam particle energy profiles for alpha-particles stopping in dense hydrogen, with initial kinetic energies of $E = 3.5\,\mathrm{MeV}$. The calculated beam straggling is displayed for both the local beam energies and the local heating rates given by the stopping power. The partially-ionised beryllium analysis is shown in figures 4.7 and 4.8. Figure 4.7 corresponds to a case for high energy particle stopping, i.e. where the beam velocity is very much greater than the electron thermal velocity. This high energy case produces sharp

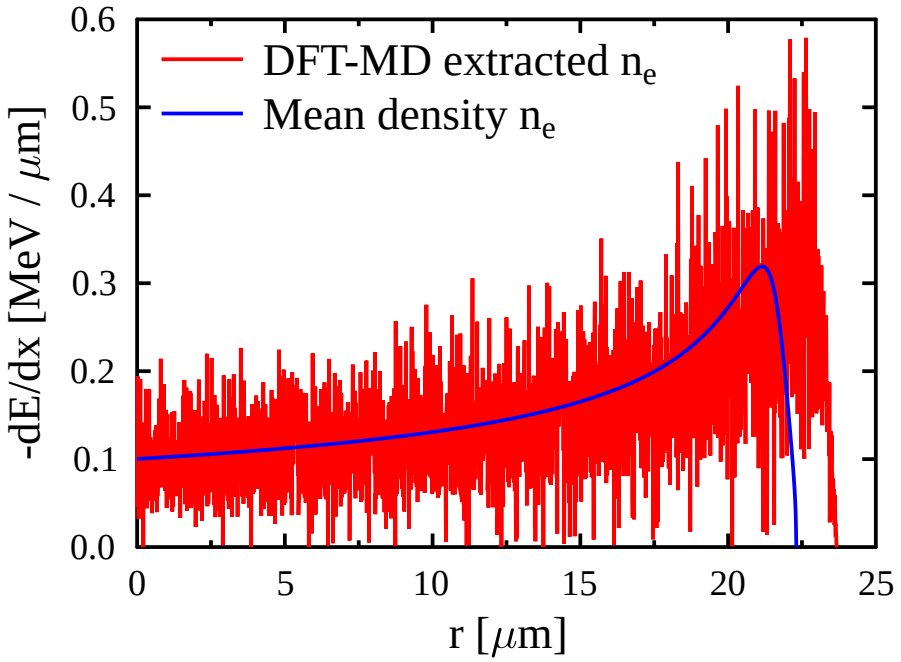

Figure 4.5: Energy deposition profiles for alpha-particles stopping in partially ionised DFT-MD beryllium compared to a similar calculation using the mean density approximation. The DFT-MD profile has $n_e = 2.469 \times 10^{23}\,\mathrm{cm}^{-3}$ and $T = 12\,eV \sim 13,900\,\mathrm{K}$. The alpha-particles have an initial kinetic energy of $E = 3.5\,\mathrm{MeV}$. The range discrepancy between the cases is large compared to the fully ionised DFT-MD simulations.

Bragg peaks and uses the full DFT-MD profile. The data presented in figure 4.8 corresponds to simulation cases of low energy particle stopping, where the beam energy is on the order of the ion binding energy. In this case, the quantised nature of the bound electron energy levels mean that only direct collisions between the incident ion and a plasma ion at almost full energy would have a non-zero cross-section for interaction. To account for the low energy case having a zero interaction cross-section, the ion peaks have been removed from the DFT-MD profile by subtracting a theoretically calculated density for a beryllium 2s electron wavefunction. To enable this simulation, I wrote a code which post processes the DFT-MD profiles to subtract the electron peaks. This code took a DFT-MD profile input, the simulated wavefunction values of the bound electron state that you wanted to remove calculated in isolation and the ion locations as they exist in the final state of the DFT-MD profile. My code then runs over this data, generating three-dimensional

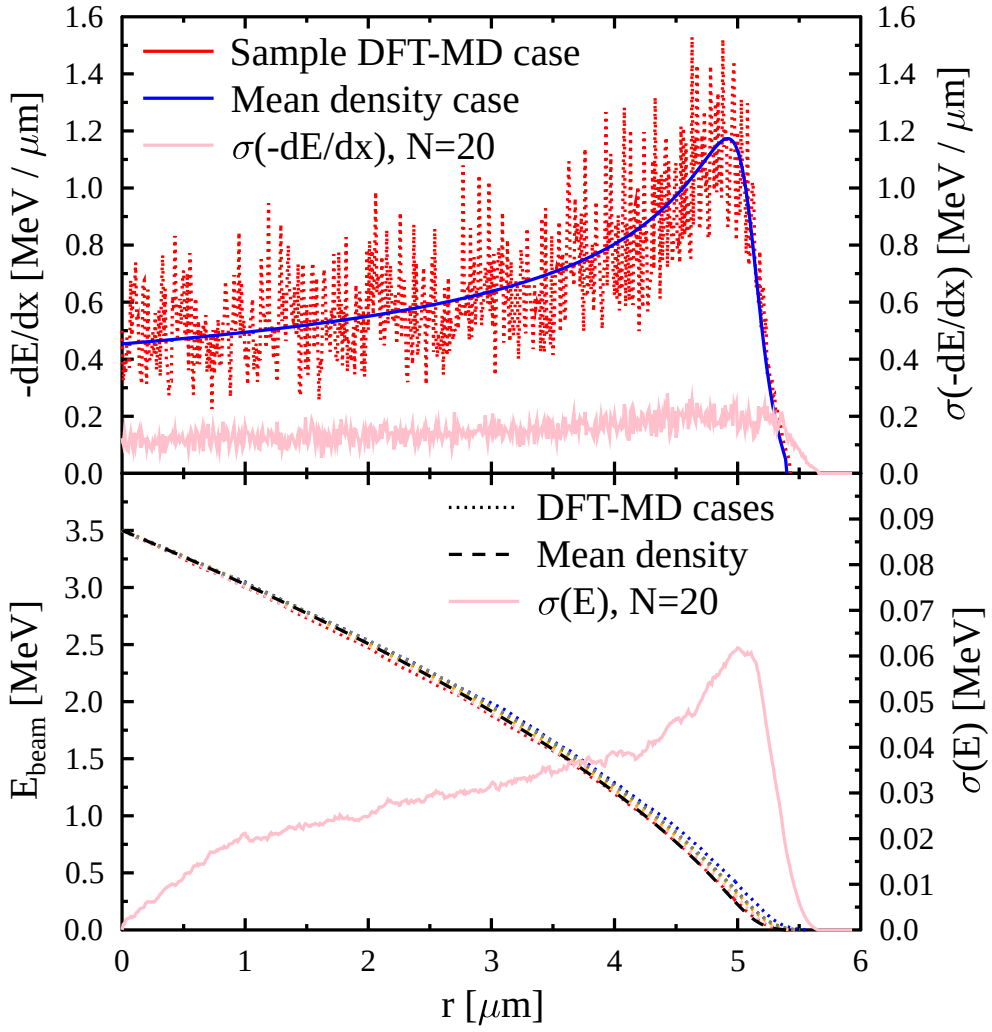

Figure 4.6: Energy and stopping power profiles as a function of target penetration depth for a simulated beam of 20 alpha-particles stopping in a dense hydrogen DFT-MD profile, $n_e = 1.661 \times 10^{24}\,\mathrm{cm}^{-3}$ and $T = 10,000\,\mathrm{K}$. The beam particles have an initial energy of $E = 3.5\,\mathrm{MeV}$, where in this case E_{beam} is used to denote the energy of a single beam particle and each separate coloured dotted line represents a different particle. The calculated energy straggling is plotted the the right hand side vertical axis. The stopping power model used in these simulations was the Thomas-Fermi model.

ion-peak density profiles from the wavefunction input and subtracting these electron states from the DFT-MD profile. The code loops over the ion locations to subtract the peaks at all of the known ion locations. Subtracting these bound electron peaks from the DFT-MD profile allows us to continue using a stopping power calculation

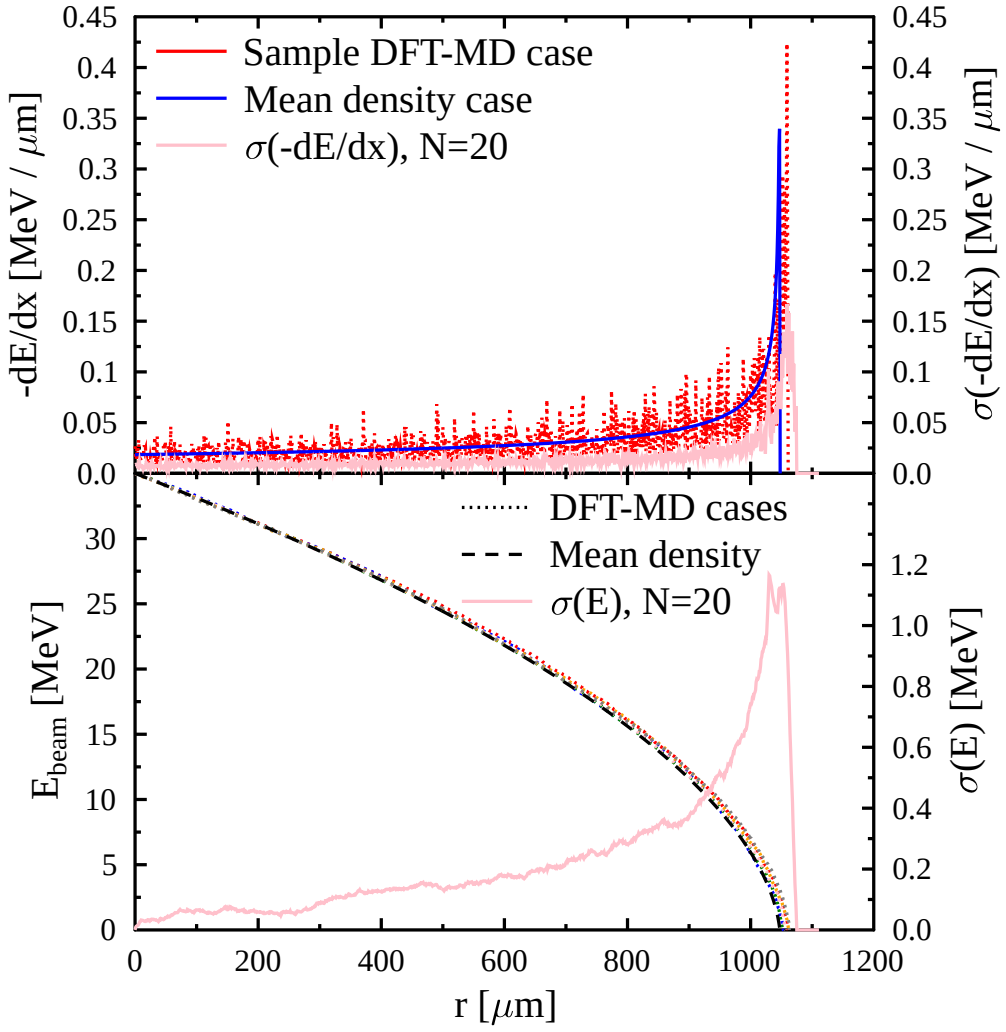

Figure 4.7: Energy profiles as a function of target penetration depth for a simulated particle stopping in a dense DFT-MD beryllium profile, $n_e = 2.469 \times 10^{23}\,\mathrm{cm}^{-3}$ and $T = 12\,\mathrm{eV} \sim 13,900\,\mathrm{K}$. In this case, the alpha-particles of the beam have an initial energy of $E = 35\,\mathrm{MeV}$ giving an initial beam velocity of slightly greater than ten times the mean electron thermal velocities in the target plasma which allows the resolution of a sharp Bragg peak.

that is based on the local electron density, but gives us some means of accounting for the zero interaction cross-section of low energy beam particles that are incident upon the bound electrons.

The hydrogen cases shown in figure 4.6 show moderate amounts of beam straggling in terms of beam energies and energy deposition. As expected the energy straggling begins at zero, as the beam is mono-energetic at 3.5 MeV. This straggling

then increases steadily with penetration depth as the effects of the density variations accumulate. The straggling peaks at approximately 15% of the local beam energy. At further depths, the straggling then decreases to zero as the particles begin to reach their range. At this point, the particle energies have decreased and as some particles will have stopped, the number of beam particles at these depths is reduced. This straggling implies that the beam particles are indeed spreading into an energy distribution. Comparisons of these beam energies with the mean density calculations shows that statistically there is a preference towards the particle energies in the variable density case being higher for a given depth than the energies in the mean density case. This implies that the particles are on average experiencing a slightly reduced stopping power in the variable density stopping simulations. The straggling of the stopping power for the hydrogen case oscillates erratically about a roughly constant mean value showing only a slight increase with penetration depth. This straggling then decreases to zero as the particles range is reached. This implies that the dominant effect in the stopping power straggling is the variations in the electron density profile and not a systematic straggling that results from some preferential behaviour of the particle energy distribution.

For the beryllium, high energy particle stopping case shown in figure 4.7 the energy straggling follows a similar form to that of the hydrogen case. However, in this case we do see that the straggling is greatly amplified in the locality of the Bragg peak. Although the beam energy is only a factor of ten higher than the hydrogen case, the peak energy straggling is a factor of twenty higher than in the previous case. Also in the Bragg peak, where the straggling is maximised, the beam straggling is on the order of the local particle energy. This is most likely a result of the larger particle range and the small width of the Bragg peak with respect to this range. For a case of increased particle range, an increased number of interactions are likely to occur before the Bragg peak. The variations in the local density seen by each of these interactions mean that the distribution of energies at the Bragg peak is likely to be wider. The stopping power straggling also begins with the same behaviour of erratic oscillation about some locally consistent mean which increases fractionally as the beam energy straggling increases. However, in this high energy case the straggling of the stopping power also exhibits a visible Bragg peak. This behaviour implies that the straggling of the stopping power is initially dominated by the variations of the electron density profile. At greater depths, the straggling of the beam energy is greatly increased. Because the stopping power is dependent on the beam energy, it is possible that if the energy straggling is large enough, it will become the dominant cause of the stopping power straggling. We think this is the

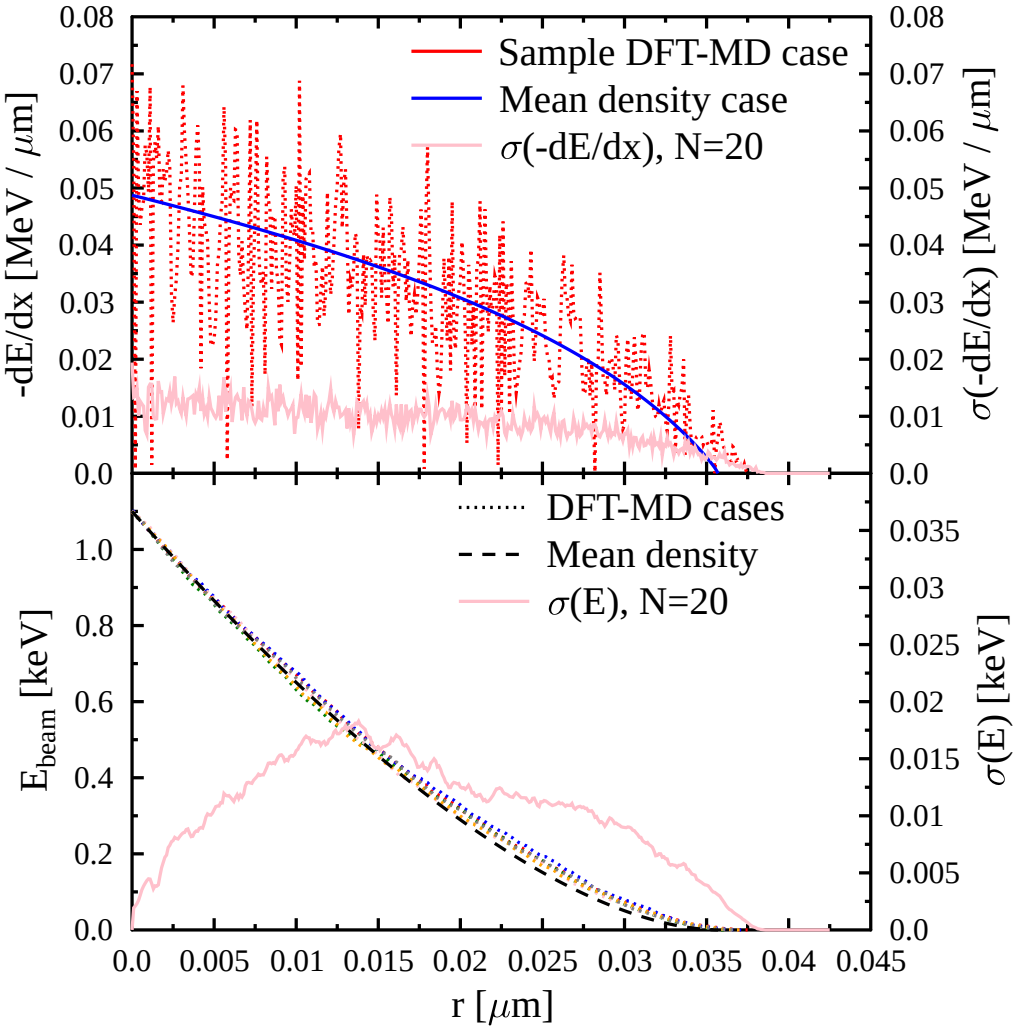

Figure 4.8: Energy profiles as a function of target penetration depth for the same partially ionised beryllium DFT-MD profile case as that shown in figure 4.7 except with the ion peaks removed which lowers the mean density to $n_e = 2.169 \times 10^{23}\,\mathrm{cm}^{-3}$. In this case, the beam particles have an initial energy of $E = 5\,E_{\mathrm{binding}} \sim 1.1\,\mathrm{keV}$. The temperature of the material is given by $T_e = 12\,\mathrm{eV}$.

case around the Bragg peak because the two straggling profiles can be seen to take the same functional form.

The final straggling case of low energy particle stopping in beryllium is shown in figure 4.8. Here the energies are low enough that the stopping power is well into the low energy, linear decrease regime. This can be seen in the form of the energy deposition profile as it decreases constantly up to the particle range. The straggling

Table 4.1: Table showing the mean range of several DFT-MD particle stopping simulations, the calculated particle ranges using the mean density approximation and the standard deviation of the calculated DFT-MD particle ranges. It can be seen that even in the fully ionised DFT-MD profile the mean density approximation behaviour does not fall within the mean of the DFT-MD cases $\pm\sigma$. However, it should also be noted that high energy Be case is in fact the most consistent between the mean ranges in terms of number of standard deviations separation.

Target	Mean n_e range (μm)	Mean of DFT ranges (μm)	σ (μm)
Be (35 MeV)	1048.0	1060.9	7.019
Be (1 keV)	0.0357	0.0375	0.000067
H (3.5 MeV)	5.40	5.49	0.042

of the beam particle energies peaks much earlier in this case than the high energy cases, at around a third of the mean particle range. This peak straggling occurs at a value of around 3% of the local beam energies. As a result this deviation never has a dominant effect of the calculated straggling of the local stopping power which is always dominated by the variations of the electron density. The particle energies and ranges in this case are very low and so the straggling profiles of both the beam energies and the stopping powers spend a large amount of the particle range in decline with little other discernible functional form.

Finally, a small statistical investigation was performed for the mean values and variances of the observed particle ranges of the straggling simulations. This was done in order to investigate the hypothesis implied by the cases shown in section 4.3.2 that, in terms of particle ranges, it is possible for the mean density approximation to be well represented by a DFT-MD treatment of the electron density. Table 4.1 shows the calculated particle range using the mean density approximation, the mean of the ranges of a sample of DFT-MD cases and the standard deviation of these ranges. This is given for the three regimes that have been investigated in the straggling analysis of this chapter. The mean density range does not lie within one standard deviation of the mean range of the DFT-MD simulation cases for any of the three regimes presented. Only the low energy beryllium case deviates by more than two standard deviations. All the cases also show that the mean range of the DFT-MD cases is longer than the range of the mean density case. The natural conclusion here is that a microscopic treatment of the electron density profile of a target medium

yields theoretical deviations from the mean density approximation and that these variations are in general small when compared to experimental error of ion stopping power measurements [Land et al. [1985]]. This means that it would be very difficult to determine any realistic regimes of relevance for this numerically intensive, variable density stopping treatment.

Chapter 5

Energy transfer in burning fusion plasmas

The goal of achieving controlled laboratory fusion is a complex matter with many design hurdles to be overcome. Currently, there is a lot of research being done into the behaviour of these fusion experiments. The hope is that we can gain a better understanding of the dynamics of fusion plasmas through laboratory experiments. It is hoped that this greater understanding will allow scientists to successfully achieve controlled fusion, a goal that is currently unattained. There are many barriers to our understanding. For the case of inertial confinement fusion concepts, the energy transfer processes that occur in the burning fusion plasma are of particular importance. The strict limitation on the confinement time of the fuel pellet has meant that previous experimental work was unable to produce significant quantities of fusion energy before the confinement was lost. It is hoped that through theoretical and experimental advances, a sufficiently optimised configuration can be found that will allow for efficient production of fusion energy in a laboratory environment.

This chapter discusses some simulation work done investigating the initiation of an inertial fusion burn wave. The simulations focused specifically on the effects of variations in stopping power and electron-ion temperature equilibration and how these affected the energy transfer dynamics. The simulation work examines the interface between the fusion hotspot and the cooler, dense fuel mass. The density and temperature regimes are chosen to represent conditions similar to those seen in fusion experiments at the National Ignition Facility [Haan et al. [2011]]. This work tests different models of particle energy deposition in several regimes. The simulations also include heat capacity calculations specific to dense plasmas and a model of electron-ion temperature equilibration that can accommodate arbitrary

electron degeneracy. These simulations investigate the initiation of the alpha-heating process from a theoretical perspective. The final analysis make an assessment of some heating timescales for different plasma parameters.

5.1 Fusion burn wave propagation

The work presented in this chapter investigates the heating of a dense hydrogen plasma by fusion-produced alpha-particles. Simulations are run which vary the modelling techniques applied to the energy transfer processes and the effects on the calculations are discussed. This topic is being investigated for its relevance to the propagation of a fusion burn wave in an inertial fusion fuel pellet. In an inertial fusion scenario, this alpha-heating process occurs after the initial, driven compression phase. At this time the fuel pellet is highly compressed and has a small, central burning region at temperatures and densities that are high enough to accommodate a rapid fusion rate. The geometry of this situation has originally been shown in this thesis in figure 1.2.

In order to begin our investigation, it is first convenient to define the transition which is hoped to be achieved through alpha-heating processes. There is still significant uncertainty about the exact temperature and density conditions which must be met to sustain a burning inertial fusion fuel pellet. As a result, whilst the methodology of analysis described here can be applied in many regimes, the simulations that are presented use initial conditions that may not give an accurate depiction of future fusion experiments. One goals of the compression phase is to maximise the particle density, which will increase the fusion rate. However, this must be achieved whilst maintaining an optimal temperature for the deuterium-tritium fusion cross-section ($T \sim 10^8$ K). It is also desirable to reduce the density gradients in the fuel pellet during compression. This is done to minimise the formation of Rayleigh-Taylor instabilities that can cause unwanted fuel mixing during the pellet compression. Figure 5.1 shows a plot of the density and temperature plane for deuterium-tritium plasmas. The heating transition that is expected between the compressed fuel and the fusion hotspot is highlighted with the arrow marked, α. This is the transition which will need to be driven by the energy of fusion-produced alpha-particles. As shown by the arrow marking the α path, the temperature transition simulated here runs from $T_e = T_i = 50\,\mathrm{eV}$ to $T_i = 5\,\mathrm{keV}$. However, unlike the transition marked on figure 5.1, the density of the fuel being heated is considered to be static on the timescales that are simulated. The calculations of the alpha-heating simulation use density values of $n_e = 3.16 \times 10^{26}\,\mathrm{cm}^{-3}$ in the compressed fuel and

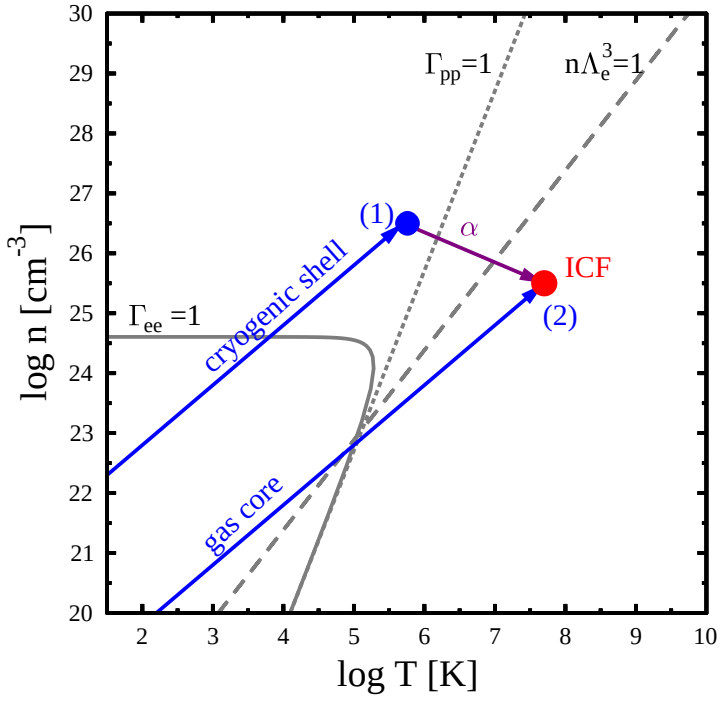

Figure 5.1: Phase space diagram in the density and temperature plane (courtesy of Jan Vorberger). This diagram labels the transition that the inertial fusion concept would require to be driven by alpha-particle heating. The conditions at point (1) are $T = 50\,\mathrm{eV}$ and $n_e = 3.16 \times 10^{26}\,\mathrm{cm}^{-3}$. The conditions at point (2) are $T = 5\,\mathrm{keV}$ and density $n_e = 2.40 \times 10^{25}\,\mathrm{cm}^{-3}$.

$n_e = 2.40 \times 10^{25}\,\mathrm{cm}^{-3}$ in the hotspot. It can be seen from the division of figure 5.1 that the alpha-heating transition happens in a regime of significant electron coupling ($\Gamma_{ee} > 1$). The transition also crosses the threshold between regimes of significant and non-significant ion coupling ($\Gamma_{pp} = 1$). The threshold for electron degeneracy ($n_e\Lambda_e^3 = 1$) is also crossed by plasma heated through this regime. The exact phase space location between these particular regions will dictate the appropriate physics that will need to be included when modelling each simulation regime.

This investigation aims only to simulate these energy transfer processes and investigate some heating timescales for the initiation of the fusion burn wave. The work presented here does not extend to the full spatial propagation of the fusion burn wave through the volume of the compressed fuel pellet. This is because, at greater simulation times, many of the assumptions used in this modelling will break down (no hydro-motion, no radiative losses).

5.2 Energy transfer chain

In order to successfully model the alpha-particle heating in an inertial fusion scenario, it is important to perform detailed calculations of the energy transfer processes involved. The energy transfer chain that is of particular interest here is the transfer of the kinetic energy of fusion-produced alpha-particles to the thermal energy of the fuel ions. This transfer happens in several stages and is an important mechanism for sustaining the fusion temperatures of an inertial fusion hotspot. Some uncertainties encountered in this modelling are a result of the current limits of experimental data, although the generalised methodology can be applied after a more detailed knowledge of the experimental conditions is available. Inertial confinement fusion operates in a very high energy regime and so the properties of the high energy density states of matter (HEDM) that are created in inertial fusion are less well understood than those of matter in lower temperature and pressure regimes. However, it is known that in HEDM the quantum nature of the material will become significant. In this section a fully quantum theoretical description of the alpha-heating energy transfer processes is presented.

Once the initial ablation and compression phases, described in section 1.4.1, are complete, simulation data says that the fuel capsule should form two distinct regions whose densities and temperatures are given approximately by points 1 and 2 on figure 5.1. The relatively low temperatures of these states, i.e. $T \leq 5\,\mathrm{keV}$, mean that when calculating the stopping of alpha-particles, the stopping power contributions are dominated by electron interactions. This is particularly true of the cooler, denser bulk of the fuel. The cooler, outer fuel must be heated to fusion conditions by alpha-particles without the aid of an external driver and so the energy deposition in this fuel is of particular interest. Once the alpha-particle kinetic energy has been transferred to the fuel electrons, via stopping power calculations, the energy source for alpha-heating of electrons is then established. The electron temperature increase can then be calculated after some analysis of the equation of state of the electrons. However, as the desired deuterium-tritium fusion interactions are ion-ion interactions, it is the temperature profile of the fuel ions which will dictate the progress of the burn wave. On a picosecond timescale, the electrons of the target medium incur numerous collisional interactions with their neighbouring ions and can transfer sufficient energy to equilibrate the temperatures of the ion and electron populations. This electron-ion energy equilibration is calculated using a similar treatment to the quantum kinetic derivations of stopping power. Similarly to stopping power, the temperature relaxation models can be adjusted to account

for the effects of increased coupling strength and electron degeneracy simulated medium. The final stage of the transfer chain is that the energy transferred to the target ions causes an increase in the temperature of the ion population. This increase can be calculated using a second equation of state that is applied to the ions. As the simulation evolves in time, the form of the ion temperature profile will indicate the position of the fusion burn wave and the shape of the burn front.

5.2.1 Alpha-particle stopping power

The energy deposition profiles of fusion-produced alpha-particles are calculated from stopping power models. In this analysis, the only contribution to the stopping power that is considered is the energy transfer from alpha-particles to the electrons of the compressed fuel medium. The relatively low ion temperatures mean that the cross-section for alpha-particle interactions with deuterium and tritium ions is small and so these stopping power contributions are neglected. The work of Li and Petrasso [Li and Petrasso [1993]] shows a comprehensive table covering a range of temperature values for a fixed density. This table shows the relative fractions of total energy deposition between the electrons and ions of the target medium for different temperatures. Although the table is calculated for a different density value than that which is employed here, the table illustrates the transition between electron dominated stopping power and ion dominated stopping power. In can be seen that, as the temperature increases, the ion stopping contributions become a significantly larger fraction of the total stopping power. This trend continues for temperatures of several tens of kilo-electronvolts until the ion stopping becomes the dominant contribution to the stopping power and the electron stopping can be neglected. For the temperature regime described by this simulation work, there is little difference in the calculated energy deposition profiles when the ion-ion interaction contributions to the stopping power are accounted for. As a result, the effects of ion stopping are neglected at these temperatures and only the transfer of kinetic energy to the target electrons is considered.

The low temperatures seen in the compressed fuel also mean that the regimes being investigated are expected to exhibit significant effects of degeneracy in their electron systems. Figure 5.2 shows a comparison of some different stopping power models in different temperature and density regimes. The figure aims to highlight the effects that electron degeneracy can have on stopping power calculations. These effects can be seen in the the significant differences between the results of calculations which include a proper description of degeneracy and calculations which do not. It can be seen that, in the case of low degeneracy, variations in the calculated stopping

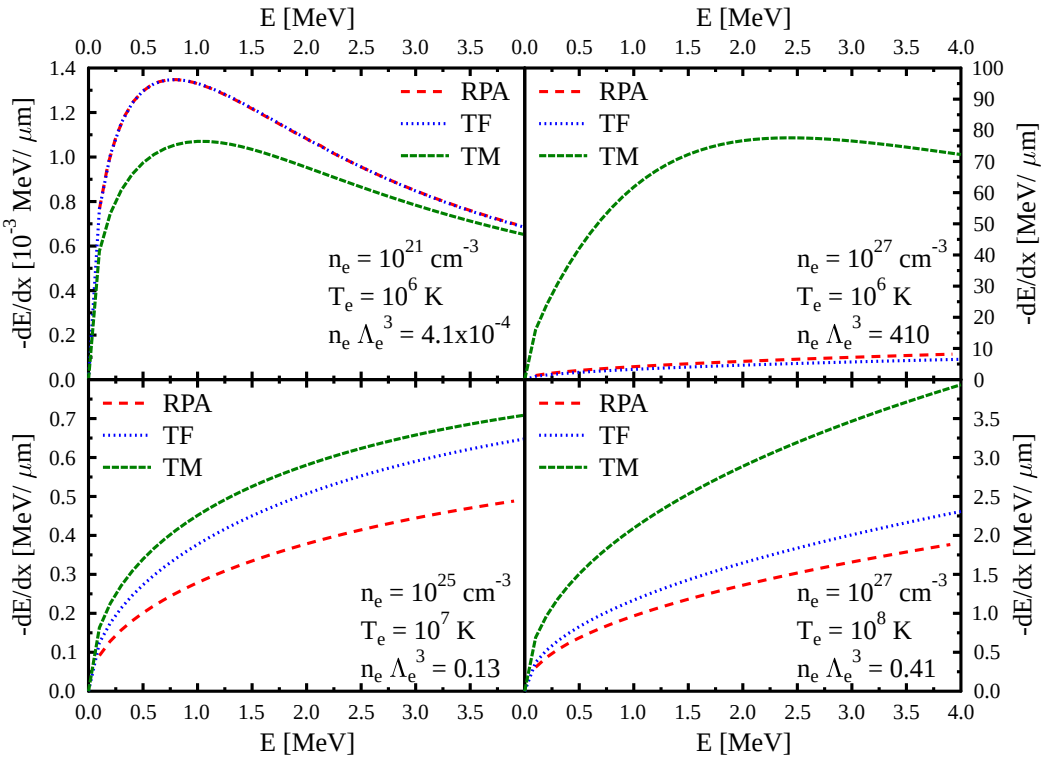

Figure 5.2: Comparison of degenerate and non degenerate stopping power models in plasmas of different degeneracies. 'RPA' denotes the Lenard-Balescu RPA dielectric function approach. 'TF' denotes the Thomas-Fermi numerical model for stopping power in degenerate systems and 'TM' denotes the T-Matrix binary collision approach. This figure shows examples of the effect that electron degeneracy can have on charged particle stopping power.

power between models is often small. However, when the level of degeneracy in the target medium is increased, the stopping power calculations begin to diverge between models which include a treatment of electron degeneracy and models which do not include such a treatment. Figure 5.2 shows that the effects of electron degeneracy in the target medium can cause deviations which amount to an order of magnitude difference in the calculated stopping power. These differences in the stopping power would also have a dramatic effect on the resulting energy deposition profiles of the alpha-particles. The final result of this could mean that a proper treatment of electron degeneracy in the target medium will significantly alter the alpha-heating mechanism by which energy is transferred to the fuel ions.

In this simulation work, the models of stopping power that are applied are varied in order to investigate their impact upon the alpha-particle kinetic energy deposition. These stopping power calculations comprise the first step in the energy

transfer chain of the simulation work covered in this chapter.

5.2.2 Electron and ion heat capacities

In the previous subsection, we describe why the alpha-particle energy deposition will heat the electrons of the target fuel and not the ions. The next step in the transfer chain is to calculate the increase in electron temperature that results from this energy deposition using an equation of state model for the electrons. A similar calculation will also be applied later to calculate the evolution of the temperature of the ion population. In order to convert between measures of temperature and measures of internal energy, you need to know the equation of state of the particle population that you are investigating. In the case of this inertial fusion simulation, the material that is under investigation is in a regime such that it forms a dense plasma. The phase-space regimes in which dense plasmas exist imply that it is important to include a quantum treatment of this particle system. Neglecting quantum effects in the electron or ion heat capacity calculations for this system could result in temperature errors amounting to as much as a few orders of magnitude. This would significantly affect the dynamics of our simulations. Correct calculation of the electron and ion heat capacities are an important aspect of this analysis. Particularly because the time-evolution of the ion temperature was an original motivation for the investigation. From a modelling perspective, the ion system of the post-compression fuel is less complicated than the degenerate electron system. As a result, the ion internal energies can be calculated using a less complex model than that which is used for calculating the internal energies of the electron population. The equation of state models which we use for calculating internal energies in this simulation work are given as

$$U_e = U_e^{\text{ideal}} + U_e^{\text{HF}} + U_e^{\text{MW}}\,, \tag{5.1}$$

$$U_i = \frac{3}{2}k_B T + 2\pi n_i^2 \int_0^\infty dr\, r^2 \Big[g_{ii}(r) - 1\Big] V_{Debye}(r)\,, \tag{5.2}$$

where $g_{ii}(r)$ is the ion pair distribution function and for all terms the subscript e corresponds to electron quantities and the subscript i corresponds to ion quantities. The terms U_e^{HF} and U_e^{MW}, from equation (5.1), are the Hartree-Fock and Montroll-Ward corrections to the electron internal energy for dense plasma systems. These corrections are the first and second order terms respectively that are obtained upon inclusion of higher order loop Feynman diagrams when treating the system with a statically screened ladder approximation. Equation 5.2 shows the ideal ion internal

energy, plus a correction to the ion ideal internal energy calculated from ion-ion electrostatic interaction contributions using a Debye-screened Coulomb approximation.

Once the internal energies of the system have been mapped over a suitable parameter range, the specific heat capacities can be calculated by simply extracting the local gradient from the internal energy profile with respect to temperature.

$$C_a^V = \frac{\partial U_a}{\partial T_a}. \tag{5.3}$$

From this, it is easy to convert a calculated energy increase into a corresponding temperature increase for the given particle species. This is important in the second transfer step, after calculating the energy transfer from alpha-particle stopping, and in the final transfer step, where the electron energy decreases and the ion energy increases as a result of electron-ion equilibration processes.

5.2.3 Electron-ion temperature equilibration

The third step in the simulated energy transfer chain is the electron-ion temperature equilibration stage. The fusion burn wave propagation is dictated not by the electron temperature of the fuel, but by the ion temperature of the fuel. In order for any assertions about the burn wave propagation to be made, it is necessary for the simulation work to include a treatment of the ion temperature and not just the energy transfer of alpha-particles to electrons. In this work the ion temperature lags behind the electron temperature, often quite significantly, as the ions are heated only through electron-ion temperature equilibration processes. These electron-ion temperature equilibration processes are modelled using the coupled mode temperature equilibration model, which is described in the work of Vorberger et al. [Vorberger et al. [2011]]. This coupled mode approach is also derived from the Lenard-Balescu kinetic equation and so can describe the effects of electron degeneracy which are significant in the initial stages of the heating process.

$$Z_{ei}(t) \;=\; -\mathcal{V}\hbar \int \frac{d^3\mathbf{q}}{(2\pi\hbar)^3} \int_0^\infty \frac{d\omega}{2\pi}\, \omega \left|V_{ei}(q)\right|^2 \frac{\mathcal{A}_e(\mathbf{q};\omega,t)\, \mathcal{A}_i(\mathbf{q};\omega,t)\, \Delta N_B(\omega)}{\left|1 - \mathcal{L}_e^R(\mathbf{q};\omega,t)\, \mathcal{L}_i^R(\mathbf{q};\omega,t)\, V_{ei}^2(q)\right|^2}\,. \tag{5.4}$$

Equation 5.4 is from the work of Vorberger et al. [Vorberger et al. [2011]] and describes the electron-ion energy transfer between populations of different temper-

atures. The numerator terms $\mathcal{A}_e(\mathbf{q};\omega,t)\,\mathcal{A}_i(\mathbf{q};\omega,t)$ are density response functions which describe the reaction of the electrons and ions respectively to the potential of the system. The denominator terms $1-\mathcal{L}_e^R(\mathbf{q};\omega,t)\mathcal{L}_i^R(\mathbf{q};\omega,t)V_{ei}^2(q)$ are an expression of the dielectric function of the medium and gives the screening of the local potential. In very dense plasma regimes, this model is a significant improvement over temperature relaxation calculations from a binary collision approximation using a different kinetic equation as described in the work of [Gericke et al. [2002]]. This is because the level of degeneracy causes the plasma to behave in a weakly-coupled fashion. As a result, the effect of collisions on the plasma behaviour becomes less significant than collective effects, which binary collision models are unable to account for.

5.3 Modelling of alpha-heating

Previous approaches to simulating alpha-heating use many simplifying assumptions to find a reduced format for modelling the vast number of alpha-particles that are produced by a burning inertial fusion pellet. Calculations have been made such as ensuring energy balance between the total alpha-particle production and the internal energy difference between the post-compression and fully burning fuel. This calculation can imply that the alpha energy that a pellet can produce is sufficient to heat the fuel pellet to fusion conditions. However, the alpha-heating process is time-dependent. There is a finite limit on the confinement time of the capsule and so it is not guaranteed that the entire capsule will reach a thermal equilibrium in this time. As a result, it is inaccurate to say that having an available fusion yield that would be sufficient to ignite the entire capsule will cause a burn wave to propagate successfully. The creation of a hotspot alone will not result in a successful inertial fusion design and so the fine details of the burn wave propagation are of great importance in constructing an efficient method of power production. This work hopes to improve the assumptions made in some respects for inertial fusion scenarios. However, in order to isolate some features of interest, these simulations neglect many features which are significant to real inertial fusion scenarios, such as hydro-motion and radiative/conductive energy transfer.

The aim of this project is to investigate the initiation of a fusion burn wave in an inertial fusion fuel pellet by way of alpha-heating. The main concern is not yet the propagation of the burn wave but simply the time taken for initiation of the burn wave and also the form of the final electron and ion temperature profiles. In these simulations, the burn wave initiation was defined as heating the compressed

fuel that is located directly at the interface with the fusion hotspot from $T_i = 50\,\mathrm{eV}$ to $T_i = 5\mathrm{keV}$ using only the energy input from alpha-particles. This work is focused on the dynamics described here because of the short interaction timescales and the enormous density of the materials being simulated. In order to model the described situation, I have written a particle energy deposition simulation. The simulation describes a system of post-compression fusion fuel adjacent to the central hotspot which acts as an alpha-particle source of a predetermined energy distribution. The simulation considers only very localised heating of a shell of compressed fuel that is directly adjacent to the burning hotspot. Figure 5.3 shows the 'adjacent plasma shell' which represents the region of compressed fuel in which this simulation work is being performed.

The simulations begin with the uniform radial temperature profiles of the electron and ion populations being initialised to $T = 50\,\mathrm{eV}$. The temperature profiles run radially outwards and begin where the edge of the fusion hotspot meets the compressed fuel. A source of alpha-particles being produced at fusion energies, $E_\alpha \leq 3.5\,\mathrm{MeV}$ is then generated which enter the simulation with an energy distribution that includes the effects of energy loss within the fusion hotspot. To obtain this distribution, I have produced an analytical description of the path length that an alpha particle born with arbitrary position and direction will travel within the hotspot before it reaches the interface with the dense fuel bulk. I then performed energy loss calculations for the alpha-particles within the hotspot from my combined T-matrix stopping power code and applied these to my analytical path-length distribution. These calculations allowed me to produce the distribution of alpha-particle energies shown in figure 5.7.

The alpha-particles enter the simulation domain with this distribution of energies and their energy deposition in the compressed fuel is calculated using stopping power calculations. The simulation then evolves the energy transfer chain described in section 5.2 until the cool fuel that is in contact with the hotspot reaches a temperature of $5\,\mathrm{keV}$. At this point, our predetermined 'ignition condition' is met and the simulation ends.

During the simulation, the alpha-particle flux is modelled using a system of quasi-particles depositing energy along a linear ion trajectory of uniform density and variable temperature. This simplification is justified by enforcing spherical symmetry on the fuel pellet, which is experimentally seen not to be valid in inertial fusion scenarios. Each timestep, a weighted particle is released into the simulation domain. This weighted quasi-particle is evolved to simulate the energy deposition of a calculated number of 'real' alpha-particles of identical energy. The simulation

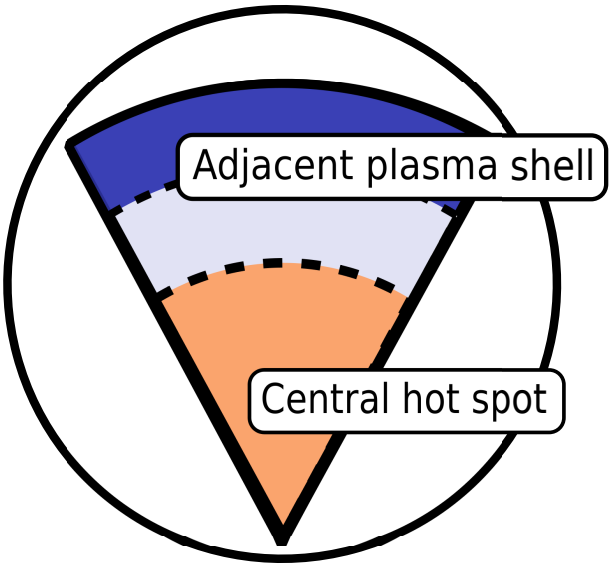

Figure 5.3: This is a visualisation which shows the theoretical simulation geometry that is being investigated. The figure shows the small plasma region adjacent to the burning hotspot where the initial alpha-heating is localised. The simulation investigates the evolution in time of the ion and electron temperature in this first fuel 'layer'.

temperature and density are initialised to $T = 50\,\mathrm{eV}$ and $n_e = 3.16 \times 10^{26}\,\mathrm{cm}^{-3}$ in the compressed fuel. The density remains constant throughout the simulation because our alpha-heating process occurs on a timescale that is far smaller than that of any hydro-motion of the fuel. The simulated variations in the electron and ion temperature profiles are evolved in sub-femtosecond timesteps. Throughout the course of the simulation, the radial ion and electron temperature profiles are recorded at variable intervals, generally on the order of tens of femtoseconds. This provides a clear picture of the relationships between the temperatures of the electron and ion populations. Visualisations are constructed from the time-resolved output of the electron and ion temperature profiles and some of these results will be presented in this chapter. This method is thought to be sufficient for investigating the effects of energy transfer processes on the initiation of the fusion burn wave, however, full burn wave simulations which run over larger timescales would need the inclusion of hydro-motion, radiative losses and a non-static simulation of the hotspot.

5.3.1 Simulation geometry

In order to ease the complexity of modelling the alpha-heating scenario, the symmetrical geometry of the spherical fuel pellet can be exploited. From this symmetry it is logical to divide the investigation domain up into many identical radial segments of small angular extent. The projected spherical nature of the hotspot and the homogeneous spatial distribution of the alpha-particles allows us to assume that the burn wave will travel radially outwards and will also have a similarly spherical form. The rotationally symmetric nature of the whole system allows for the assumption of periodic boundaries at the angular edges of our defined radial simulation segments and so the identical nature of the segments and their time evolution requires only one segment to be simulated. The simulation is then reduced to a one dimensional radial simulation of a general spherical geometry. The alpha-particle energy deposition calculations are reduced to a fully one-dimensional calculation, and the kinetic energy of the alpha particles is deposited in radial grid-cells. This geometry also allows the radius of the simulated hotspot to be easily varied. This size is fixed between simulation cases in order to investigate the effects of the hotspot radius on the final heating timescales. The hotspot could be continuously expanded without any significant increase in computational effort, although this analysis will not be covered here. As the hotspot itself falls outside the recorded simulation domain, the main effect on the simulation that the hotspot radius has is on the heating calculations. This is because the grid-cells are defined by radial co-ordinate and angular extent. As a result, the volume of the radial grid-cells increases as a function of the radial co-ordinate. This becomes most significant in the calculation of internal energies and local temperatures. The grid-cell volume is an important parameter here because it is necessary to account for the number of particles that the deposited energy is being distributed over.

5.3.2 Distribution of alpha-particle path lengths within the hotspot

Alpha-particles will be produced from deuterium-tritium fusion interactions, which are assumed to be localised to the fusion hotspot. The alpha-particle production rate can be calculated as a function of the density, temperature, volume of the hotspot and the fusion cross-sections for the deuterium-tritium fusion reaction. Within the hotspot, alpha-particles are simulated as being created continuously at uniformly distributed locations and with uniformly distributed directions of travel. In the case of the simulation work that is presented here, the alpha-particle production rate is a fixed constant throughout the entire simulation time. For investigative purposes,

in this simulation work the alpha-particle production rate is defined manually and used as a free parameter. This means that it often differs from the physical value obtained from the fusion cross-section calculation based on the volume of the burning hotspot. The energy of alpha-particle production is uniform, i.e. particles are created in the 'hotspot' at $E = 3.5\,\mathrm{MeV}$. However, it is thought to be unphysical to have a fully uniform source of alpha-particles entering the compressed fuel. In order to improve this treatment, the alpha-particles enter the simulation domain with a predetermined energy distribution. This distribution is calculated here from a geometric distribution of paths combined with numerically calculated energy deposition data.

Some assumptions are made when calculating an analytical expression for the energy distribution of the alpha-particles that we employ. The first assumption made is that because of the change in density between the hotspot and the outer fuel, the expected alpha-particle path will be much smaller in the cooler denser fuel than it is in the hotspot. We will use averaged quasi-particles in the simulation and so we assume these particles take a mean, radially outwards direction of flight in the dense fuel. Considering the energy propagation of a statistically large sample of alpha-particles in this geometry, the assumption that the energy propagates radially outwards is valid, though assuming that the projection of the trajectory is fully radial as is assumed here does introduce some uncertainty. However, this assumption allows the one dimensional geometry used for the simulation domain and also allows a fully analytical and generalised path length distribution to be derived.

The initial distribution of fusion alpha-particle kinetic energies upon creation is of course isotropic and described by a delta function at an energy value of approximately $E = 3.5\,\mathrm{MeV}$. Immediately after creation, these alpha-particles will then begin collisional interactions with the particles of the surrounding medium and start depositing their kinetic energy. In this simulation, it is important to find the statistical distribution that describes how far the alpha-particles will have travelled within the hotspot before reaching the compressed fuel. This is because the hotspot is not directly simulated and in reality the alpha-particles are not created at the origin of the simulation domain, i.e. directly on the interface between the hotspot and the fuel bulk. Once the distribution of path lengths has been derived, non-degenerate binary collision energy deposition calculations can be performed to obtain a kinetic energy distribution from the distribution of path lengths.

Only the numerical distribution of the path lengths is of interest here and not any information regarding the three-dimensional spatial distribution of these paths, which is assumed to be uniform. To obtain the numerical distribution, the

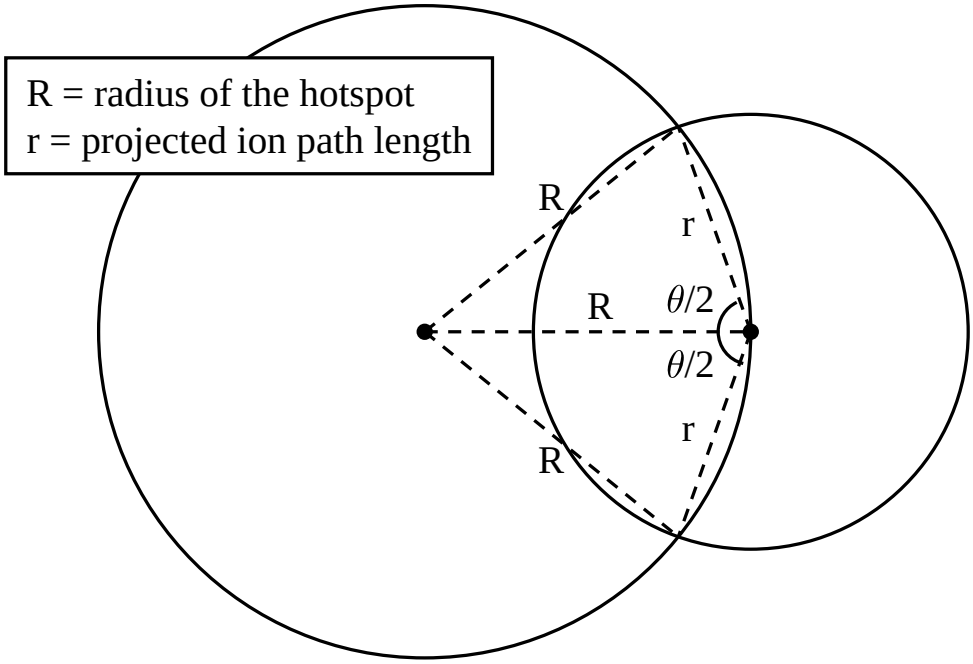

Figure 5.4: Two dimensional visual representation of the geometry for possible alpha-particle contributions for an ion path length, r, in a hotspot of radius, R. The contributing volume can be calculated from a three dimensional calculation of two intersecting spheres using the geometry represented here.

complete angular symmetry allows for free rotation of the system. This allows any location of creation and direction of travel to be rotated to represent any of a set of different particles with different locations of creation and directions of travel without altering the distribution of path lengths. The result of this is that the distribution of all path lengths to all points on the hotspot radius will be equal to the distribution of all path lengths to a single point on the hotspot radius. From this assumption about the geometry of the particle distribution, there will effectively be an infinitesimally thin shell of burning plasma that could possibly contribute alpha-particles for any given path length within the hotspot. The cumulative distribution function of path lengths can then be obtained by writing an expression for this contributing volume in terms of the path length and integrating this expression for all path lengths over the diameter of the hotspot. This can be calculated by considering the general case for an ion path, r, to be travelled within a spherical hotspot of radius, R. For clarity, figure 5.4 provides a two dimensional visualisation of this situation and acts as an aid to understanding in the derivation of the ion path length distribution. The contributing volume of all possible paths of length, r, will take the form of an infinitesimally thin, sphere segment of arc radius, r, and

angular extent, θ. Examining the dotted construction lines in figure 5.4 it is easy to isolate an isosceles triangle with the two equal sides of length R and the third side of length r. From here we can express the angle, θ, from

$$\cos\left(\frac{\theta}{2}\right) = \frac{r/2}{R}, \quad \Longrightarrow \quad \theta = 2\cos^{-1}\left(\frac{r}{2R}\right). \tag{5.5}$$

It is then possible to use θ in calculating the arc length of contribution, which is simply θ in radians multiplied by the arc radius. In this case the arc radius is given by the ion path length in question, r. Beginning with a volume integral in spherical coordinates

$$V(r,\theta,\phi) = \int_0^{2\pi}\int_0^{\pi}\int_0^{r} r^2 \sin\theta \, dr d\theta d\phi. \tag{5.6}$$

The area of a spherical arc segment, where r is the arc radius and θ is the full angular extent of the arc, can be determined by performing the angular parts of the spherical volume integral up to a limit of $\theta/2$ in the θ co-ordinate.

$$A_{\text{shell}}(r,\theta) = \int_0^{2\pi}\int_0^{\theta/2} r^2 \sin\theta \, d\theta d\phi. \quad \Longrightarrow \quad A_{\text{shell}}(r,\theta) = 2\pi r^2\left[1-\cos\left(\frac{\theta}{2}\right)\right]. \tag{5.7}$$

Inserting equation (5.5) into equation (5.7) removes the dependence of the arc area on the θ co-ordinate. This yields an expression for the shell area that is only dependent on the r co-ordinate and the chosen hotspot radius, R. Giving these shells an infinitesimal thickness, dr, we have an expression for the contributing volume of plasma which can create alpha-particles which will travel a given path length within the hotspot.

$$V_{\text{shell}}(r) = A_{\text{shell}}(r)\, dr = 2\pi r^2\left[1-\frac{r}{2R}\right] dr, \tag{5.8}$$

where r is the range travelled by the 3.5 MeV alpha-particle before leaving the fusion hotspot, R is the radius of the fusion hotspot and dr is the infinitesimal thickness of the contributing shell. This shell volume approach, when extended over the whole volume of the sphere, $r = 2R$, uses spherical symmetry to account in an analogous fashion for all possible alpha-particle production locations and directions of travel. Integrating these volume shells over the full hotspot diameter will yield the volume of the whole hotspot as expected. As a result we can obtain a probabilistic expression for the occurrence of a given path length by normalising the shell volume expression by the total hotspot volume. Then we are left with a function which describes

the distribution of possible ion path lengths as a function of r and which returns unity when integrated over the entire domain of the distribution. This probability distribution, $P(r)$, is the final goal of our derivation and is as expressed in the following form

$$\int_0^{2R} P(r)dr \quad = \quad \int_0^{2R} \frac{V_{\text{shell}}}{V_{\text{hotspot}}} = 1 \tag{5.9}$$

$$P(r) = \frac{2\pi r^2 \left[1 - \frac{r}{2R}\right]}{\frac{4}{3}\pi R^3} \quad \Longrightarrow \quad P(r) = \frac{3}{2R^3}\left(r^2 - \frac{r^3}{2R}\right) \tag{5.10}$$

Integrating this distribution over all r values within the hotspot ($r = 0 \rightarrow 2R$), it can be seen that this probability distribution is indeed already correctly normalised. However, the form of equation(5.10) is not the simplest form for the intended use of this distribution, which is assigning simulated alpha-particle energies. In order to employ this expression when generating alpha-particles in the simulation, the cumulative distribution function (CDF) was calculated.

When assigning particle energies in the simulation, a random real number between zero and one is generated from a numerical generator which produces an approximately flat distribution of output values. The cumulative distribution function, whose value runs from zero to one, can then be interpolated using a bisection method to return the path length associated with the generated number. An initial energy deposition plot of a 3.5 MeV alpha-particle within the fusion hotspot can then be interpolated using the assigned ion path length. This calculation will give the remaining kinetic energy of the alpha-particle when it enters the simulation domain. By considering all possible path lengths, the full energy distribution can be seen. Due to the simple polynomial form of the initial distribution function, $P(r)$, the CDF can be calculated analytically with minimal effort.

$$\text{CDF}(r) \quad = \quad \frac{3}{2R^3}\int_0^r r^2 - \frac{r^3}{2R} \tag{5.11}$$

$$\text{CDF}(r) \quad = \quad \frac{r^3}{2R^3} - \frac{3r^4}{16R^4} \tag{5.12}$$

I have also written a simulation in order to confirm the statistical agreement of this approach with the distribution obtained from generation of randomly directed particles. This simulation worked by generating particles within a three dimensional, spherical simulation domain. The particles were randomly assigned position

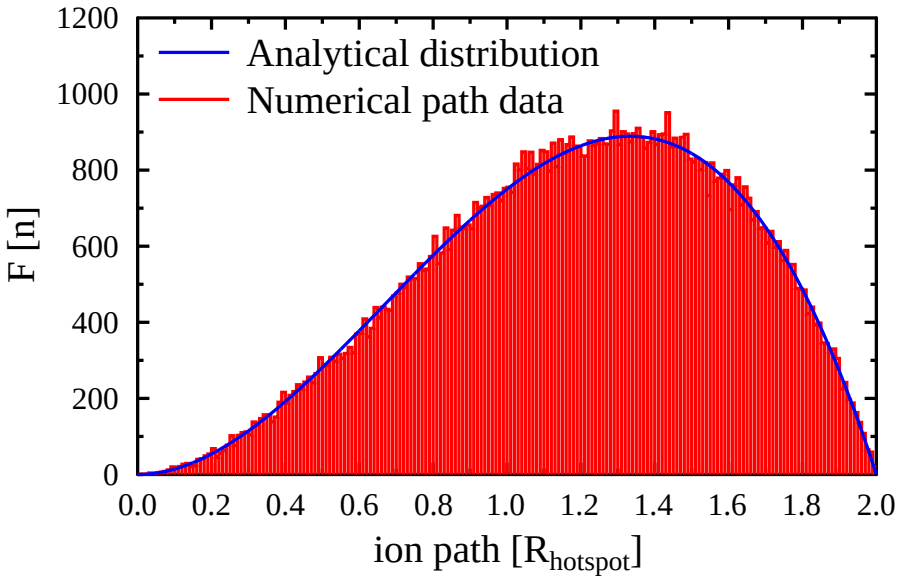

Figure 5.5: Histogram of the length of simulated ion paths within the spherical domain of the fusion hotspot with scaled analytical distribution model overlayed. Agreement between two models is clear for this case of $N = 10^5$ simulation particles in 100 histogram bins. This agreement can be seen to improve or degrade with an increase or decrease in the number of simulated path lengths respectively as is statistically expected.

an velocity vectors within the simulation using a hypercube rejection method. The simulation simply generates a number of particles with the conditions stated and then records the distance that each given particle would travel to reach the edge of the spherical simulation domain. The calculated analytical distribution functions can then be compared to the simulated path lengths, expressing this distance travelled as a multiple of the radius of the simulation domain. The hypercube rejection method was chosen because it provides a convenient way of applying a random number generator with a flat distribution to produce direction-vectors on a spherical geometry, where the distribution of vectors within the sphere fully rotationally invariant. The method works by generating three vector components (x, y, z) in Cartesian space to produce a resultant vector from the origin. Any vectors whose endpoint lies outside the unit sphere are rejected from the distribution. The method generates points in Cartesian space because applying a flat distribution to θ and ϕ in spherical co-ordinates causes grouping of the vectors around the poles. Simply generating points in Cartesian space, i.e. over a cubic domain, would lead to a dis-

tribution of direction-vectors that is more concentrated around the vertices of the cube and so the rejection stage is employed in order to make the vector distribution rotationally invariant within the sphere.

The graph shown in figure 5.5 implies that the accuracy of the calculated analytical distribution is high compared with the distribution seen in the simulated data. This is some evidence that the derived distribution of path lengths is representative of the path length distribution for a fully three dimensional simulation. This agreement is also observed for simulation cases of differing domain radius and particle number.

5.3.3 Alpha-particle energy distribution

Now that a distribution of possible path lengths has been acquired this still needs to be post-processed to produce a distribution of alpha-particle energies leaving the hotspot. In order to obtain this distribution, it is necessary to calculate the alpha-particle energy deposition profile within the burning hotspot.

The calculations shown in figure 5.6 allow the remaining kinetic energy of a fusion alpha-particle to be calculated for a given path length travelled within the hotspot. Figure 5.6 illustrates the form of the stopping power as a function of alpha-particle energy but also shows the case of a 3.5 MeV alpha-particle stopping in a dense plasma in the regime of the simulation hotspot. This profile can easily be interpolated to obtain the remaining kinetic energy of an alpha-particle upon exiting the hotspot. In general the lower density of the hotspot region means it is not in a degenerate regime and implies that the T-matrix model is more applicable. The T-matrix model is employed for hotspot calculations within the code. However, hotspot alpha stopping calculations from two models are presented in figure 5.6 and the difference in the calculated results is used to quantify the uncertainty in the hotspot deposition calculations.

If the alpha-particle path within the hotspot would exceed the alpha-particle range within the hotspot then the particle would enter the simulation domain with no energy. In order to avoid these unnecessary calculations, the simulation distribution function is limited to the alpha-particle range and the particle flux entering the simulation is scaled accordingly. The fraction of the total particles produced in the hotspot that will enter the simulation domain is easily calculated from equation (5.12) by calculating the value of the cumulative distribution function at, $r = r_\alpha$, where r_α is the alpha-particle range. This is how the distribution of initial alpha-particle energies is calculated. Plotting this distribution allows some calculations about the heating supplied by these simulation approximations to be made.

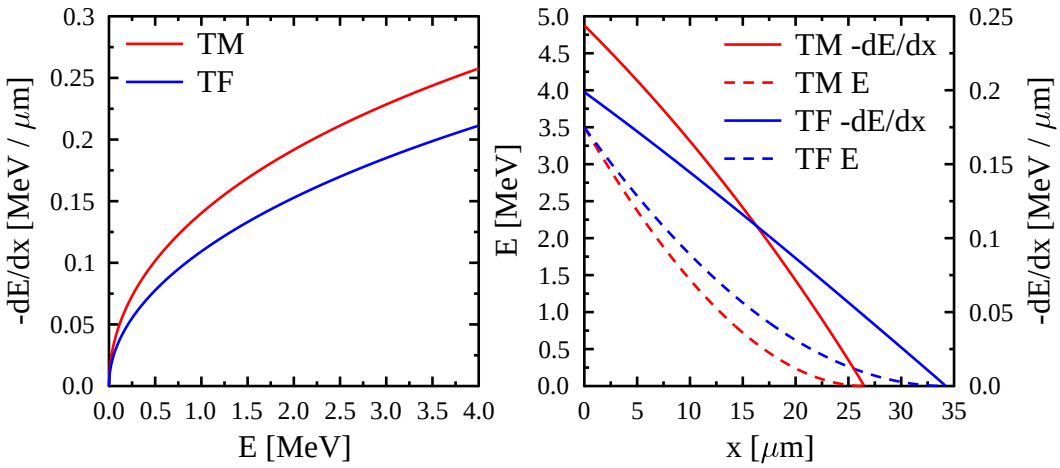

Figure 5.6: Energy deposition calculations within the hotspot. The left frame shows the behaviour of the alpha-particle stopping power against kinetic energy for a range of beam energies from $E = 0 - 4\,\text{MeV}$. The right frame shows the resulting alpha-particle Bragg curves and their associated energy profiles for the case of a $E = 3.5\,\text{MeV}$ alpha-particle stopping within the dense plasma medium of the burning fusion hotspot. The conditions of the hotspot electron system are $n_e = 2.41 \times 10^{25}\,\text{cm}^{-3}$ and $T_e = 5.8 \times 10^7\,\text{K}$. The figures show comparisons between two models, the T-Matrix (TM) binary collision model and the Thomas-Fermi (TF) interpolation model.

Figure 5.7 shows the energy distribution of alpha-particles upon leaving the fusion hotspot. The figure also labels the mean kinetic energy of these alpha particles. The validity of this distribution relies on the hotspot being treated as a steady-state alpha-particle production source, which in turn relies on the assumptions that all of the hotspot is burning, the propagation velocity of the burn front is slow compared the to alpha-particle velocity and that time since fusion reactions began is greater than the alpha-particle range in the hotspot divided by the alpha-particle velocity, i.e. initiation of the original hotspot was a process that occurred in a picosecond timescale or greater.

From the alpha-particle energy distribution we can obtain a simple equation for the heating power from alpha-particles being supplied to the outer fuel in this scenario. This function is strongly dependent on the alpha-particle range in the hotspot and the hotspot radius. Using the mean alpha-particle kinetic energy, which is calculated from the distribution shown in figure 5.7 and the fraction of alpha-particles escaping the hotspot from equation 5.12, we can obtain the following expression

$$P_{\alpha-\text{heating}} = \frac{d\alpha}{dt} \times \left(\frac{r_\alpha^3}{2R^3} - \frac{3r_\alpha^4}{16R^4} \right) \times \langle E_\alpha \rangle \tag{5.13}$$

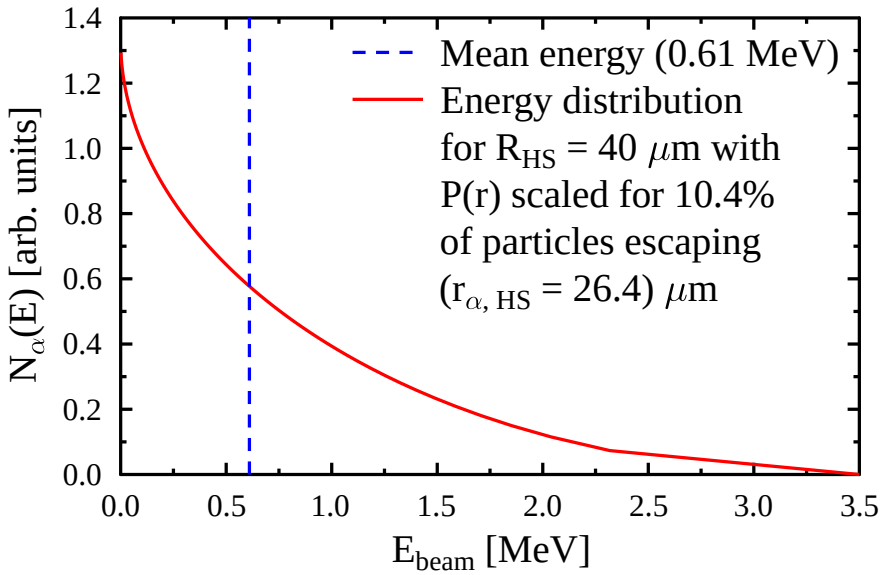

Figure 5.7: Distribution of alpha-particle energies entering the simulation domain for a hotspot of radius $R_{HS} = 40\,\mu$m and an alpha range within the hotspot of $r_{\alpha,HS} = 26.4\,\mu$m.

in which $P_{\alpha-\text{heating}}$ is the power being supplied for alpha-heating to the fuel bulk in terms of available kinetic energy of alpha-particles, $\frac{d\alpha}{dt}$ is the number of alpha-particles being created by fusion interactions in the hotspot, $\left(\frac{r_\alpha^3}{2R^3} - \frac{3r_\alpha^4}{16R^4}\right)$ is the fraction of these particles which are created with locations and velocities that will allow the particles to leave the hotspot (r_α being the range of an alpha-particle in the hotspot and R being the hotspot radius) and $\langle E_\alpha \rangle$ is the expectation value of the kinetic energy of the alpha-particles which do leave the hotspot and enter the cold fuel. Now calculating the rate of alpha-particle production from the fusion cross-section it is possible to calculate an optimal hotspot size for heating in this simulation regime.

$$\begin{aligned} P_{\alpha-\text{heating}} &= \langle \sigma v \rangle (T) \cdot n_D n_T V \times \left(\frac{r_\alpha^3}{2R^3} - \frac{3r_\alpha^4}{16R^4}\right) \times \langle E_\alpha \rangle \\ &= \langle \sigma v \rangle (T) \cdot n_D n_T \times \left(\frac{4}{3}\pi R^3\right) \times \left(\frac{r_\alpha^3}{2R^3} - \frac{3r_\alpha^4}{16R^4}\right) \times \langle E_\alpha \rangle \\ &= \frac{1}{2} \langle \sigma v \rangle (T) \cdot n_D n_T \times \frac{4\pi r_\alpha^3}{3} \times \left(1 - \frac{3r_\alpha}{8R}\right) \times \langle E_\alpha \rangle \end{aligned} \tag{5.14}$$

In this simulation geometry it can be seen that if the alpha-particle production

rate is calculated from the hotspot volume, the optimal case is for a hotspot large enough such that $r_\alpha/R \sim 0$. However, it can also be seen that there is indeed a limiting heating rate which is given by the total expectation value of the fusion energy entering the simulation from a hemisphere of radius, $r = r_\alpha$. However, an interesting effect has been observed in this geometry, that the hotspot appears to be largely opaque to the alpha-particle radiation. This can be seen in equation (5.12), where the mathematics for $r_\alpha \lesssim R_{\mathrm{HS}}$ implies that only a small percentage of alpha particles will reach the edge of the hotspot, and also in figure 5.7 which shows that of the particles that do reach the hotspot edge there is a strong preference for lower kinetic energy values. Scaling the energy for the geometric availability of alpha-particles for heating and for the mean energy of the heating particles implies that only $\sim 2\%$ of the total alpha-particle energy will be available for propagating the burn wave.

5.4 Timescales of simulated burn wave initiation

The full alpha-particle heating simulation that has been described was run in several regimes. These simulations investigated the way in which heating times were affected by variations in the hotspot size, variations in the rate of alpha-particle production from the hotspot and the inclusion of electron degeneracy in the stopping power calculations. In this section, the analysis will concentrate mostly on the time taken for the initial plasma layer to reach the defined 'ignition' condition and the energy and temperature distributions seen in the electron and ion populations at this time. Figure 5.8 shows some typical output from the simulation code. Radial temperature profiles of the ion and electron population are recorded. These profiles begin at the interface between the hotspot and the compressed fuel and extend radially into the fuel bulk. These temperature profiles are then evolved in time and snapshots of the profiles are recorded at intermediate steps. These profiles are presented to show the time evolution of the heating, both in the maximum magnitude of the temperature and also the spatial distribution of the temperature. The parameters of the simulation can then be modified and the simulation repeated. This allows the dependence of the observed heating upon each simulation variable to be described. The separation of the electron and ion temperature profiles can be seen in figure 5.8 as the ions are heated to the ignition condition on a picosecond timescale.

Whilst investigating the effects of varying the alpha-particle production rate, a transitional behaviour was observed between these cases of lower and higher alpha-particle production rate. A threshold is observed in the modelling of dense plasmas

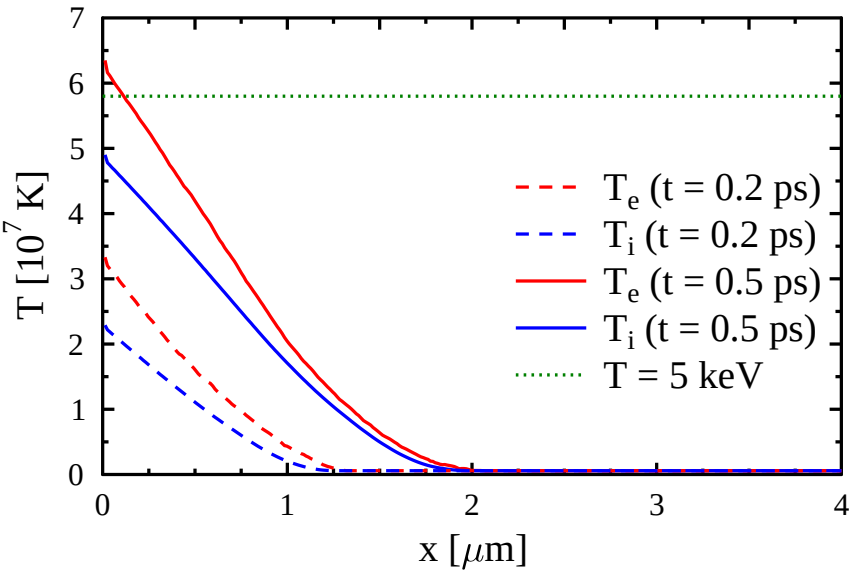

Figure 5.8: Example output from the alpha-heating simulation. This graph presents some data from an alpha-heating simulation using the Thomas-Fermi stopping model for an alpha-particle production rate of $d\alpha/dt = 10^{28}\,\mathrm{s}^{-1}$ and a hotspot radius of $R_{HS} = 10\mu\mathrm{m}$. The output is one-dimensional and the $x = 0$ point represents the hotspot edge whilst positive x extends into the fuel bulk.

at temperatures where electron degeneracy is still a significant factor for energy deposition calculations. The choice of stopping power model is seen to be a significant factor in determining the fuel heating rate at lower alpha-particle production rates, such that the electron-ion temperature equilibration times are small compared to the electron heating timescales. However, if the alpha-particle production rates are high enough that the electron heating happens on a much smaller timescale than the electron-ion temperature equilibration, then a change in the ion heating rate is observed. For the case of rapid electron heating, the temperature of the electron population becomes so much higher than the ion temperature that the temperature equilibration rate dictates the ion population behaviour.

Several cases were compared for differing alpha-particle production rates and also for stopping power models which did and did not include the effects of degeneracy. In figure 5.9 we can see a notable difference in the functional form of the heating profiles between the cases of degenerate and non-degenerate stopping power models. This is a result of the reduced heating rates seen at this lower alpha-particle production rate. The effect is that there is greater time for temperature

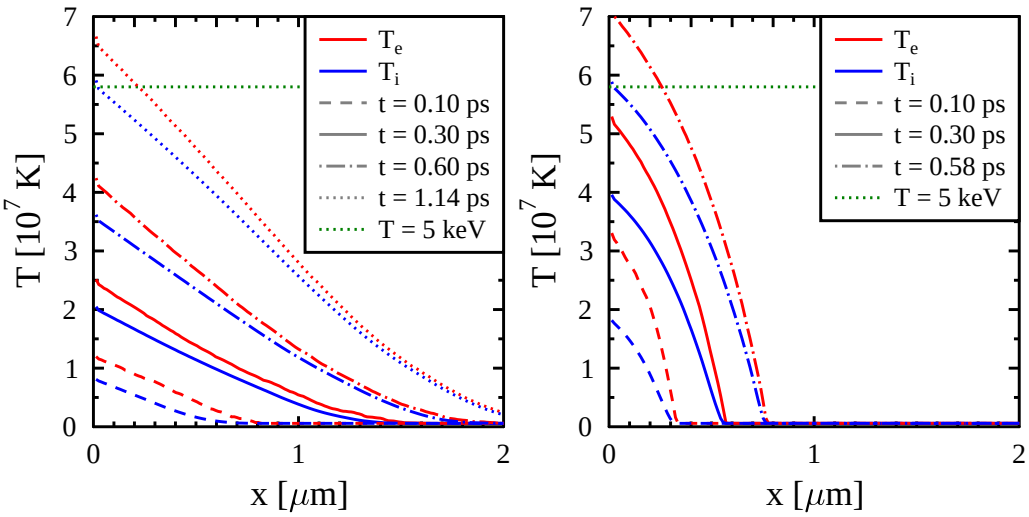

Figure 5.9: Visualisation of some radial temperature profiles that have come from the one dimensional alpha-heating simulation. Showing the form of the temperature profiles as a function of radius measured in the dense fuel bulk beginning from the edge of a hotspot of $R_{HS} = 10\mu m$. These frames are from simulations using a total alpha-particle production rate of $d\alpha/dt = 5 \times 10^{27}\,\mathrm{s}^{-1}$. The frame on the left hand side shows results which include a treatment of electron degeneracy in the energy deposition from the Thomas-Fermi model and the frames on the right employs the T-Matrix stopping power model with no treatment of degeneracy. The simulations which produced these frames both use the Spitzer fit to the coupled mode approximation to model the electron ion energy transfer processes.

equilibration to happen before the electron population is heated back into the non-degenerate temperature regime which means that the earlier heating is spread more evenly between the electrons and the ions. Since a degenerate electron target gives a reduced stopping power, we also see that the energy deposition is spread over a larger penetration depth. Figures 5.9 and 5.10 show some key simulation output for this analysis. It can be seen that in the case of a lower alpha-particle production rate ($d\alpha/dt = 10^{28}\,\mathrm{s}^{-1}$) the correct treatment of electron degeneracy effects in the fuel bulk will increase the initial heating times by more than a factor of two. We can also see from these cases that the inclusion of effects of electron degeneracy also has a significant impact of the form of the temperature profiles and the spatial distribution of the alpha-particle energy through the fuel bulk. Figure 5.10 also shows that for the case of a significantly higher alpha-particle production rate ($d\alpha/dt = 10^{30}\,\mathrm{s}^{-1}$) the ion heating times are found to be nearly identical between the case which includes degeneracy effects and the case which does not, even at the femtosecond scale. The form of the ion temperature profiles also remains consistent

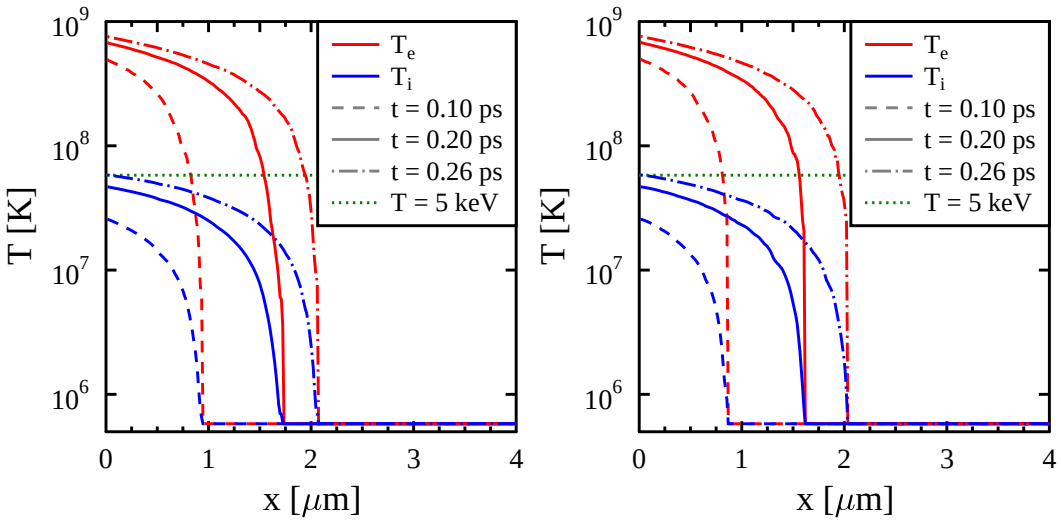

Figure 5.10: Visualisation of some radial temperature profiles that have come from the one dimensional alpha-heating simulation. Showing the form of the temperature profiles as a function of radius measured in the dense fuel bulk beginning from the edge of a hotspot of $R_{HS} = 10\mu m$. These frames are from simulations using a total alpha-particle production rate of $d\alpha/dt = 1 \times 10^{30}\,\mathrm{s}^{-1}$. The frame on the left hand side shows results which include a treatment of electron degeneracy in the energy deposition from the Thomas-Fermi model and the frames on the right employs the T-Matrix stopping power model with no treatment of degeneracy. The simulations which produced these frames both use the Spitzer fit to the coupled mode approximation to model the electron ion energy transfer processes.

between the two rapid heating cases shown here, which has also been observed in cases where the electron temperature profiles show quite different forms.

The investigation implies that the alpha-heating rates can be increased by increasing the density of alpha-particle production. This can be achieved in these simulations by reducing the hotspot size or increasing the alpha-particle production rate. Figure 5.11 presents a summary of these heating times. The calculated heating behaviour is that for a fixed fusion alpha-particle production rate, an increase in the hotspot radius will reduce the rate at which the fuel heats because the heating power is then spread across a larger fuel volume. Similarly, for a fixed hotspot radius, increasing the rate of alpha-particle production will increase the available heating power. This will then increase the rate at which the heating of the fuel bulk occurs. These findings quite naturally imply that the alpha-particle production rate per unit volume fusion fuel is a controlling factor in calculating the rate of the fuel bulk heating. The effects of electron degeneracy on the energy deposition of the incident alpha-particles can become quite large in regimes of increased electron

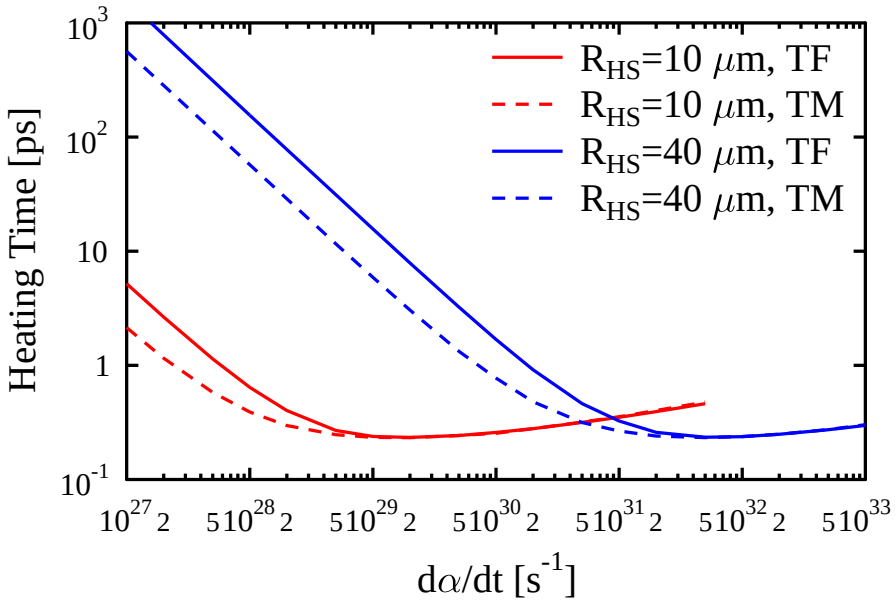

Figure 5.11: Heating times to reach the proscribed ignition condition against alpha particle production rate. Cases are shown for an hotspot radius of $R_{\mathrm{HS}} = 40\,\mu$m and a reduced hotspot case of $R_{\mathrm{HS}} = 10\,\mu$m. The convergence of the heating times between the simulations with and without the description of electron degeneracy is attributed to the limitations on the energy transfer rate from electrons to ions. The increase in heating times that can be observed at very high alpha-particle production rates is associated with the decrease in interaction cross-section of the electrons and ions in these extreme temperature cases.

degeneracy. This acts to both slow the local heating times of the fuel bulk and also to deposit the kinetic energy over a larger volume of the compressed fuel. As a result, electron degeneracy is considered to be impeding the propagation of the burn wave initiation through the fusion capsule. This means that significant electron degeneracy would have a negative impact on inertial fusion efficiency. However, without a fully propagating burn wave simulation, it is not clear whether the wider distribution of the heating energy will aid in the later propagation of the burn wave. These degeneracy effects seem greatly diminished for the case of very high alpha-particle production rates. In these cases, the rapid alpha-heating causes the electrons to leave the degenerate regime before the ion temperature profile has begun to react to the heating. In these cases the choice of stopping power model has little effect on the final heating timescales. Finally, figure 5.11 shows that for very high heating rates there is a corresponding increase in the calculated heating times. This increase in heating time is associated with the decrease in the interaction

cross-section of the electrons and ions of the compressed fuel. This means that for the case of temperature differences between the electrons and ions of several orders of magnitude, the electron-ion temperature equilibration is damped and the propagation of the burnwave is inhibited.

In simulations which both include and neglect degeneracy effects, the inner shell of the fusion fuel adjacent to the hotspot was still heated from the post compression temperature to the burn initiation temperature on a picosecond timescale. This heating rate is consistent with a working fusion concept which burns on confinement timescales predicted in previous simulation work. The order of the simulated confinement timescales is generally on the order of tens of nanoseconds [Djaoui [1995]], which has been reflected in inertial fusion experiments at the NIF. However, on these large timescales the assumptions made in the simulations presented in this chapter will become invalid. This is because of assumptions such as neglecting radiative processes and hydrodynamic-motion of the fuel. As a result, this simulation is only employed to identify the dominant energy transfer processes of initial alpha-heating and also to provide an insight into the differences resulting from including effects of electron degeneracy into the energy deposition calculations.

The conclusion drawn from this simulation data is that effects of electron degeneracy are important when considering the energy deposition of charged particles in a dense plasma. However, for the case of inertial confinement fusion, the observed effects of rapid electron heating should eliminate the need for the inclusion of this effect in simulation work. The effects of electron degeneracy have been significant in the lower alpha-particle production rate simulations presented here. However, the heating timescales associated with these alpha-particle production rates would be too long to provide the driving energy for the successful propagation of a fusion burn wave.

Chapter 6

Conclusions

6.1 Summary

This thesis presented some simulation-based investigations into energy deposition of fast ions in various dense plasma regimes. The simulations presented have offered a theoretical perspective on the behaviour of particle stopping, and other energy transfer processes, in dense plasma scenarios. Several questions have been answered by this work, however, an incremental increase in knowledge will always raise new questions that could be answered by future investigations. The main conclusions of the work in this thesis can be summarised briefly by the following paragraphs.

In chapter 3, we investigated some modelling approaches to charged-particle stopping in partially-ionised plasmas. Specifically, we looked at the case of Hartree-Fock modelling of bound electron wavefunctions being used in place of uniform mean density approximations. We made calculations of the key input quantities to the T-matrix stopping power, specifically the scattering phase-shifts and momentum-transport cross-section. These quantities were calculated for the cases of 2+ ionised Beryllium and bare Coulomb potentials for $Z = 2$ and $Z = 4$, which are the limiting potentials for the ionised beryllium case. This work aimed to investigate whether introducing extended bound electron functions would cause significant differences in the values of these calculated cross-sections. By examining the results, the effects of the different electron modelling methods can be seen from both the calculated scattering phase shifts and the calculated momentum transport cross-sections. These values are displayed in figures 3.6, 3.7 and 3.8. The cross-sections calculated using the Hartree-Fock modelling show a transition between the two bare potential cases. These profiles return similar cross-sections to the $Z = 2$ case for low momenta impact values and similar cross-sections to the $Z = 4$ case for higher impact mo-

menta. This implies that some averaging of the cross-sections between pure linear Coulomb calculations might provide a good approximation in some cases. However, the calculations from the Hartree-Fock case also show non-linear alterations in the functional form of the momentum-transport cross-sections, such as variable numbers of peaks seen at low momentum values. These features could not easily be replicated by an averaging of cross-sections between the limiting Coulomb cases and instead the averaging should be performed on the input potential. This implies that the Hartree-Fock treatment of the bound electrons would cause changes in the stopping power calculated for this partially-ionised medium compared to modelling using pure Coulomb calculations. However, the deviations are still within the envelope of the limiting Coulomb cases and so perhaps a more prominent affect could be calculated by allowing the charge of the incident ion to affect the bound electron wavefunctions. It was thought that to more accurately model a partially-ionised medium on an atomic level, we should include the effects of the incident ion potential on the simulated electron wavefunctions. We aimed to employ a time-dependent Hartree-Fock technique to achieve this effect and some preliminary work was done to this end. However, none of my attempts at this were successful and the final work did not result in any time-dependent wavefunctions being calculated for further analysis.

In chapter 4, we were again investigating the effect microscopic variations in electron density could have on charged-particle stopping power. This investigation has some overlap in principle with chapter 3, although in this case we were not restricted to partially-ionised plasma systems. In this chapter, we were analysing the collective electron density profiles of several ions and electrons in any state of ionisation using DFT-MD. This was to investigate the effects that these density variations would have on particle stopping and to see if we could simulate the degree of energy straggling of an ion beam penetrating a dense plasma target. We extracted simulated line-of-sight paths from the DFT-MD plasma profiles and observed large variations in the local density, as seen in figure 4.1. Figure 4.5 shows that for a single particle case, calculations of the stopping power, and particle range can all be significantly affected by the cumulative effect of these density variations. Figure 4.5 shows that the resulting energy deposition profile differs significantly from the same case calculated using a mean density approximation. The statistical effect of these deviations over several particles traversing the same medium can be seen in figures 4.6, 4.7 and 4.8. These figures show that the behaviour of the cases using variable density calculations do remain close to the case using a mean density approximation. However, it is seen that there is a tendency for the average energy deposition to be reduced and the particle range to be increased in the variable density cases when

compared to the mean density case. This is confirmed in table 4.1 where it is seen that across twenty simulated particle cases in each of the three regimes chosen, the outcome was always that the mean DFT-MD ranges were greater than the range of the mean density case by at least one standard deviation of the ranges. The energy straggling of the beam behaves similarly across all cases shown in figures 4.6, 4.7 and 4.8. The straggling begins at zero, i.e. uniform energy of the beam particles, and increases as the stopping power increases to the Bragg peak. After the Bragg peak, as the stopping power is reduced and the particle energies are lowered to zero, the straggling of the beam also reduces to zero again. Since particle level stopping power models are now widely used, it would be possible to produce specific case simulations which might predict the beam straggling that would be observed in experiment. This would allow finer calculations of energy deposition to be made which could be advantageous for any case where ion beams are used as a method of energy delivery. Unfortunately, the magnitude of the effects that I have calculated here are small and so these effects could be difficult to observe.

In chapter 5, we investigated the calculations of particle stopping power in dense plasma regimes. Specifically, we investigated what effect the treatment of electron degeneracy would have on our stopping power calculations in dense plasma regimes. To do this we compared calculations of stopping power in dense plasmas from the Thomas-Fermi model with similar calculations using the T-matrix model, which simply treats the plasma as a very dense non-degenerate plasma. The scenario that we chose for this investigation was the initiation of a fusion burn wave in an inertial fusion fuel capsule. Figure 5.2 shows that for single particle stopping power calculations in plasmas that have strong electron degeneracy, the stopping power will be greatly over-estimated by models which do not take the electron degeneracy into account. We expanded upon this in our fusion heating example by allowing the stopping medium to be heated by the particle energy deposition. In the plasma regime we chose, the target electrons are heated by energy deposition of alpha-particles and the target ions are heated through electron-ion temperature equilibration. After some heating time, the stopping medium would transition from a degenerate electron regime into a regime where the target electrons are no longer degenerate. To give these calculations a little context with respect to an inertial confinement alpha-heating scenario, we used fusion energy alpha-particles, being produced at rates around the region of those expected in an inertial fusion hotspot. These alpha-particles were then depositing their kinetic energy in a dense hydrogen medium which was being heated from a degenerate regime to a non-degenerate regime in some simulation timescale. The results showed that for the case of a low

alpha-particle production rate, the effects of degeneracy on the stopping power can have a controlling influence on the energy deposition profile. This is seen in figure 5.9 where the heating timescales are slower when degeneracy is correctly treated and the energy is deposited over a wider volume of plasma. Figure 5.10 shows a case where the alpha production rate is very large and as a result the electron population of the plasma is quickly heated out of the degenerate regime. The result in this case is that the treatment of degeneracy does not make a significant a difference to the heating timescales or the energy deposition profile. This shows that the ion temperature profile can not respond quickly to the heating of the electrons and so its behaviour is limited by the rate of electron-ion temperature equilibration. The implication from this was that electron degeneracy could effect the timescales of these energy transfer processes in some heating regimes. However, for the case of very large fluxes of heating particles, the effects of degeneracy will be greatly reduced because the target electrons are rapidly heated into a non-degenerate regime. This idea was explored further by repeating the simulations for the two stopping power models over a wider range of alpha-particle creation rates and over a couple of cases of hotspot radii. The results of these simulations are shown in the summary figure 5.11. For each radii case, this figure shows a transition point at some alpha-particle production rate, where the two stopping power cases give equal heating timescales. For alpha-particle production rates above this value, the cases for each stopping power model will provide almost identical heating times and energy deposition profiles. This happens because the rate of ion heating is so strongly limited by the rates of the electron-ion temperature equilibration.

As with all investigations, there is still much room for expansion. Conclusions can be progressed, assumptions can be improved upon and new scenarios can be explored. The current outlook offers some possible directions that future researchers may pursue in order to extend this research. However, much of this would need a significant review of the initial assumptions made in the investigations presented in this thesis.

Bibliography

N.R. Arista and W. Brandt. *Phys. Rev. A*, 23, 1981.

S. Atzeni and J. Meyer-ter-Vehn. *The Physics of Inertial Fusion*. Clarendon Press, Oxford, 2004.

H. Bethe. *Ann. Phys (Leipzig)*, 5, 1930.

F. Bloch. *Ann. Phys. (Leipzig)*, 16, 1933.

David Bohm and David Pines. A collective description of electron interactions: iii. coulomb interactions in a degenerate electron gas. *Physical Review*, 92(3):609, 1953.

N. Bohr. *Phil. Mag.*, 25, 1916.

S.N. Bose. Plancks gesetz und lichtquantenhypothese. *Zeitschrift fur Physik*, 26, 1924.

R. Car and M. Parrinello. Unified approach for molecular dynamics and density-functional theory. *Physical Review Letters*, 55(22):2471, 1985.

M. Chabot, D. Gardès, J. Kiener, S. Damache, C. Deutsch, G. Maynard, M. Pouey, W. André, C. Fleurier, D. Hong, K. Wohrer, and D.H.H. Hoffmann in:. Gsi annual report: High energy density in matter produced by heavy ion beams. 21, 1994.

J. Daligault and S. Gupta. Electron-ion scattering in dense multi-component plasmas: application to the outer crust of an accreting neutral star. *Astrophys. J.*, 703, 2009.

L. de Ferrariis and N.R. Arista. *Phys. Rev. A*, 29, 1984.

A. Djaoui. Radiation hydrodynamics of x-ray driven targets. *Journal of Quantum Spectroscopy and Radiative Transfer*, 54(1), 1995.

R. Drake. *High Energy Density Physics: Fundamentals, Inertial Fusion and Experimental Astrophysics*. Springer, Berlin, 2006.

P. Dufour, J. Liebert, G. Fontaine, and N. Behara. White dwarf stars with carbon atmospheres. *Nature*, 450, 2007.

E. Fermi. Sulla quantizzione del gas perfetto monoatmoico. *Rendiconti Lincei*, 3, 1926.

E. Fermi and E. Teller. *Phys. Rev.*, 72, 1947.

D.O. Gericke. *Kinetische Theorie der Stopping Power Nichtidealer Plasmen*. PhD thesis, Ernst-Moritz-Arndt-Universität Greifswald, 2000.

D.O. Gericke. Stopping power for strong beam-plasma coupling. *Laser and Particle Beams*, 20(3):471, 2002.

D.O. Gericke and M. Schlanges. Beam-plasma coupling effects on the stopping power of dense plasmas. *Physical Review E*, 60(1):904, 1999.

D.O. Gericke, M. Schlanges, and W.D. Kraeft. *Phys. Letters A*, 222, 1996.

D.O. Gericke, M. Schlanges, and M.S. Murillo. Dense plasma temperature equilibration in the binary collision approximation. *Physical Review E*, 65(3):036418, 2002.

S. H. Glenzer, B. J. MacGowan, P. Michel, N. B. Meezan, L. J. Suter, S. N. Dixit, J. L. Kline, G. A. Kyrala, D. K. Bradley, D. A. Callahan, E. L. Dewald, L. Divol, E. Dzenitis, M. J. Edwards, A. V. Hamza, C. A. Haynam, D. E. Hinkel D. H. Kalantar, J. D. Kilkenny, O. L. Landen, J. D. Lindl, S. LePape, J. D. Moody, A. Nikroo, T. Parham, M. B. Schneider, R. P. J. Town, P. Wegner, K. Widmann, P. Whitman, B. K. F. Young, B. Van Wonterghem, L. J. Atherton, and E. I. Moses. Symmetric inertial confinement fusion implosions at ultra-high laser energies. *Science*, 327, 2011a.

S.H. Glenzer, B. J. MacGowan, N. B. Meezan, P. A. Adams, J. B. Alfonso, E. T. Alger, and Z. Alherz et al. Demonstration of ignition radiation temperature in indirect-drive inertial confinement fusion hohlraums. *Phys. Rev. Lett.*, 106, 2011b.

P. Gluck. *Nuovo Cimento*, 38, 1971.

A. Golubev, M. Basko, A. Fertmann, A. Kosodaev, N. Mesherayakov, B. Sharkov, A. Vishnevskiy, V. Fortov, M. Kulish, V. Gryaznov, V. Mintsev, E. Golubev,

A. Pukhov, V. Smirnov, U. Funk, S. Stoeve, M. Stetter, H.P. Flierl, D.H.H. Hoffmann, J. Jacobi, and I. Iosilevski. *Phys. Rev. E*, 57, 1998.

T. Guillot. Interiors of giant planets inside and outside the solar system. *Science*, 72, 1999.

S. W. Haan, J. D. Lindl, D. A. Callahan, D. S. Clark, J. D. Salmonson, B. A. Hammel, L. J. Atherton, R. C. Cook, M. J. Edwards, S. Glenzer, A. V. Hamza, S. P. Hatchett, M. C. Herrmann, D. E. Hinkel, D. D. Ho, H. Huang, O. S. Jones, J. Kline, G. Kyrala, O. L. Landen, B. J. MacGowan, M. M. Marinak, D. D. Meyerhofer, J. L. Milovich, K. A. Moreno, E. I. Moses, D. H. Munro, A. Nikroo, R. E. Olson, K. Peterson, S. M. Pollaine, J. E. Ralph, H. F. Robey, B. K. Spears, P. T. Springer, L. J. Suter, C. A. Thomas, R. P. Town, R. Vesey, S. V. Weber, H. L. Wilkens, and D. C Wilson. Point design targets, specifications and requirements for the 2010 ignition campaign on the national ignition facility. *Phys. of Plasmas*, 18, 2011.

B. A. Hammel, H. A. Scott, S. P. Regan, C. Cerjan, D. S. Clark, M. J. Edwards, R. Epstein, S. H. Glenzer, S. W. Haan, N. Izumi, J. A. Koch, G. A. Kyrala, O. L. Landen, S. H. Langer, K. Peterson, V. A. Smalyuk, L. J. Suter, and D. C. Wilson. Diagnosing and controlling mix in national ignition facility implosion experiments. *Phys. of Plasmas*, 18, 2011.

D. Hochstuhl and M. Bonitz. Two-photon ionization of helium studied with the multiconfigurational time-dependent hartreefock method. *Journal of Chemical Physics*, 134:084106, 2011.

P. Hohenberg and W. Kohn. Inhomogeneous electron gas. *Physical Review*, 136(3), 1964.

J.D. Huba. *NRL plasma formulary*. Naval Research Laboratory, Washington, 2007.

S. Ichimaru. *Statistical Plasma Physics I*. Addison-Wesley, Redwood City CA, 1992.

S. Ichimaru. *Statistical Plasma Physics Vol. 1: Basic Principles*. Westview Press, Colorado, 2004.

C.J. Joachain. *Quantum collision theory*. North-Holland, 1975.

W. Kohn and L.J. Sham. Self-consistent equations including exchange and correlation effects. *Physical Review*, 140(4), 1965.

W. D. Kraeft and B. Strege. *Physica A*, 149, 1988.

D. Kremp, M.Schlanges, and W.-D Kraeft. *Quantum statistics of nonideal plasmas*. Springer, Berlin, 2004.

G. Kresse and J. Hafner. ab initio molecular dynamics for liquid metals. *Physical Review B*, 47(1):558, 1993.

David J. Land, Donald G. Simons, James G. Brennan, and G.A. Glass. Range distributions and electronic stopping power of nitrogen ions in solids. *Nuclear instruments and methods in physics research*, page 234, 1985.

J.D. Lawson. Some criteria for a power producing thermonuclear reactor. *Proceedings of the Physical Society B*, 70, 1957.

Chi-Kang Li and Richard D. Petrasso. Charged-particle stopping powers in inertial confinement fusion plasmas. *Physical Review Letters*, 70(20):3059, 1993.

J. Lindhard. *K. Dan. Vidensk. Selsk. Mat. Fys. Medd.*, 28, 1954.

J. Lindl. *Inertial Confinement Fusion*. Springer, New York, 1998.

J.D. Lindl and E.I. Moses. Special topic: Plans for the national ignition campaign (nic) on the national ignition facility (nif): On the threshold of initiating ignition experiments. *Phys. of Plasmas*, 18, 2011.

Richard M. Martin. *Electronic Structure: Basic Theory and Practical Methods*. Cambridge University Press, Cambridge, 2004.

N. David Mermin. Thermal properties of the inhomogeneous electron gas. *Physical Review*, 137(5), 1965.

P. Michel, L. Divol, R. P. J. Town, M. D. Rosen, D. A. Callahan, N. B. Meezan, M. B. Schneider, G. A. Kyrala, J. D. Moody, E. L. Dewald, K. Widmann, E. Bond, J. L. Kline, C. A. Thomas, S. Dixit, E. A. Williams, D. E. Hinkel, R. L. Berger, O. L. Landen, M. J. Edwards, B. J. MacGowan, J. D. Lindl, C. Haynam, L. J. Suter, S. H. Glenzer, and E. Moses. Three-wavelength scheme to optimize hohlraum coupling on the national ignition facility. *Phys. Rev. E*, 83, 2011.

B. Militzer, W. Hubbard, J. Vorberger, I. Tamblyn, and S. Bonev. A massive core in jupiter predicted from first-principles simulations. *Astrophys. J. Lett.*, 688, 2008.

E. Moses and C. Wuest. The national ignition facility: Laser performance and first experiments. *Fusion Science and Technology*, 47, 2005.

N. Nettelmann, B. Holst, A. Kietzmann, M. French, and R. Redmer. Ab initio equation of state data for hydrogen, helium and water and the internal structure of jupiter. *Astrophys. J.*, 683, 2008.

Roger G. Newton. *Scattering Theory of Waves and Particles, Second Edition*. Dover Publications, Inc., 1982.

B.V. Numerov. A method of extrapolation of perturbations. *Monthly Notices of the Royal Astronomical Society*, 84:592, 1924.

C.A. Ordonez and M.I. Molina. *Phys. Rev. Lett.*, 72, 1994.

T. Peter and J. Meyer-ter-Vehn. *Phys. Rev. A*, 43, 1991.

E. Rutherford. The scattering of alpha and beta particles by mater and the structure of the atom. *Phil. Mag.*, 21, 1911.

P. Sigmund. *Phys. Rev. A*, 26, 1982.

Stanley Skupsky. Energy loss of ions moving through high-density matter. *Physical Review A*, 16(2):727, 1977.

P. Spiller and G. Franchetti. The fair accelerator project at gsi. *Nuclear Instruments and Methods in Physics Research Section A: Accelerators, Spectrometers, Detectors and Associated Equipment*, 561(2):305, 2006.

N.A. Tahir, A.R. Piriz, A. Shutov, D. Varentsov, S. Udrea, D.H.H. Hoffmann, H. Juranek, R.Redmer, R.F. Portugues, I. Lomonsov, and V.E. Fortov. *J. Phys. A: Math. Gen.*, 36, 2003.

N.A. Tahir, A. Shutov, A.R. Piriz, I.V. Lomonosov, C. Deutsch, P. Spiller, and Th. Stöhlker. Application of intense heavy ion beams to study high energy density physics. *Plasma Physics and Controlled Fusion*, 53(12):124004, 2011.

J.J. Thomson. On the structure of the atom: an investigation of the stability and periods of oscillation of a number of corpuscles arranged at equal intervals around the circumference of a circle; with application of the results to the theory of atomic structure. *Phil. Mag.*, 7(39):237, 1904.

J. Vorberger, D.O. Gericke, and W.-D. Kraeft. The hydrogen equation of state at high densities. *Arxiv*, 2011.

J. Vorberger, Z. Donko, I.M Tkachenko, and D.O. Gericke. The dynamic ion structure factor in warm dense matter. *Physical Review Letters*, 109(22):225001, 2012.